Theoretical studies on imaging of electron motion and excitation on ultrafast time scales

by

J. Venzke

B.S., Drake University, 2016

M.S., University of Colorado at Boulder, 2020

A thesis submitted to the
Faculty of the Graduate School of the
University of Colorado in partial fulfillment
of the requirements for the degree of
Doctor of Philosophy
Department of Physics
2021

Committee Members:
Andreas Becker, Chair
John Bohn
Jose D'Incao
Michael Litos
Bengt Fornberg

Venzke, J. (Ph.D., Physics)

Theoretical studies on imaging of electron motion and excitation on ultrafast time scales

Thesis directed by Dr. Andreas Becker

The development of ultrashort laser pulses with durations of a few tens of attoseconds (1 as = 10^{-18} s) has opened the possibility of observing and controlling the motion of electrons in matter at their natural time scale. However, the broad spectral bandwidth of the pulses pose the challenge that several linear and nonlinear pathways compete and interfere during the interaction of those pulses with the target. The ionized electrons contain information about the target, the electronic wavepacket prior to ionization, the laser pulse, and the various pathways to ionization. In this thesis, we will use numerical and analytic tools to study and interpret these ionization spectra. Additionally, we will examine electron excitation to Ryberg states driven by intense IR pulses and discuss the tools we are developing to study electron correlation.

First, we will give a brief review of ultrafast and ultrastrong physics literature. This is followed by an overview of the numerical and analytic methods used in this thesis including our recent insights in frequency corrections for short pulses and work on using radial basis functions to solve the time-dependent Schrödinger equation. We then focus on few photon ionization including effects induced by ultrashort pulses, the development of novel generalized asymmetry parameters, and the reconstruction of electronic wavepackets undergoing attosecond motion. Next, we present theoretical studies concerning the analysis of excitation and stabilization effects related to Rydberg states in the case of both linear and bi-circular laser pulses. Finally, we will discuss the development and first tests of a fully correlated two-electron code that utilizes a basis of hyperspherical harmonics.

Dedication

To my parents Jim and Kelli, siblings Tom and Andrea, brother-in-law Bobby, niece Jaidyn, and nephew Robby.

Acknowledgements

It is amazing how important a great support system is to achieving a PhD. There are many more friends, family members, acquaintances, and colleagues who have helped me along the way than I have space to mention here, but I will do my best. To start off, I would like to thank my PhD advisor, Andreas Becker, for his never ending support, both professionally and personally, during my PhD. I would also like to thank my committee members John Bohn, Jose D'Incao, Michael Litos, and Bengt Fornberg for the fruitful scientific discussions along the way.

I would be admiss if I didn't acknowledge my high school physics teacher David Sklenicka for sparking my interest in physics. Without his influence, it is very unlikely I would have pursued a PhD in physics. I would also like to extend many thanks my undergraduate community at Drake University, most notably Klaus Bartschat and Nicolas Douguet for developing my interest in ultrafast physics and Timothy Urness for inspiring my interest in computer science.

I extend great gratitude to my fellow lab mates and collaborators both past and present: Andrew Spott, Cory Goldsmith, Erez Shani, Brynn Reiff, Tennesse Joyce, Yonas Gebre, Spencer Walker, Andres Mora, Bejan Ghomashi, Zetong Xue, Lucas Kolanz, Edward MacDonald, and Agnieszka Jaron-Becker. The countless scientific discussions and support through out my PhD have been instrumental in developing the contents of this thesis.

Finally, I would like to extend my greatest thanks to my parents Jim and Kelli and siblings Andrea and Tom for the endless support when there was the enviable setback, multi-week long hunts for bugs in my code, and when life threw curve balls. Without their support, there is no way I would have been able complete my PhD.

Contents

Chapter

Tables

Table

Figures

Figure

Chapter 1

Introduction

In 1905, Einstein published a paper on the photoelectric effect [56], for which he later received the Noble Prize. The effect shows when light is shined on an object an electron can be ionized from an atom, molecule, or solid by absorbing a photon with a sufficiently high energy. With the advent of the laser in 1960, it became possible to focus coherent light tight enough to allow the ionization process to occur not only by absorbing one but many photons in rapid succession leading to a process known as multiphoton ionization [85]. Since then, laser intensities have increased to the point where the superposition of the electric field of the laser with the attractive potential produced by a nucleus can create a barrier and allow the electron to tunnel and ionize from the atom [123]. Furthermore, depending on various laser parameters, the electron that tunneled through the barrier can interact with the laser field and recombine with the residual ion. During the recombination process, photons are released at harmonics of the driving laser's central frequency. This process can convert a large numbers of infrared (IR) photons into a single X-ray photon in a process known as high-order harmonic generation (HHG) [71, 140, 40]. HHG is one method that allows for the production of bright X-ray laser pulses with pulse durations as short as tens of attoseconds [256, 37] (10^{-18} sec). Recent developments have allowed for the generation high-order harmonics using not only linearly polarized lasers but also lasers or combination of lasers with other polarizations [64, 196, 125, 58, 100]. Such pulses provide the tools necessary for the imaging of electron dynamics on their fundamental time scale [135].

Einstein's photoelectric effect mostly considered continuous wave (CW) light that produced a near delta function like energy distribution. These CW lasers are good for precision energy measurements, however, their time resolution it greatly limited. The recent advances in attosecond pulse technology have strongly decreased the interaction time allowing for the imaging of (attosecond) electron dynamics at the cost of energy bandwidths of the pulses on the order of several eVs. The largely increased pulse bandwidth, however, leads to many competing pathways of ionization that can involve different numbers of photons complicating the ionization process. The photoelectron angular distributions (PAD) produced by such pulses contain complex shapes that encode features of the target's initial wavefunction, ionization cross sections for each process, the ionizing pulse, and the various competing pathways to ionization. This naturally raises the question of how can one backtrack all of this information from such a PAD signal?

In this thesis, we will explore methods to understand and image the motion of electrons on ultrashort time scales from ionization signals and photoelectron angular distributions. Then, we will also analyze how intense IR light can cause that electrons are being trapped in highly excited states although the absorption of a single additional photon would lead to ionization. Finally, the focus will be turned to a new numerical method that we are developing to study two fully correlated electrons interacting with each other and an ultrafast laser pulse.

1.1 Attosecond time scale

The idea of an attosecond (1 as $= 10^{-18}$ sec) is difficult to wrap ones mind around. Some perspective can be gained by noting that there are more attoseconds in a single second than seconds in the lifetime of the universe. At this ultrashort time scale, nearly all motion in an atom, molecule or solid is frozen. Only the motion of electrons, particularly that in atoms as visualized in Fig. 1.1, is non-negligible. With laser technology recently reaching pulse durations with sub 100 attosecond pulse widths [256, 37], it is becoming possible to "image" electrons as they move around inside of atoms and molecules. One approach to imaging electron motion will be presented in this thesis (see Chap. 4).

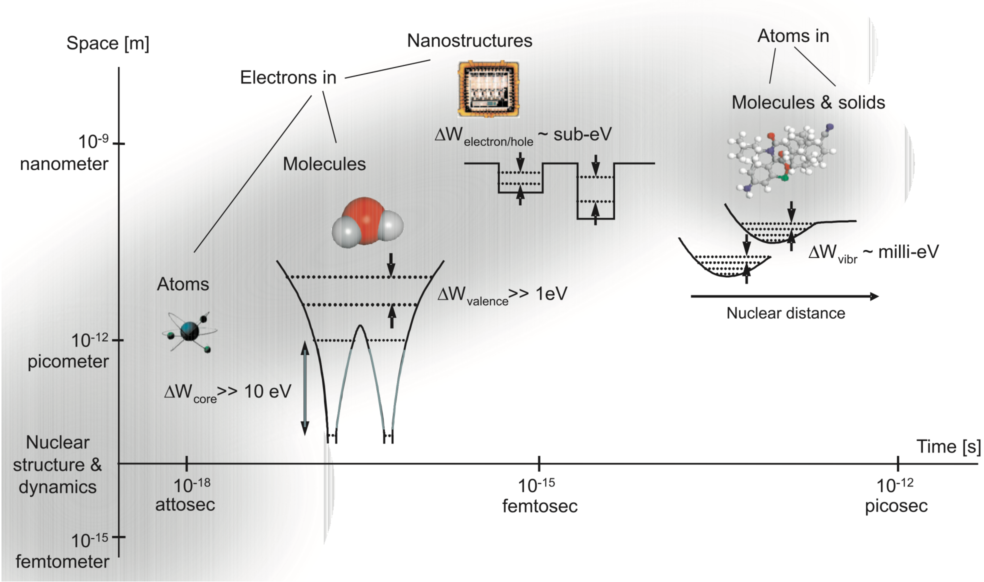

Figure 1.1: Relevant space and time scales present in ultrafast physics. (Figure from [135])

1.2 Light sources

The fields of ultrastrong and ultrafast physics rely on bright laser light to study and understand the behavior of matter on short time scales. The light used ranges from intense IR radiation, that can bend atomic and molecular potentials enough to allow electrons to tunnel into the continuum, to hard X-rays that can ionize multiple electrons with a single photon. The intense IR light is often produced using Ti:sapphire or similar laser setups. In the following subsections, we will briefly describe the two major sources of ultrafast extreme ultraviolet (XUV) to X-ray sources and the applications they are designed for.

1.2.1 High harmonic generation

High harmonic generation (HHG) is a process that converts low-energy photons of intense IR laser pulses into high-energy photons of an X-ray laser pulse through a highly non-linear and non-perturbative process. The process is often understood through the so-called three step model shown in Fig. 1.2 [140, 40, 197]. First, the strong electric field of the IR laser bends the atomic Coulomb potential allowing for the electron to tunnel ionize. Next, the electron interacts with the field gaining energy and reversing direction when the oscillating field changes direction. Finally, the electron recombines with the ion releasing its energy in the form of a high-energy photon. For linearly polarized laser pulses, the emitted electrons have energies corresponding to $(2n+1)\omega$ where n is an integer and ω in the central frequency of the driving laser pulse.

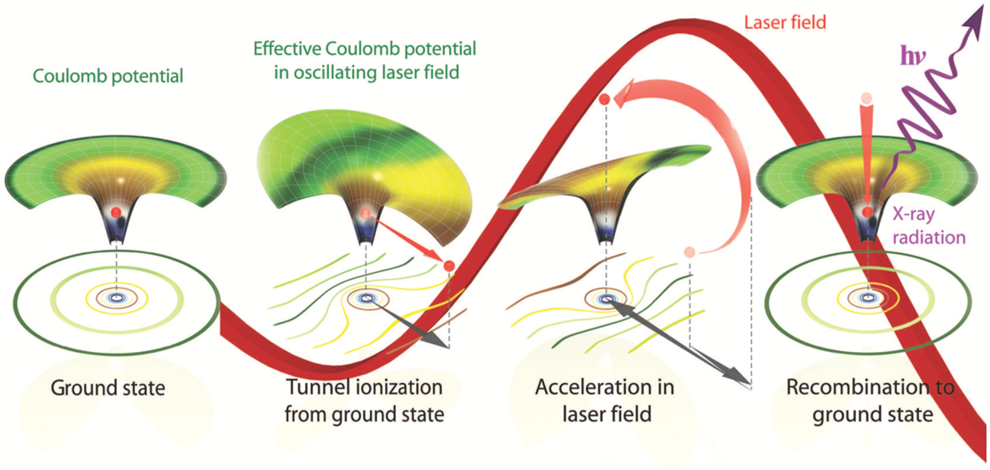

Figure 1.2: Schematics of the three step model in which an electron tunnel ionizes, is accelerated in the continuum by the driving laser and recombines with the remaining ion producing a high energy photon. (Figure from [197])

Nowadays, HHG sources can produce laser pulses with arbitrary polarization [64, 196, 125, 58, 100]. The theoretical method for generating circularly polarized HHG sources was proposed more than two decades ago [53, 150]. By using two counter rotating cicularly polarized IR lasers with frequencies ω and 2ω, a so called counter-rotating bi-circular laser pulse is produced. The three fold symmetry of the final laser pulse allows for the electron to recombine with the parent ion, something that is not possible with a circularly polarized pulse alone. The resulting HHG spectrum contains circularly polarized harmonics at energies of $(3n+1)\omega$ and $(3n+2)\omega$ with alternating helices and no harmonic at energies of $3n\omega$. Since then, non-collinear methods of circularly polarized HHG [100] and methods for elliptically polarized harmonics [12] have been demonstrated.

HHG sources have the advantage that they are compact table top setups. Additionally, the light produced is coherent and carrier-to-envelope phase locking can be achieved in certain cases, which make it possible to control the light produced in these sources. As a result, trains of attosecond long pulses can be generated [128], and isolated pulses with a duration of only a few tens of attoseconds have been demonstrated [256, 37]. For more details on HHG light sources, we refer to Ref. [197, 38]

1.2.2 Free electron lasers

Free electron lasers (FEL) differ significantly from HHG sources. Often located at large shared user facilities [218], they start with a high energy electron beam from an accelerator. The electron beam is then passed through an undulator consisting of alternating magnetic fields. The electrons oscillate back and forth leading to a phenomenon known as micro bunching and the generation of light. After leaving the undulator, the electron beam is dumped while an X-ray laser pulse propagates towards the experimental stations, as shown in Fig. 1.3. By tuning the spacing between the magnets, the frequency of the light can be changed.

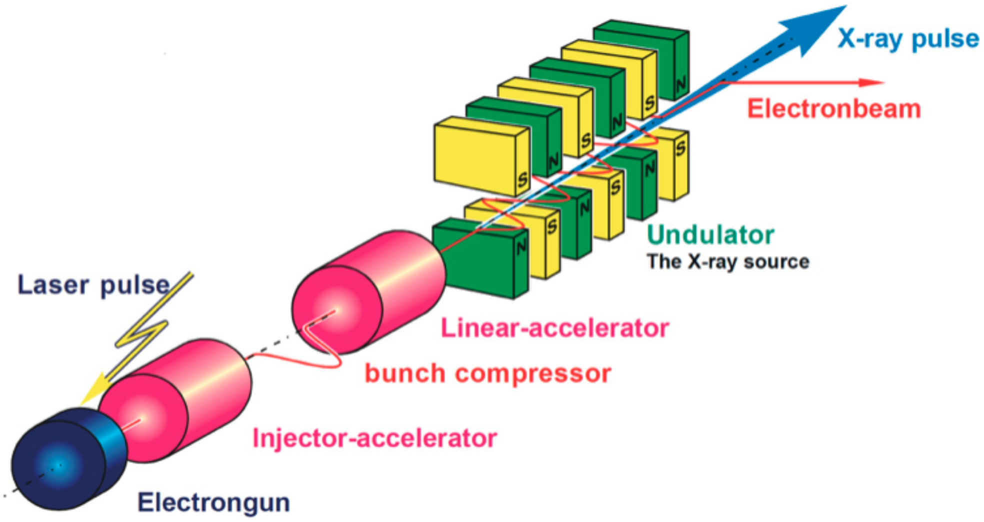

Figure 1.3: Schematics of an FEL laser showing the electron bunch production, undulator, and beam dump that are essential parts to generate an X-ray pulse. (Figure from [202])

Due to the large amount of energy in an electron bunch, FEL sources are much brighter than HHG sources in the same frequency range. FEL can produce arbitrary polarized laser pulses [109] and pulses with a duration less than a femtosecond have been demonstrated [158]. The laser pulses, however, are only partially coherent and their shape varies widely from shot to shot limiting their application for effects that depend significantly on the control of the pulse parameters. For more details on FEL technology, see [218].

1.3 Organization of this thesis

The remainder of this thesis is organized as follows. In Chap. 2 we cover the relevant theoretical and experimental background. Chap. 3 provides a detailed description of the analytical and numerical methods used in this thesis to model ultrafast laser-atom interactions. In Chap. 4 we present results of computations showing the impact of ultrashort laser pulses on the ionization process and how the ionized electrons can be used to analyze electron motion on the attosecond time scale. Next, in Chap. 5 various mechanisms by which electrons are excited into Rydberg states when interacting with intense IR laser pulses are discussed. Finally, in Chap. 6 we provide details on the development of a two-active electron code using hyperspherical harmonics including its current status, first tests, and possible paths forward. In this thesis, atomic units ($\hbar = e = m = 1$) are used throughout unless noted otherwise.

Chapter 2

Theoretical and experimental background

2.1 Attosecond dynamics

Understanding and imaging motion on fast time scales has been of interest for more than a century. In 1878, Eadweard Muybridge invented high speed photography to find out if all of a horse's feet leave the ground at a full gallop [174]. Since then, high speed photography has reached time scales of $\sim 10^{-5}$s, a long ways off of the attosecond (10^{-18}s) time scale of electron motion. On attosecond time scales, only electrons in atoms and molecules display significant motion (see Fig. 1.1) rendering electronic or mechanical shutters, from traditional photography, useless. Additionally, the electrons being imaged are quantum objects further complicating the imaging process. Before we go into the methods used for imaging electron motion, lets dive into what we mean when we say a quantum object is moving.

For a time independent system, such as an atom or molecule in vacuum, there exists a set of stationary states that are eigenfunctions of the system's Hamiltonian (for details see Sec. 3.1). In the case of an atom or molecule, these stationary states are the bound or continuum states which we will call $|\psi_j(\mathbf{r})\rangle$. These states depend on space, and evolve in time like e^{iE_jt} where E_j is the energy of the jth stationary state, $i = \sqrt{-1}$ is the imaginary number, and t is time. This shows that only the phase of the state is changing in time. As the global phase of a wavefunction is not observable, an electron occupying a single stationary state displays no motion.

For attosecond motion to occur, either the system's Hamiltonian must become time dependent, e.g. by introducing a laser pulse, and/or multiple stationary states must be populated forming a superposition. The former is often required to image the motion of electrons, but the latter is simpler to understand. We will, therefore, start with the motion produced by an electron in a superposition of more than one stationary state. In principle, one or more of the states could be continuum states, but for simplicity we restrict ourselves to bound states only in the following discussion. The resulting electronic wavefuction can be written as

$$|\Psi(\mathbf{r},t)\rangle = \sum_{j=0}^{N-1} a_j e^{i(\phi_j + E_j t)} |\psi_j(\mathbf{r})\rangle \tag{2.1}$$

where a_j is a non-negative real number, ϕ_j is a phase, E_j is the energy of the state, and the superposition contains N total states each labeled by the subscript j. The global phase can be accounted for by removing the time dependent phase of the ground state by setting $E_0 = 0$. The relative phases of the excited states ($j > 0$) changes in time like $(E_j - E_0)t$ resulting in dynamics if $E_j \neq E_0$. For a two state system, the dynamics will be periodic with a period of $T = 2\pi/|E_1 - E_0|$. Fig. 2.1 shows the dynamics of the wavefunction for a helium atom in a $1s - 2p_+$ superposition as it rotates with a period of approximately 200 attosecond.

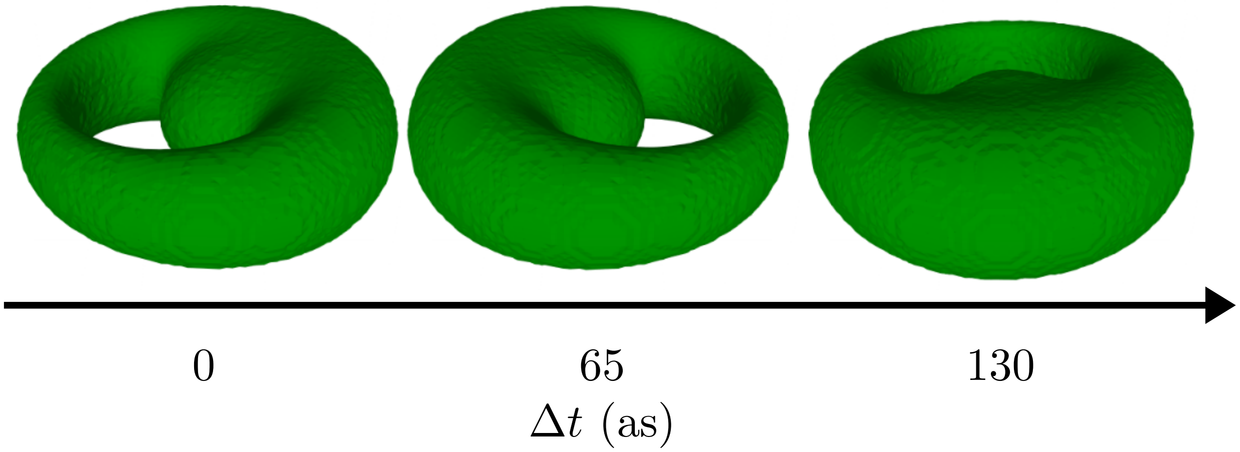

Figure 2.1: An isosurface of the wavefunction of a helium atom in a $1s - 2p_+$ superposition ($|r\Psi|$) undergoing attosecond motion. (Figure from [233])

Adding additional states to the superposition allows for arbitrarily complicated field free dynamics to occur. In order to "image" the wavepacket, all of the values for a_j and ϕ_j must be obtained at some time t_0 with the restrictions that $a_0 = \sqrt{1 - \sum_{j=1}^{N-1} a_j^2}$ and $\phi_0 = 0$ to enforce normalization and removing the global phase, respectively. Then using Eq. 2.1, the time dependence of the system is known. A method for imaging simple superpositions is presented in Sec. 4.3.

When the system's Hamiltonian becomes time dependent, however, the above approach does not capture the dynamics completely. If the time dependent operator is weak, relative to the time independent operators, the dynamics maybe captured by allowing a_j and ϕ_j to become time dependent quantities. When effect of the time dependent operator becomes comparable or larger than the independent operators, the stationary states, $|\psi_j(\mathbf{r})\rangle$, may no longer be a good basis to describe the system. Imaging the dynamics of such a system requires techniques beyond the scope of this thesis.

2.2 Pump-probe spectroscopy

Pump-probe spectroscopy is a powerful tool for imaging ultrafast processes. The general concept is quite simple. Two isolated ultrashort pulses are produced. The first pulse, known as the pump pulse, prepares the system by starting some dynamical process. Some time after the end of the first pulse, the second (probe) pulse images the target. By delaying the probe pulse with respect to the pump pulse, the impact of the dynamics on a given observable can be observed experimentally. This gives a glimpse at how the system evolves over time. Although conceptually easy to understand, attosecond pump-probe spectroscopy is an extremely difficult experiment to perform for the following reasons.

In many cases, it is required to have both angle- and/or energy-resolved spectra of the ionized electrons. With the development of experimental techniques, such as velocity map imaging (VMI) [131, 210] or cold target recoil ion momentum spectroscopy (COLTRIMS) [229], the detection of angle-resolved emission of the photoelectron following few-photon ionization of atomic and molecular targets has become possible [153]. Additionally, one requires the ability to produce well controlled isolated ultrafast laser pulses. In the recent past, it has become possible to generate isolated attosecond pulses [70]. This has opened the door for the application of pump-probe spectroscopy to attosecond physics.

In 2001, the first experimental observation of attosecond electron dynamics was made with a pump-probe setup including a few cycle visible light pulse and an attosecond soft-X-ray pulse [95]. The bandwidth of attosecond laser pulses allows for both bound and continuum states to be studied [161] and, more recently, charge dynamics in Tryptophan on the sub 4fs time scale have been observed showing that attosecond pump-probe spectroscopy may be applied to complex molecules [137]. As experimental techniques evolve, the application of attosecond pump-probe experiments will continue to expand. In this thesis, we look at how pump-probe spectroscopy can be used to understand the ionization of electrons in superposition states in Sec. 4.2 and reconstruct attosecond electron motion in Sec. 4.3.

2.3 Few photon ionization

Multiphoton ionization was proposed by Göppert-Mayer in 1931 [85]. Thirty years later, two photon ionization was demonstrated experimentally, shortly after the advent of the laser [120]. As we approach a century since the proposal of multiphoton ionization, research in this area is still progressing. With recent advances in HHG and FEL laser pulse sources in the extreme-ultraviolet (EUV) wavelength regime, studies involving few photon ionization in the perturbative intensity regime have been of both experimental and theoretical interest [177, 230, 220, 193, 65, 214, 86, 66, 112, 113, 153, 207, 82, 47, 103, 104, 25, 243]. Using tools like VIM and COLTRIMS allows for both the direction and momentum of the ionized electrons to be detected. At a given electron energy, the probability distribution of an electron being ionized in a specific direction is known as a photoelectron angular distribution (PAD).

PADs contain information containing about the phase and amplitude of the various partial waves produced during the ionization process. These signals have been used to study the competition between resonant and non-resonant two-photon ionization pathways [112, 113, 153] and between one- and two-photon ionization channels [82, 47, 25]. These tools are also used to investigate the impacts of many other physical effects, such as a significant circular dichroism via the asymmetry in the forward-backward electron emission from bromocamphor molecules induced by circularly polarized light has been identified [26]. Observation of the breakdown of the symmetry in the photoelectron emission of argon has been shown in the region of the Cooper minimum [110], molecular vibrations and chirality have been studied [75] and other applications range from studies of coherent control [199] to the characterization of ultrashort laser pulses [35].

Through the contents of Chap. 4 we explore the impacts of few photon ionization using ultrashort pulses (Sec. 4.1), proposing new asymmetry parameters for understanding few photon ionization of electrons in superpositions (Sec. 4.2) and how few photon ionization can be used to reconstruct attosecond electron motion (Sec. 4.3).

2.4 Rydberg state excitations induced by strong fields

Excited states in atoms and molecules have played an important role in the understanding of many physical phenomena in strong field physics such as resonant enhancement in the population of excited states [42, 119], structures in the energy spectrum [72, 190, 3], and in energy-resolved angular distributions [209] of photoelectrons. When excited states become resonant with a one- or multiphoton process from an initial state, the electron can populate the excited state. Depending on the system and laser involved, the population in the excited state can be trapped or it can enhance the probability of another process occurring. The role of excitation was initially observed via resonant enhancement in the population of excited states [42, 119] and structures in the energy spectrum [72, 190, 3] and in energy-resolved angular distributions [209] of photoelectrons.

As the laser intensity increases, the ionization potential of an atom shifts into the continuum due to the AC-Stark shift. Additionally, the resonances of highly excited states, known as Rydberg states, follow the same trend. The AC-Stark shifted resonance (E') for highly excited states is therefore approximately

$$E' = E + U_p \,, \tag{2.2}$$

where E is the field-free energy of the excited state, $U_p = I/4\omega^2$ is the ponderomotive energy, I is the peak laser intensity, ω is the central frequency of the laser, and E' is the energy of the shifted resonance. The initial findings were explained examining the effects of multiphoton absorption becoming resonant with the AC-Stark shifted states.

More recently, significant excitation of atoms has also been observed in the tunneling regime and described by the frustrated tunneling ionization (FTI) model for linearly polarized lasers [180]. Similar to the three-step model of HHG, the FTI model starts with the tunnel ionization of an electron. The electron then interacts with the trailing end of the laser pulse which is slowing it down. Finally, the electron is recaptured by the ionic potential ending with a final energy corresponding to that of a Rydberg state. This observation has renewed the general interest in the mechanisms leading to the population of excited Rydberg states during the interaction of an atom with an intense laser pulse (most recently, e.g., in Refs. [38, 145, 144, 260, 221, 32, 142, 59, 27, 73, 152, 219, 89, 176, 248, 19, 138, 261, 22, 74, 115, 109, 156, 247, 194]).

The FTI model is semi-classical and provides no predictive power for the angular momentum distribution of the populated excited states. Therefore, recent theoretical studies of the excitation mechanism in linearly polarized strong fields mainly consider the distribution of the population as a function of the principal quantum number of the excited states [145, 144, 261, 247, 194]. It was shown that the modulation of the excitation probability is related to the channel closing effect [134, 145, 144, 194]. The latter phenomenon occurs at threshold intensities at which the absorption of one more photon is needed to ionize the atom due to the AC- Stark shift. The interpretation that an increase in excitation can be understood as result of the shift of the first ATI peak below the ionization threshold [145, 144] is in agreement with the explanation of earlier experimental results (e.g., [72, 119, 209]) via the resonance enhanced population of AC-Stark shifted excited states.

On the other hand, the literature provides very limited understanding of the angular momentum distribution in the populated Rydberg states by linearly polarized fields. Assuming the initial state has even angular momentum, it has been shown that the populated Rydberg states have angular momentum with the same parity as $N_p - 1$, with N_p being the minimum number of photons needed to ionize the AC-shifted ionization potential using Floquet theory for a monochromatic laser field [134] and results of numerical calculations for laser pulses with a trapezoidal envelope [194].

Furthermore, the angular quantum number of the states with the largest population in numerical calculations [145, 144, 194] agrees well with semiclassical estimations [6], initially performed for low-energy angular resolved photoelectron distributions.

For more complex laser set-ups, such as bichromatic circularly polarized laser pulses, almost no work on the population of Rydberg states has been done. Recently, in bicircular fields it has been observed that the probability to ionize an atom is significantly enhanced if the two fields are counter-rotating as compared to co-rotating fields [157]. In that work, the authors propose that the counter-rotating pulse's ionization pathways allow for resonance enhanced ionization while the co-rotating pulse's do not due to selection rules. However, distributions over the quantum numbers (principal, angular momentum, magnetic) were not presented. Such analysis can shed further light on the role of excited states in the pathways to ionization since excitation in a resonant multiphoton process should rely on the spin-angular momentum selection rules for the absorption of circularly polarized photons.

In this thesis, we examine the excitation of Rydberg states in Chap. 5. We study the angular momentum distributions caused by linearly polarized lasers in Sec. 5.1 and the various mechanisms present in the excitation of Rydberg states by bicircular laser pulses in Sec. 5.2.

2.5 Electron correlation

For many effects in ultrafast physics, the single-active electron approximation (SAE), where one electron is allowed to move in an effective potential of all remaining electrons and nuclei, is valid. However, for laser pulses with high energy photons, multiple electrons can interact leading to effects caused by electron correlation. Boll et al. recently showed that the SAE approximation breaks down in the interaction of helium with lasers at high central frequencies [25].

Electron correlation effects can manifest themselves in many ways. One such example can be found in direct vs. autoionizing channels [39] where anisotropy and asymmetry parameters have been used to study the impact of the $3s^{-1}np$ resonance in argon. When interacting with an autoionizing resonance, a photon is absorbed by an electron with energy that would allow for ionization and the promotion of a second electron to an excited state. The first electron remains in the resonant state long enough to share its energy via electron correlation with another electron that is excited to a state of higher energy. The first electron is then ionized at a lower energy.

In addition to autoionizing resonances, two electrons can be ionized by a single photon in a process known as single photon double ionization [160]. The process proceeds via two main mechanisms, non-sequential double photoionaization (NSDI) and shake-off. In NSDI, the first electron absorbs a high energy photon before it interacts with a second electron. Both electrons are then ionized with similar final energies. The ionized electrons are correlated and have been shown to produce a double slit pattern when double ionizing the H_2 molecule [5]. When even higher photon energies are used, the first electron can be ionized so quickly, that the ionic potential is rapidly changed and a second electron is ionized with a vary small relative momentum in the shake-off process [33]. At even higher photon energies, core electrons can be ionized leaving a hollow atom. A valence electron can then relax into the hole left behind. To conserve energy, a second valence electron is ionized in a process known as the Auger effect originally proposed in 1922 [166].

In order to study these problems in detail, fully correlated multi-electron calculations are required. A solution to the time dependent Schrödinger equation (TDSE) in full dimensions requires $3N_e + 1$ dimensions where N_e is the number of electrons and the last dimension is time. For time dependent problems, a full solution for two electrons is possible, but requires the use of supercomputer resources [231]. The typical approach is to expand the wavefunction in bi-spherical harmonics resulting in two radii that must be discretized to large distances increasing the size of the wavefunction to be stored. In Chap. 6 we discuss our recent developments and first tests of a two-electron code based on hyperspherical harmonics with the goal to potentially remove the need for supercomputers since only a single radius needs to be discretized.

Chapter 3

Modeling laser-atom interactions

In order to model laser-atom interactions, the regime of laser parameters must be considered. The studies presented in this thesis fall well within the so-called dipole oasis shown in Fig. 3.1 [151]. The dipole oasis shows the areas where the dipole and non-relativistic approximations are valid. The right edge of the dipole oasis in Fig. 3.1 occurs when the wavelength of light becomes comparable to the size of an atom, and the upper left limits correspond to the large amount of energy in a laser pulse. In the latter case, the magnetic components of the field become non-negligible resulting in the breakdown of dipole and non-relativistic approximations.

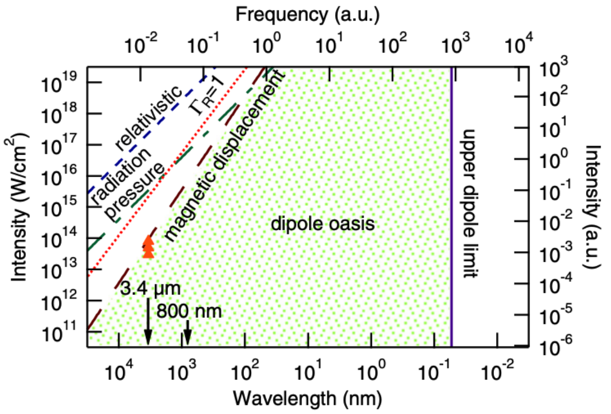

Figure 3.1: The dipole oasis shows the laser parameters that ensure that the dipole and non-relativistic approximations hold. (Figure from [151])

To study the dynamics of an electron interacting with and intense laser pulse, we solve the time-dependent Schrödinger equation (TDSE, Sec. 3.1). For the intense laser pulses used in this work, an analytic solution to the TDSE has not been found. Therefore, numerical solutions to the TDSE, described in Sec. 3.3, are used for the majority of the studies in this thesis. Numerical solutions to the TDSE are computationally intensive since they require tight sampling near the atomic core to ensure the ground state is properly represented, and large boxes to allow ionized wavepackets to remain on the grid. As a result, it is sometimes useful to apply approximate methods. At low intensities, typically below 10^{13} W/cm^2, the laser can be treated as a perturbation to the atomic potential allowing for approximate solutions to be obtained via perturbation theory (Sec. 3.2). At the other extreme when the laser pulse is much stronger than the atomic potential, the strong field approximation (SFA) can be used [133, 57, 205].

For the hydrogen atom, an analytic potential for the Coulomb interaction of the electron with the nucleus is known. However, for multi-electron atoms, one must use a single-active electron (SAE) potential to solve the TDSE. The SAE potentials used in this work are described in Sec. 3.4. Once a solution to the TDSE has been obtained, we use various observables, discussed in Sec. 3.5, to analyze the final wavefunction. Finally, the laser pulse definitions and frequency correction for ultrashort pulses is given in Sec. 3.5.

3.1 Time-dependent Schrödinger equation

The TDSE can be written as

$$i\frac{\partial}{\partial t}\psi(\mathbf{r},t) = \hat{H}\psi(\mathbf{r},t) \tag{3.1}$$

where $i = \sqrt{-1}$ is the imaginary number, $\hat{H}$ is the Hamiltonian which describes the system, and $\psi(\mathbf{r},t)$ is the time dependent wavefunction. The Hamiltonian for a system with N_e correlated electrons interacting with a laser field and N_n fixed nuclei is given by

$$\hat{H} = \sum_{e=1}^{N_e}\left(\frac{\hat{\mathbf{p}}_e^2}{2} + V_{las}(\mathbf{r},t) - \sum_{n=1}^{N_n}\frac{Z_n}{r_{e,n}}\right) + \sum_{e_1<e_2=1}^{N_e}\frac{1}{r_{e_1,e_2}} \tag{3.2}$$

where $\hat{\mathbf{p}}_e = (-i\nabla_e)$ is the momentum operator of the e^{th} electron, $V_{las}(\mathbf{r},t)$ is the laser operator, Z_n is the charge of the n^{th} nucleus, and $r_{i,j}$ is the Euclidean distance between particles i and j. The laser interaction is typically considered using both the dipole and non-relativistic approximation in either the length gauge ($V_{las} = -\mathbf{E}(t) \cdot \mathbf{r}$) or velocity gauge ($V_{las} = -\mathbf{A}(t) \cdot \hat{\mathbf{p}}_e/c$). Since no analytic solution for more than one electron in a central potential is known, as the problem is not separable, numerical methods are required. Solving the TDSE accurately in full dimensions for more than one electron is extremely difficult and next to impossible for three or more active electrons. For most studies, we make the single-active electron approximation (SAE) where all except one 'active' electron and the nuclei are fixed in space. A SAE potential generated by the nuclei and remaining electrons is then used to model the interaction of the active electron with the fixed electrons and nuclei. The SAE Hamiltonian of an atom interacting with a laser field therefore becomes

$$\hat{H} = \frac{\hat{\mathbf{p}}^2}{2} + V_{las}(\mathbf{r}, t) + V_{SAE}(r), \tag{3.3}$$

where $V_{SAE}(r)$ is the SAE potential. The exact form of the SAE potentials used in this work is given in Sec. 3.4. Extensions towards two-active electron calculations beyond the SAE approximation are discussed in Chap. 6. Finally, it is often convenient to split the problem into a time-independent field-free Hamiltonian ($\hat{H}_0$) and the time dependent laser field such that

$$\hat{H} = \hat{H}_0 + V_{las}(\mathbf{r}, t). \tag{3.4}$$

Eigenfunctions associated with H_0 can be used to analyze the results of a simulation.

3.2 Perturbation theory

In the case of a weak laser field (typically for intensities below 10^{13} W/cm^2) relative to the atomic potential the TDSE can be solved using perturbation theory (PT). In some cases, such as for the hydrogen atom, the corresponding terms of the perturbation series can be solved analytically. However, for many of the SAE potentials that we use there is no analytic solutions. In such a case, a numerical solution to the first-order terms of the series provides much of the same insight.

Therefore, it is advantageous to provide a general framework that can be used for both analytical and numerical solutions. We start by diagonalizing the field-free Hamiltonian H_0 to discretize both the bound (Sec. 3.3.6) and continuum states (Sec. 3.3.7). The result can be written as a Green's function

$$G_0(t,t') = \sum\!\!\!\!\!\!\!\!\int_g e^{-iE_gt} \left|\phi_g(t)\right\rangle \left\langle\phi_g(t')\right| e^{iE_gt'}, \tag{3.5}$$

where $|\phi_g(t)\rangle$ are the field free states (both bound and continuum), E_g is the energy of the state, and t denotes time. For some initial wavefunction $|\Psi_0(\mathbf{r},t)\rangle$, the consecutive orders of the PT can be obtained via

$$\left|\Psi_{i+1}(\mathbf{r},t)\right\rangle = \int_{-\infty}^{t} dt_1 G_0(t,t_1) V_{las}(t_1) \left|\Psi_i(\mathbf{r},t_1)\right\rangle \tag{3.6}$$

with $i = 0, 1, 2, \ldots$. The total wavefunction in Nth order can then be obtained via a sum such that

$$\left|\Psi(\mathbf{r},t)\right\rangle^{(N)} = \sum_{i=1}^{N} \left|\Psi_i(\mathbf{r},t)\right\rangle. \tag{3.7}$$

By taking $N \to \infty$, the resulting wavefunction is exact in the regime where the perturbation is small as compared to other interaction terms. However, if the perturbation is of similar order as compared to other terms in the Hamiltonian, the series will not converge to the correct answer leading to the breakdown of PT. The wavefunction obtained using PT can be used to extract observables (Sec. 3.5) in the same way as for a (full) numerical solution of the TDSE. Additionally, for laser-matter interactions PT offers the option to analyze the wavefunction of a particular order to extract further information about how many photons are involved in a process.

3.2.1 Selection rules

The wavefunction is often expanded in 3D spherical harmonics to take advantage of selection rules for interactions with an electric field. We proceed by considering the selection rules for length gauge ($V_{las} = -\mathbf{E}\cdot\mathbf{r}$). For simplicity, we consider a linearly polarized laser field along the z-axis, i.e.

$$V_{las} = -E_z z. \tag{3.8}$$

Noting that $z = r\cos(\theta)$ we obtain

$$V_{las} = -E_z r\cos(\theta) \tag{3.9}$$

$$= -2E_z r\sqrt{\frac{\pi}{3}}Y_1^0(\theta,\phi), \tag{3.10}$$

where $Y_\ell^m(\theta,\phi)$ is a spherical harmonic. This expansion can then be used to calculate the angular portion of a matrix element between two wavefunctions with V_{las} as a perturbation:

$$\left\langle Y_{\ell'}^{m'}\right| V_{las}\left|Y_\ell^m\right\rangle = -2E_z r\sqrt{\frac{\pi}{3}}\left\langle Y_{\ell'}^{m'}\right| Y_1^0\left|Y_\ell^m\right\rangle. \tag{3.11}$$

The integral over three spherical harmonics can be written as

$$\int_{4\pi} Y_{\ell_1}^{m_1*}Y_{\ell_2}^{m_2*}Y_L^M = \sqrt{\frac{(2\ell_1+1)(2\ell_2+1)}{4\pi(2L+1)}}\left\langle \ell_1,0,\ell_2,0|L,0\right\rangle\left\langle \ell_1,m_1,\ell_2,m_2|L,M\right\rangle, \tag{3.12}$$

where $\langle \ell_1,m_1,\ell_2,m_2|L,M\rangle$ is a Clebsch–Gordan coefficient. Thus, we get

$$\left\langle Y_{\ell'}^{m'}\right| V_{las}\left|Y_\ell^m\right\rangle = -E_z r\sqrt{\frac{(2\ell_1+1)(2\ell_2+1)}{3(2L+1)}}\left\langle \ell',0,1,0\middle|\ell,0\right\rangle\left\langle \ell',m',1,0\middle|\ell,m\right\rangle, \tag{3.13}$$

which is only non-zero for $\ell' = \ell \pm 1$ and $m' = m$. Therefore, the selection rules for a linearly polarized laser along the z-axis are given by $\Delta\ell = \pm 1$ and $\Delta m = 0$. Similarly, for a linearly polarized laser along either the x or y axis one gets $\Delta\ell = \pm 1$ and $\Delta m = \pm 1$. Finally, a circularly polarized laser in the xy-plane leads to $\Delta\ell = \pm 1$ and $\Delta m = 1$ for absorbing a photon from a right-handed circularly polarized field and $\Delta\ell = \pm 1$ and $\Delta m = -1$ for absorption of a photon from a left-handed circularly polarized laser field. By taking advantage of these selection rules, one can greatly reduce the size of a wavefunction used in a particular order of PT or in a numerical TDSE solution.

3.3 Numerical methods

For much of the parameter regime we are interested in, perturbation theory fails as an approximation method. Therefore, we have developed and implemented numerical solvers of the TDSE. As for most partial differential equations, numerical solutions to the TDSE have a relatively simple general form with the complexity hidden in the details. First, one chooses a basis/discretization to write down the solution, in our case the wavefunction. Next, the operators are expanded in the basis and written as a matrix. Then, one obtains a set of initial conditions at the start of the simulation, in our case typically a bound state of the atom or molecule. Finally, the initial condition is propagated in time with updates to the operating matrix between time steps. In this section, we will lay out the basis/discretization choices in Sec. 3.3.1, followed by a detailed discussion of the implementation in the remaining subsections. For the sake of simplicity, we will focus on single-active electron calculations in this section (for details on two-active electron calculation see Chapter 6).

3.3.1 Coordinate systems

The solution to a single-active electron calculation is three dimensional in space. The simplest and most general strategy would be to expand the wavefunction on a 3D grid in real space with the atom or molecule placed in the center. Such a grid is generated by discretizing each dimension (1D problem) with N grid points and then taking a Kronecker product producing a 1D vector that represents the full 3D Cartesian space. The derivative operators can then be discretized utilizing finite differences (discussed in the next section) and stored in a matrix. The implementation is relatively straight forward and there are no assumptions about the symmetry of the problem. However, this method has its flaws. If a potential has a singularity, such as the Coulomb potential at zero ($V = -1/r$), special care must be taken to avoid sampling that point. Additionally, the size of the calculation scales like N^3 when the number of grid points in each dimension (N) increases. Therefore, obtaining converged results for large atoms, which require smaller grid spacing to sample the core properly, and high intensities, which require larger box sizes to keep the wavefunction on the grid, becomes computationally impractical. It is, therefore, useful to consider the symmetries of the problem in question to greatly speed up the calculations. Two standard approaches are to utilize cylindrical or spherical coordinates.

The problem of an atom or a linear molecule aligned along a linearly polarized laser is cylindrically symmetric. Therefore, in this case using cylindrical coordinates is the natural choice. By choosing the laser polarization (and internuclear axis) along the z-axis, the solution in the angular coordinate ϕ is given by the initial condition and remains constant. Thus, one only needs to find a solution in the z and ρ dimensions numerically, reducing the problem to two dimensions. As a result, solutions scale like N^2 which significantly accelerates calculations as compared to a 3D Cartesian code.

However, in our studies we have actually found that spherical codes are often even faster. When written in spherical coordinates, the TDSE for a central potential (such as an atom) can be separated into a radial equation that contains the potential, and an angular portion that is independent of the potential. The angular solution can then be found analytically in the form of spherical harmonics and the radial solution is all that remains. For the hydrogen atom an analytic solution exists. However, in general for a radial potential it is not guaranteed that there is an analytic solution. Therefore, we expand the wavefunction in spherical harmonics and use finite difference to discretize the radial portion. Since the laser field only couples spherical harmonics according to the selection rules $\ell \to \ell \pm 1$ and $m \to m, m \pm 1$ depending on the polarization, the number of spherical harmonics needed is rather small (typically $\ell_{max} < 50$) with a weak dependence on laser intensity and wavelength. The result is a code that scales like $N\ell_{max}$ for linear polarization and $N\ell_{max}^2$ for arbitrary polarization. Since ℓ_{max} is small, the code typically scales like N as the pulse intensity, wavelength, or target atom is changed.

3.3.2 Finite difference

To discretize the spatial derivatives, we use finite difference. When using finite differences (FD), derivatives are represented by a set of coefficients called a stencil. The stencil provides the non-zero weights c_i for various sample points of the function. We can then write the second derivative of ψ known at various evenly spaced grid points labeled by n as

$$\frac{d^2}{dx^2}\psi_n \approx \frac{1}{\Delta x^2}\sum_i c_i \psi_i \tag{3.14}$$

The non-zero c_i coefficients are given in the table below for various orders of accuracy:

Order	c_{n-3}	c_{n-2}	c_{n-1}	c_n	c_{n+1}	c_{n+2}	c_{n+3}
2nd			-1	2	-1		
4th		$-1/12$	$4/3$	$-5/2$	$4/3$	$-1/12$	
6th	$1/90$	$-3/20$	$3/2$	$-49/18$	$3/2$	$-3/20$	$1/90$

Although it is possible to hard code the stencil weights, it becomes quite tedious particularly for high order stencils, non-uniform grids, and near boundaries where off-centered stencils are needed. Therefore, in this work we utilize the Fornberg method [68] to obtain the necessary stencil for a particular simulation. For the remainder of this discussion, we will assume that we are using second order derivatives. However, it is straightforward to expand it to higher order derivatives by adding more off-diagonal elements in matrices discussed in this section.

We begin with a 1D wavefunction and later extend to ND wavefunctions. Let us assume that we start with $\psi(x)$ known at various points along the x-axis spaced by a grid step of dx. We will label the points by n such that $\psi_n = \psi(x_0 + ndx)$ with x_0 being the smallest x value. Inserting this into Equation 3.14 we get

$$\frac{d^2}{dx^2}\psi_n \approx \frac{1}{\Delta x^2}\left(-\psi_{n-1} + 2\psi_n - \psi_{n+1}\right). \tag{3.15}$$

For the point ψ_{n+1} we can therefore write

$$\frac{d^2}{dx^2}\psi_{n+1} \approx \frac{1}{\Delta x^2}\left(-\psi_n + 2\psi_{n+1} - \psi_{n+2}\right). \tag{3.16}$$

This holds until we reach the other end of the grid. If we consider as boundary condition that $\psi(x_0 - dx) = \psi(x_N + dx) = 0$, then the points at $x_0 - dx$ and $x_N + dx$ can be simply left out of the matrix, which automatically imposes this boundary condition. For higher order stencils, an off centered difference formula is needed such that the boundary condition is only imposed at one point. The operator becomes a system of linear equations in the form of a matrix:

$$\frac{d^2\psi}{dx^2} \approx \frac{1}{\Delta x^2} \begin{bmatrix} 2 & -1 & & & \\ -1 & 2 & -1 & & \\ & \ddots & \ddots & \ddots & \\ & & -1 & 2 & -1 \\ & & & -1 & 2 \end{bmatrix} \begin{bmatrix} \psi_0 \\ \psi_1 \\ \vdots \\ \psi_{N-1} \\ \psi_N \end{bmatrix} \tag{3.17}$$

One uses a tensor product to produce the two and three dimensional versions of the operator.

3.3.3 Radial basis functions

A disadvantage of grid based methods, such as 3D Cartesian codes, is the structure of the grid. The required structured grids for FD do not give the freedom to refine the sampling in points of interest, such as near the nucleus, while sparsely sampling at large radii, due to the Kronecker product. Radial basis functions (RBF), on the other hand, is a meshless method that allows for sampling points, called nodes, to be placed anywhere [69]. The lack of required structure significantly reduce the number of points required to approximate the wavefunction. In this work the RBF method described below was applied to quickly obtain bound and continuum states. However, more work will be needed to allow for time propagation of the wavefunction in a laser field.

The RBF method starts with a set of N unique points in space called nodes that discretize the problem space. A stencil of size $n < N$ is then made for each node via its $n-1$ closest neighbors by using a k-nearest neighbors algorithm. For a RBF wavefunction $\phi(r)$, one defines the matrix

$$\mathbf{A} = \begin{bmatrix} \phi(|\mathbf{x}_1 - \mathbf{x}_1|) & \phi(|\mathbf{x}_2 - \mathbf{x}_1|) & \cdots & \phi(|\mathbf{x}_n - \mathbf{x}_1|) \\ \phi(|\mathbf{x}_1 - \mathbf{x}_2|) & \phi(|\mathbf{x}_2 - \mathbf{x}_2|) & \cdots & \phi(|\mathbf{x}_n - \mathbf{x}_2|) \\ \vdots & \vdots & & \vdots \\ \phi(|\mathbf{x}_1 - \mathbf{x}_n|) & \phi(|\mathbf{x}_2 - \mathbf{x}_n|) & \cdots & \phi(|\mathbf{x}_n - \mathbf{x}_n|) \end{bmatrix}, \tag{3.18}$$

where $\mathbf{x}_j$ represents the coordinates of a node. It is then possible to calculate the weights ω_j of an operator $\mathcal{L}$ evaluated at some point x_c by solving

$$\left[\begin{array}{ccc|cccccc} & & & 1 & x_1 & y_1 & z_1 & \cdots & e^{-\alpha r_1} \\ & \mathbf{A} & & \vdots & \vdots & \vdots & \vdots & & \vdots \\ & & & 1 & x_n & y_n & z_n & \cdots & e^{-\alpha r_n} \\ \hline 1 & \cdots & 1 & & & & & & \\ x_1 & \cdots & x_n & & & & & & \\ y_1 & \cdots & y_n & & & 0 & & & \\ z_1 & \cdots & z_n & & & & & & \\ \vdots & & \vdots & & & & & & \\ e^{-\alpha r_1} & \cdots & e^{-\alpha r_n} & & & & & & \end{array}\right] \left[\begin{array}{c} \omega_0 \\ \vdots \\ \omega_n \\ \hline \omega_{n+1} \\ \omega_{n+2} \\ \omega_{n+3} \\ \omega_{n+4} \\ \vdots \\ \omega_{n+m} \end{array}\right] = \left[\begin{array}{c} \mathcal{L}\phi(|\mathbf{x}-\mathbf{x}_1|)|_{\mathbf{x}=\mathbf{x}_c} \\ \vdots \\ \mathcal{L}\phi(|\mathbf{x}-\mathbf{x}_n|)|_{\mathbf{x}=\mathbf{x}_c} \\ \hline \mathcal{L}1|_{\mathbf{x}=\mathbf{x}_c} \\ \mathcal{L}x|_{\mathbf{x}=\mathbf{x}_c} \\ \mathcal{L}y|_{\mathbf{x}=\mathbf{x}_c} \\ \mathcal{L}z|_{\mathbf{x}=\mathbf{x}_c} \\ \vdots \\ \mathcal{L}e^{-\alpha r}|_{\mathbf{x}=\mathbf{x}_c} \end{array}\right] . \quad (3.19)$$

The matrix **A** imposes the RBF restrictions while the additional rows and columns allow for polynomials up to some degree (1, x, y, z, x^2, xy, $\cdots$) to be attached, improving the order of accuracy for the stencil. We can also attach other functions such as a Slater type orbital[1] ($e^{-\alpha r}$) to treat the discontinuity in the hydrogen atom wavefuction at $r = 0$. The weights ω_j for $j = 1, \ldots, n$ are used as the matrix elements in the operator matrix and weights with $j > n$ are discarded. When solving a PDE, it is often useful to take $x_c = x_1$ for each stencil such that the weights can be reused during time propagation. However, one can freely choose x_c allowing for the node placements to adapt to the PDE solution over time.

For the solution to the hydrogen atom we use 7^{th} order polyharmonic spline functions ($\phi(r) = r^7$). The node set is then chosen to emulate the standard spherical codes that are used. To do this, we discretize the radius at values $r_j = (j + dr)/2$ for $j = 0, \ldots, j_{max}$. A maximal determinate (MD) node set [211] for each radius is added to the total RBF node set. The MD node sets simulate the use of spherical harmonics, which drastically reduces the required number of nodes for the problem at hand.

---

[1] The method was developed in collaboration with Dylan Abrahamsen and Bengt Fornberg (Department of Applied Mathematics, University of Colorado Boulder).

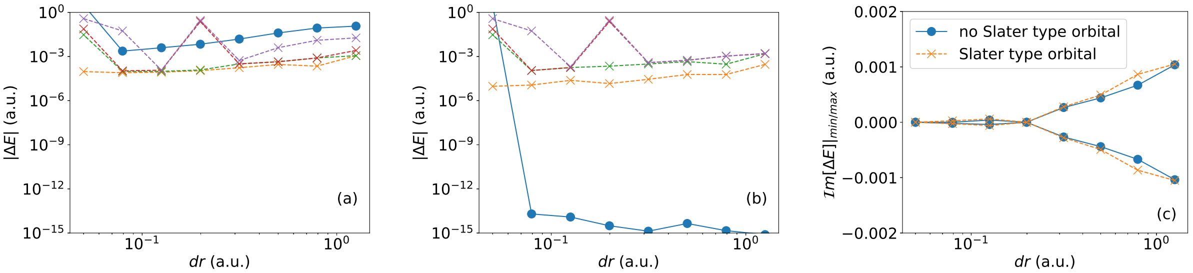

Figure 3.2: Panels (a) and (b) show the convergence of the lowest energy bound states in Hydrogen without and with an attached Slater type orbital respectively for various radial spacing (dr). The solid blue line show the error in the $1s$ state and dashed lines show the error for $n = 2$ states ($2s$, $2p_{-1}$, $2p_0$, and $2p_1$) in random order. Panel (c) shows the minimum and maximum imaginary part of the calculated bound state energies.

Choosing a fixed order of MD nodes for all values of r leads to two major issues. At small r, the nodes on each shell are much closer than the distance to the neighboring shells leading to the obstacle that stencils do not couple in the radial direction. This can be avoided by reducing the order of the MD node sets at small r so that the radial grid spacing (dr) is less than or equal to the average distance between neighboring MD nodes within a shell. The order of the MD node set then increases as r increases to the set maximum order. At large r, a similar issue occurs, where only nodes at fixed angles (θ and ϕ) with varying radii are chosen for a given stencil. To avoid this, each MD node set is quasi randomly rotated before being added to the total node set.

A final implementation issue is caused when attaching Slater type orbitals ($e^{-\alpha r}$) to the stencil. Since $e^{-\alpha r}$ becomes small quickly for increasing r, it can have variations below machine precision in a given stencil. The result is a linear dependence with the constant term producing poor stencils. To remedy this issue, $e^{-\alpha r}$ is only attached for stencils centered at radii with $e^{-\alpha r_1} > 10^{-10}$.

Convergence of the lowest five bound states using the RBF code are shown in Fig. 3.2. Results were obtained on a mesh with an extension of 30 a.u. in radial direction, 8th order MD node set, 7th order PHS RBF, attached polynomials up to 3rd order, and a stencil size of 54 nodes. Panels (a) and (b) shows the error in the states energy without and with a Slater type orbital e^{-r} being attached. The addition for the Slater type orbital give machine precision for the ground state (blue line) and improves the $2s$ (orange line) energy until nonphysical states appear with $dr < 0.1$. The $2p_m$ states see little benefit from inclusion of the Slater type orbital.

Fig. 3.2(c) shows the maximum and minimum imaginary part of the energy of the five calculated states. The splitting occurs for the states with $m \neq 0$ when meshes other than a Cartesian lattice are used. The states with $\mathcal{I}m[E] < 0$ lead to unstable time propagation for the Crank-Nicolson method used in this work. Further work on mesh generation, hyperviscoisty, and/or time propagation methods will be needed to study time dependent problems with the RBF method.

3.3.4 Numerical integration

For equally spaced grids used in our finite difference methods, either the midpoint or trapezoid rule are used for numerical integration. For both methods the integration is performed by

$$\int_x f(x')dx' \approx \sum_{i=1}^{n} c_i f(x_i) \tag{3.20}$$

where $f(x_i)$ is the value of the function at x_i and x is the integration interval. The midpoint rule is used if the grid is placed at half grid points on the interval (i.e. $x_i = (2i+1)dx/2$ for $i = 0, 1, 2, ..., n$). In this case $c_i = 1/dx$ for all grid points. For the trapezoid rule the grid points sample the ends of the integration range resulting in $c_0 = c_n = 1/2dx$ and $c_i = 1/dx$ for $i = 1, \ldots, n-1$.

In the case of the RBF code, the MD node set comes with a provided integration weight for the angular integration and the radial integration is done via the midpoint rule. For the spherical code, the angular integration is done analytically since spherical harmonics are orthonormal.

3.3.5 Boundary conditions

The wavefunction at large r must decay to zero for it to be normalizable. Therefore, we set the wavefunction to zero at r_{max} and increase the value of r_{max} until a converged result is obtained (Sec. 3.3.9). Exterior complex scaling (ECS), which is discussed in the next paragraph, insures that the wavefunction decays prior to hitting the boundary. For the Cartesian code, this is the only boundary condition needed. For the cylindrical and spherical codes, another boundary condition

$$\begin{array}{cc|cccccc|}
c_{n-2} & c_{n-1} & c_n & c_{n+1} & c_{n+2} & & & \text{(a)} \\
 & c_{n-2} & c_{n-1} & c_n & c_{n+1} & c_{n+2} & & \\
 & & c_{n-2} & c_{n-1} & c_n & c_{n+1} & c_{n+2} & \\
 & & & \ddots & \ddots & \ddots & \ddots & \ddots
\end{array}
\qquad
\begin{array}{c|cccccc|}
c_{n-1} & c_n & c_{n+1} & c_{n+2} & c_{n+3} & & \text{(b)} \\
c_{n-2} & c_{n-1} & c_n & c_{n+1} & c_{n+2} & & \\
 & c_{n-2} & c_{n-1} & c_n & c_{n+1} & c_{n+2} & \\
 & & \ddots & \ddots & \ddots & \ddots & \ddots
\end{array}$$

Figure 3.3: The finite difference stencil near the edge of the grid. Panel (a) shows how in the fourth order finite difference the stencil extends beyond the grid leading to a boundary condition being imposed at two points. Panel (b) shows the non-centered 4th order stencil that enforces a single boundary condition.

at $r = 0$ is required. The cylindrical code the grid is chosen such that the grid points are given by $x_j = (2j + 1)dx/2$ with $j = 0, 1, 2, \ldots, n$ and the boundary condition of $\psi(-x) = \psi(x)$ is used. In the spherical code, however, $x_j = jdx$ with $j = 1, 2, 3, \ldots, n$ and the boundary condition $\psi(0) = 0$ is used. To enforce a boundary condition a "ghost node" is implemented. The ghost node is a grid point that falls outside of the grid. If the ghost node is set to zero, the coefficient is left off the matrix, and the boundary condition is met. If the stencil extends beyond the grid by more than one point, such as in 4th order finite difference, the stencil is shifted so that only one point is beyond the grid and it retains the same width (see Fig. 3.3). For the cylindrical case, the ghost node is taken at $\psi(-dx/2)$. Since $\psi(-x) = \psi(x)$, the stencil coefficient at $\psi(-dx/2)$ is added to the coefficient for $\psi(dx/2)$ which imposes the boundary condition.

To absorb any outgoing wave packets, we utilize an exterior complex scaling method (ECS, [92]) on the outer portion of the grid. This is equivalent to changing the spatial step used in finite difference from $x_{n+1} = x_n + dx$ to $x_{n+1} = x_n + e^{i\eta}dx$. In test calculations we have found that $\eta = \pi/4.0$ works well. The result is an exponential decay of the wavefunction in the absorbing region. Obtaining the finite difference weights in the transition and ECS region is done by implementing the Fornberg method [68] using complex numbers.

3.3.6 Bound state calculations

The bound states of the system are simply the eigenstates of the Hamiltonian with energies less than zero. Therefore they satisfy the equation

$$\hat{H}\phi_i = E_i\phi_i \tag{3.21}$$

where $\hat{H}$ is the Hamiltonian, E_i is the energy, and ϕ_i is the bound state assuming $E_i < 0$. To solve for the bound states, we use the Krylov-Schur method that is implemented in the SLEPc library [97, 208]. When obtained using SLEPc, the states have a random complex phase associated with them. The phase is physically irrelevant unless one is creating a superposition or comparing results of calculations that use different bound state sets such as a TDSE and PT result. To avoid issues, it is best to use a single bound state calculation for each project. The populations obtained via projections onto excited bound states at the end of a simulation are, for example, useful to analyze and verify selection rules for a given laser polarization.

The coordinate system used for bound state calculations will control which states are generated. For spherical calculations, each ℓ block can be calculated independently and the results are independent of m. Likewise, results of cylindrical 2D calculations are obtained for fixed m quantum number. Finally, Cartesian 3D calculations will provide all n, ℓ, and m states in one calculation with the states being oriented at a random angle.

3.3.7 Continuum states

The continuum has states at all levels with energy larger than zero in the physical problem. However, when we solve the TDSE numerically, due to the finite extension of the grid the continuum is represented via a discrete set of states. For example, in spherical coordinates the TDSE solution on the grid requires $\psi(0) = \psi(r_{max}) = 0$ (for the radial coordinate). The boundary condition is the same as for an infinite square well with a bottom in the shape of $V(r)$. The continuum states are, therefore, a distorted solution to the infinite square well problem. We can obtain these states by the same method as used in the bound state calculations providing a discrete set of energies that represent the continuum. This method is used for the numerical PT solution discussed in Sec. 3.2.

When calculating a photoelectron (energy or angular) spectrum, however, it is advantageous to be able to select the energy of the continuum wave. For this case, we utilize the shooting method [215] to obtain a continuum wave at a given energy. The method is given via an ODE which one solves as follows. The wavefuction at $r = 0$ is set to zero by the boundary condition. The first point at $r_0 = dr$ is set to an arbitrary value (in this case 1) giving

$$\phi_{kl}(r_0) = 1. \tag{3.22}$$

with $k = \sqrt{2E}$. The second point is then obtained by

$$\phi_{kl}(r_1) = \phi_{kl}(r_0)\left(dr^2\left[\frac{\ell(\ell+1)}{r^2} + 2V(r_0) - 2E\right] + 2\right). \tag{3.23}$$

Each additional point can be found by

$$\phi_{kl}(r_{i+1}) = \phi_{kl}(r_i)\left(dr^2\left[\frac{\ell(\ell+1)}{r^2} + 2V(r_i) - 2E\right] + 2\right) - \phi_{kl}(r_{i-1}). \tag{3.24}$$

Once the wavefunction has been obtained, we match the asymptotic solution to that for a hydrogen-like atom

$$\phi_{kl}(r \gg 1) \to \sin\left[kr - \frac{l\pi}{2} + \frac{Z}{k}\ln(2kr) + \delta_{kl}\right]. \tag{3.25}$$

The continuum state oscillates between -1 and 1 at $r \gg 1$ leading to a normalization of

$$A = \left[\frac{1}{\sqrt{|\phi_{kl}(r)|^2 + \left|\frac{\phi'_{kl}(r)}{(k+\frac{Z}{kr})}\right|^2}}\right]_{r=r_{max}}. \tag{3.26}$$

Finally, we extract the phase shift δ_{kl} by

$$\delta_{kl} = \left[\arg\left(\frac{i\phi_{kl}(r) + \frac{\phi'_{kl}(r)}{(k+\frac{Z}{kr})}}{(2kr)^{iZ/k}}\right) - kr + \frac{l\pi}{2}\right]_{r=r_{max}}. \tag{3.27}$$

This continuum state can then be used to obtain the photoelectron spectrum by

$$P(k,\theta,\phi) \propto \left|\sum_{l,m} Y^*_{l,m}(\theta,\phi)\int e^{-i\delta_{kl}}(i)^l\phi_{kl}(r)^*\psi(r,t)dr\right|^2. \tag{3.28}$$

3.3.8 Time propagation

Time propagation is often performed using the split-operator method where the Hamiltonian ($\hat{H}$) is split into its spatial dimensions, e.g. along (z) and perpendicular (ρ) to the polarization direction of a linearly polarized laser. Similarly, the problem can be split along x, y, and z for an arbitrary laser polarization. The resulting propagation scheme is given by

$$\psi(\mathbf{r}, t + \Delta t) \approx e^{-i\hat{H}_\rho \frac{\Delta t}{2}} e^{-i\hat{H}_z(t)\Delta t} e^{-i\hat{H}_\rho \frac{\Delta t}{2}} \psi(\mathbf{r}, t), \tag{3.29}$$

where

$$e^{-i\hat{H}\Delta t} \approx \frac{1 - i\frac{\Delta t}{2}\hat{H}}{1 + i\frac{\Delta t}{2}\hat{H}}. \tag{3.30}$$

This produces a set of tridiagonal matrices which can be solved with $\mathcal{O}(\mathcal{N})$ operations and $\mathcal{O}(\mathcal{N})$ memory. However, parallelization of such a method on a modern supercomputer with distributed memory can be cumbersome, requiring multiple all-to-all Message Passing Interface (MPI) messages during each time step which strongly reduces its scalability.

Instead, we avoid splitting the Hamiltonian and propagate the total Hamiltonian in time using a second order Crank-Nicolson scheme where

$$\psi(\mathbf{r}, t + \Delta t) \approx e^{-i\hat{H}\Delta t} \psi(\mathbf{r}, t). \tag{3.31}$$

We note that the Crank-Nicolson method is not tridiagonal (due to a tensor product) and a direct solution would require $\mathcal{O}(\mathcal{N}^3)$ operations and $\mathcal{O}(\mathcal{N}^2)$ memory which is significantly more than in the split operator method. However, the system of equations in the full Crank-Nicolson method is sparse and iterative methods can be used to vastly accelerate the time propagation. We utilize the Generalized Minimal Residual Method (GMRES), implemented in PETSc [8, 9], which solves the sparse system of linear equations in $\mathcal{O}(\mathcal{N}\log(\mathcal{N}))$ operations and $\mathcal{O}(\mathcal{N})$ memory. The PETSc library makes it straightforward to parallelize the Crank-Nicolson method on modern supercomputers with distributed memory. On a local supercomputer (Summit, CU Boulder), we achieved super-linear scaling up to 3,000+ cores (see Fig. 3.5) allowing us to complete simulations in a matter of hours that would take weeks running on a high-end workstation.

dx	Z=1	Z=2	Z=3	Z=4	Z=5
4.000e-01	5.995e-03	6.217e-02	1.590e-01	2.568e-01	3.416e-01
2.000e-01	3.035e-04	5.995e-03	2.612e-02	6.217e-02	1.086e-01
1.000e-01	1.041e-05	3.035e-04	1.841e-03	5.995e-03	1.392e-02
5.000e-02	2.225e-07	1.041e-05	7.810e-05	3.035e-04	8.331e-04
2.500e-02	-2.663e-09	2.225e-07	2.290e-06	1.041e-05	3.204e-05
1.250e-02	-7.101e-10	-2.672e-09	2.992e-08	2.225e-07	8.341e-07

Table 3.1: The relative error of the ground state energy for a hydrogen-like atom with a nuclear charge Z. A grid spacing around 0.1 produces well converged results for $Z = 1$. Excited states have lower relative error.

3.3.9 Convergence studies

Numerical solutions to the TDSE require a convergence study to ensure that the final results are reliable. One does this by varying a free parameter, such as grid spacing, spherical harmonic expansions, time step, etc. until the observable in question remains within some tolerance. It is possible to use an error calculation and reduce it until a numerical tolerance is met. However, graphical convergence, when two lines plotted on top of each other are indistinguishable, is often a more practical convergence criteria. In Table 3.1 we show how the error of the ground state energies of a hydrogen-like atom with difference charge (Z) converges with decrease of the grid spacing when using 4th order finite difference.

For a fixed target, it is advantageous to use the highest order finite difference that is stable. Fig. 3.4 shows the convergence of the $1s$, $2s$, and $3s$ energy levels of the hydrogen atom using 2^{nd} through 20^{th} order FD. The slope of the convergence for each curve matches the order of the method. 20^{th} order FD achieves a converged result with the largest grid spacing leading to a shorter calculation. It is therefore advantageous for bound state calculations. However, the Hamiltonian for higher order methods become increasingly non-Hermitian near the boundaries leading to unstable time propagation for 6^{th} or higher order FD. Therefore, we have used 4^{th} order for the vast majority of calculations that we have performed in this work.

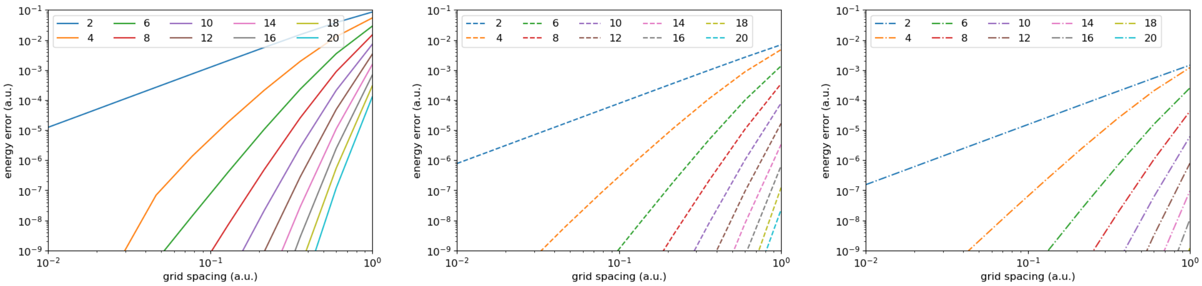

Figure 3.4: Convergence with respect to grid spacing for various orders of FD for the 1s (a), 2s (b), and 3s (c) states in hydrogen atom.

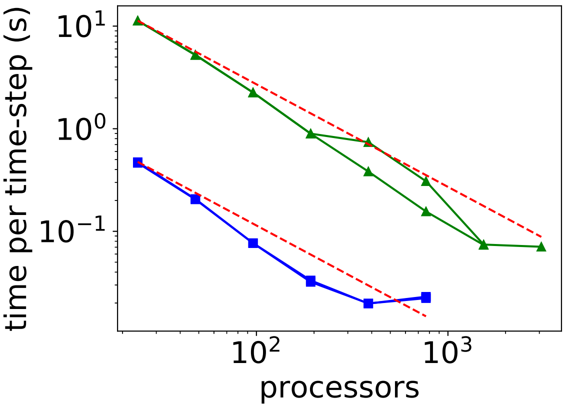

Figure 3.5: Scaling results for present Crank-Nicolson method. Two runs each for calculations with 1 million (blue with squares) and 15 million grid points (green with triangles) have been performed. Note that the scaling improves with increasing number of grid points.

3.3.10 Parallel Computing

Many simulations can be performed on a laptop or small desktop, however, the largest calculations, such as those done in Cartesian coordinates or utilizing bicircular laser polarizations, benefit from supercomputing resources. Since the code is implemented utilizing the PETSc library and through the use of MPI, we are able to take advantage of the distributed memory of a modern supercomputer. Linear scaling, i.e. the computational time is cut in half when twice as many processors are used, is often the benchmark for code scaling. Our code obtains super-linear (better than linear) scaling on the Summit supercomputer up to 3,000+ processors (see Fig. 3.5). This is

Atom	z	Z_c	c	a_1	b_1	a_2	b_2
H	1	-	-	-	-	-	-
He	1	1	2.0329	0.3953	6.1805	-	-
Ne	1	9	0.8870	-9.9286	1.3746	-5.9950	3.7963

Table 3.2: Coefficients of SAE potentials in Eq. 3.33 for hydrogen, helium, and neon from [204].

possible due to the increased size of cache memory as the number of CPUs increases. This allows for calculations that would take a month on a desktop to be completed in a few hours on a supercomputer. Additionally, the supercomputing systems come with a large increase in the available RAM (often on the order of terabytes) significantly reducing the memory limitations on calculation size.

3.4 Single-active electron potentials

For many atoms, full treatment of Eq. 3.2 is impractical, if not impossible. Since in many ultrafast laser-atom interactions, primarily a single valence electron is involved, in this case it becomes advantageous to treat only the single-active electron in the potential produced by freezing the remaining $N-1$ electrons in their ground state reducing the problem from 3^N-dimensions down to three dimensions. The resulting Hamiltonian becomes

$$\hat{H} = -\frac{\mathbf{p}^2}{2} + V_{SAE}(\mathbf{r}) + V_{las}(t)\,, \tag{3.32}$$

where $V_{las}(t)$ is the laser operator and $V_{SAE}(\mathbf{r})$ is the SAE potential. The SAE potentials utilized in this work take the form [204]

$$V_{SAE}(\mathbf{r}) = -\frac{z}{r} - \frac{Z_c e^{-cr}}{r} - \sum_n a_n e^{-b_n r}. \tag{3.33}$$

The coefficients are obtained by fitting to a potential obtained through density functional theory (DFT). In Table 3.2 we show the coefficients for SAE potentials used in this thesis.

3.5 Observables

The wavefunction, given as numerical solution of our calculations, is not experimentally observable. It is therefore necessary to extract experimentally relevant information via observables. For a given observable $\hat{O}$, the expectation value is obtained by calculating $\langle\Psi|\,\hat{O}\,|\Psi\rangle$. In this work we have studied high order harmonic generation (HHG) spectra, ionization, bound state populations, and photoionization (energy and angular) distributions.

HHG spectra are obtained by first calculating the dipole acceleration using the Ehrenfest theorem

$$\hat{a}_j = \frac{\partial V(\mathbf{r})}{\partial j}\,, \tag{3.34}$$

where $j \in x, y, z$ are the Cartesian coordinates. For the hydrogen atom, $\hat{a}_j = j/r^3$ where r is the distance from the nucleus. Then the HHG spectrum is obtained by taking a Fourier transform such that

$$\hat{O}_{HHG}(\omega)_j = \left| \int_{-\infty}^{\infty} e^{-i2\pi\omega t} \langle\Psi(t)|\, \hat{a}_j \,|\Psi(t)\rangle \, dt \right|^2 . \tag{3.35}$$

Bound state populations are obtained using

$$P_{\phi_i} = |\langle\phi_i|\Psi\rangle|^2 \,, \tag{3.36}$$

where ϕ_i is the field-free bound state and Ψ is the wavefunction.

At the beginning of each simulation, the wavefunction is normalized to 1 such that

$$\langle\Psi(t_0)|\Psi(t_0)\rangle = 1\,. \tag{3.37}$$

Ionization probabilities can then be calculated in two manners. In the first method one propagates the wave function after the pulse allowing the ionized part to be absorbed at the ECS boundary. The ionization probability is then obtained by taking

$$P_{ion} = 1 - |\,\langle\Psi|\Psi\rangle\,|^2 \tag{3.38}$$

since $\langle\Psi(t_0)|\Psi(t_0)\rangle = 1$. This method is slow to converge and can lead to numerical round off errors due to extended time propagation. The preferred method for calculating the ionization probability is

$$P_{ion} = 1 - \sum_i |\langle \phi_i | \Psi \rangle|^2 \tag{3.39}$$

where ϕ_i is a bound state and the sum over i includes all states the grid supports with a real part of the energy that is less than zero. Therefore, the ionization probability can be obtained at the end of the pulse reducing the computational expense and numerical error.

The photoelectron spectrum (energy and angular) can are obtained at the end of the pulse by calculating

$$P(k, \theta, \phi) \propto \left| \sum_{l,m} Y^*_{l,m}(\theta, \phi) \int e^{-i\delta_{kl}} (i)^l \phi_{kl}(r)^* \psi(r, t) dr \right|^2 , \tag{3.40}$$

where $\phi_{kl}(r)$ is a continuum wave, δ_{kl} is a phase shift, and $Y_{l,m}(\theta, \phi)$ is a spherical harmonic. The angular distribution is obtained by plotting the angular dependence (θ and ϕ) for a given energy. The energy distribution is obtained by integrating over θ and ϕ (see Sec 3.3.7 for details on obtaining $\phi_{kl}(r)$ and δ_{kl}).

3.6 Frequency shift[2]

Few-cycle laser pulses are used in many interesting strong-field applications (for reviews, see e.g., [197, 225, 238, 187, 242, 249]). For example, high-order harmonics and (isolated) attosecond pulses are generated, ultrafast atomic and molecular dynamics as well as charge transfer and exciton dynamics can be induced and time resolved, molecular structure can be imaged on ultrashort time scales, or chemical reactions may be controlled. Therefore, light sources generating ultrashort intense laser pulses in different regions of the spectrum, at extreme ultraviolet [79], ultraviolet [48], optical [67], near-infrared [259, 178, 179] and infrared wavelengths [111, 200, 176], have been developed over the past decades. The simulation of the time-dependent response of matter to a few-cycle pulse, e.g. via the numerical solution of the corresponding time-dependent Schrödinger equation (TDSE), can however crucially depend on the definition of the electric field $E(t)$ used. To achieve quantitative agreement between theory and experiment, the potential issues present in

---

[2] The content of this subsection has been also published in J. Venzke, T. Joyce, et al. PRA **98**, 063409 (2018).

both numerical calculations and experiment must be well understood and minimized.

As pointed out by Chelkowski and Bandrauk [35], the representation of $E(t)$ via an envelope function times a trigonometric function may lead to a non-vanishing potential $A(t)$ at the end of the pulse. This inconsistency can be resolved by first defining the magnitude of the vector potential $A(t)$ as (we use Hartree atomic units: $e = m_e = \hbar = 1$) [35]:

$$A(t) = \frac{cE_0}{\omega_A} f(t) \cos(\omega_A t + \phi_A), \tag{3.41}$$

where f, ω_A, c, E_0 and ϕ_A are the envelope function, central frequency, speed of light, peak electric field amplitude, and carrier envelope phase of the vector potential, respectively. The prefactors ensure that the peak intensity of the laser field is $I = \frac{c}{8\pi} E_0^2$. The magnitude of the electric field is then obtained via the derivative:

$$\begin{aligned} E(t) =& -\frac{1}{c}\frac{\partial}{\partial t} A(t) \\ =& E_0 f(t) \sin(\omega_A t + \phi_A) - \frac{E_0}{\omega_A}\frac{\partial f(t)}{\partial t} \cos(\omega_A t + \phi_A). \end{aligned} \tag{3.42}$$

The expression for the electric field, Eq. 3.42, includes a term that depends on the time derivative of f and, hence, may have significant effects in the case of few-cycle pulses. As we will show below, a direct implication is that the central frequency of the electric field spectrum, ω_E, is not equal to ω_A. The frequency shift $|\omega_E - \omega_A|$ is a purely electromagnetic effect that is directly related to the definition of the electric field via the vector potential given in Eq. 3.42. For long pulses, the frequency shift is small, but it increases as pulse duration decreases. Note, that in experiment typically the central laser frequency of the electric field ω_E is measured and reported, while in numerical calculations it is useful to define the laser pulse via the vector potential and the related central frequency ω_A. It is therefore important to study what impact, if any, the difference between the central frequencies has on numerical calculations, or on the interpretation of theoretical results.

By solving the time-dependent Schrödinger equation both numerically, as well as within perturbation theory, we show below that theoretical results obtained for linear processes, such as excitation and ionization, involving few-cycle pulses with the same value for the central frequencies

ω_A and ω_E do not coincide. Furthermore, we find that the frequency shift is also noticeable for nonlinear processes, such as two-photon excitation and high-order harmonic generation, and it scales with the number of photons involved. Our results also demonstrate that it is the central frequency of the electric field ω_E that is the physical relevant quantity for the interpretation of laser driven quantum mechanical processes. Therefore, the frequency shift should be taken into account when setting the central frequency ω_A of the vector potential in a numerical calculation or, more generally, a theoretical analysis.

3.6.1 Estimation of frequency shift

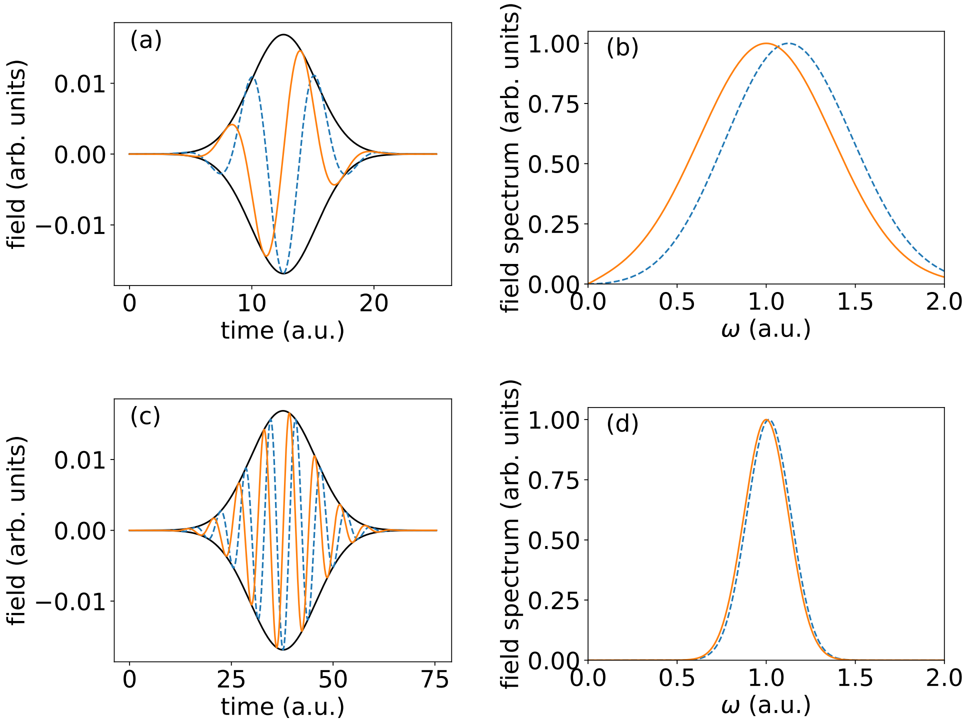

Figure 3.6: Temporal (left) and spectral (right) distributions of vector potential (solid lines) and electric field (dashed line) for pulses with FWHM of one cycle (top), and three cycles (bottom) at central frequency $\omega_A = 1.0$ a.u. of the vector potential. Also shown is the Gaussian envelope of the vector potential. (Figure from [236])

The frequency shift due to the difference in central frequencies is illustrated in Fig. 3.6, where the vector potential A and the electric field E, obtained from Eqs. (3.41) and (3.42) for a Gaussian

Name	Envelope Function $f(t)$	N/N_{FWHM}	γ_2
Gaussian	$e^{-(t/T)^2}$	0.849	0
Cos^2	$\begin{cases} \cos^2\left(\frac{t}{T}\right) & -\frac{\pi}{2} \leq \frac{t}{T} \leq \frac{\pi}{2} \\ 0 & \text{otherwise} \end{cases}$	0.723	-0.594
Cos^4	$\begin{cases} \cos^4\left(\frac{t}{T}\right) & -\frac{\pi}{2} \leq \frac{t}{T} \leq \frac{\pi}{2} \\ 0 & \text{otherwise} \end{cases}$	0.777	-0.381
Sech	$\text{sech}(\frac{t}{T})$	1.19	2.00

Table 3.3: Several common analytic pulse envelopes. The conversion factor between N, as defined in Eq. 3.45 (number of cycles within one standard deviation to either side of the maximum), and the more typical N_{FWHM} (number of cycles in the full-width half-maximum of the electric field) is given. The last column shows the excess kurtosis γ_2, defined in Eq. 3.47, which is independent of the pulse duration T. (Table from [236])

envelope $f(t)$, are compared in both the time and frequency domain. While the temporal behavior is satisfactory, the spectral distributions reveal different central frequencies. We define the central frequency ω_A (ω_E) as the location of the maximum in the spectral density $|\tilde{A}(\omega)|$ ($|\tilde{E}(\omega)|$). The discrepancy is much greater for the one-cycle full-width at half-max (FWHM) pulse (top), than for the three-cycle FWHM pulse (bottom).

For the further analysis, we note that in order for the central frequencies to be well-defined and consistent with the definition of ω_A in Eq. 3.41, we make several assumptions about the envelope $f(t)$:

- $f(t)$ is nonnegative and continuously differentiable,
- $f(t)$ falls off at least exponentially for large $|t|$,
- $f(t)$ contains no appreciable Fourier components larger than ω_A.

These assumptions could be relaxed significantly, but they are sufficient for the present discussion and all practical purposes. The ratio of the central frequencies is given by the leading terms of an expansion in $1/N$ as[3] :

$$\frac{\omega_E}{\omega_A} = \frac{1+\sqrt{1+4(\pi N)^{-2}}}{2} + \frac{\gamma_2}{6\pi^4}N^{-4} + O(N^{-6}) \tag{3.43}$$

$$\approx \frac{1+\sqrt{1+4(\pi N)^{-2}}}{2}. \tag{3.44}$$

Here

$$N \equiv \frac{\omega_A}{\pi}\sqrt{\frac{\int_{-\infty}^{\infty}(t-t_0)^2 f(t)dt}{\int_{-\infty}^{\infty} f(t)dt}}. \tag{3.45}$$

is the number of cycles within one standard deviation to either side of the pulse center, with

$$t_0 \equiv \frac{\int_{-\infty}^{\infty} t f(t)dt}{\int_{-\infty}^{\infty} f(t)dt}, \tag{3.46}$$

and lastly γ_2 is the excess kurtosis of the envelope

$$\gamma_2 \equiv \frac{\left[\int_{-\infty}^{\infty}(t-t_0)^4 f(t)dt\right]\left[\int_{-\infty}^{\infty} f(t)dt\right]}{\left[\int_{-\infty}^{\infty}(t-t_0)^2 f(t)dt\right]^2} - 3. \tag{3.47}$$

Note that N is proportional to the more typical N_{FWHM} (number of cycles in the FWHM of $f(t)$), but the ratio N/N_{FWHM} depends on the shape of the envelope (c.f., Table 3.3).

Eq. 3.43 indicates that the ratio ω_E/ω_A depends on the number of cycles and the pulse shape, but it is independent of peak intensity, carrier envelope phase, ellipticity, and ω_A itself. In fact, the first term of the expansion, Eq. 3.43, is a very accurate estimate even for single cycle pulses, showing that the shift is nearly independent of pulse shape. This can be seen from the comparison between the predictions based on Eq. 3.43 with the exact frequency shift for a variety of pulse shapes in Fig. 3.7. The exact shift was calculated by numerically maximizing the analytic expressions for $|\tilde{E}(\omega)|$. The slight dependence on pulse shape is visible in the inset; the differences are described well by the correction term in Eq. 3.43, which involves the excess kurtosis γ_2.

In the next section, we demonstrate that ω_E is the physically observable and relevant central frequency. Therefore, when modeling the interaction with a pulse using Eqs. (3.41) and (3.42), one

---

[3] The analytic work for obtaining the frequency correction and perturbation theory calculations was preformed by T. Joyce.

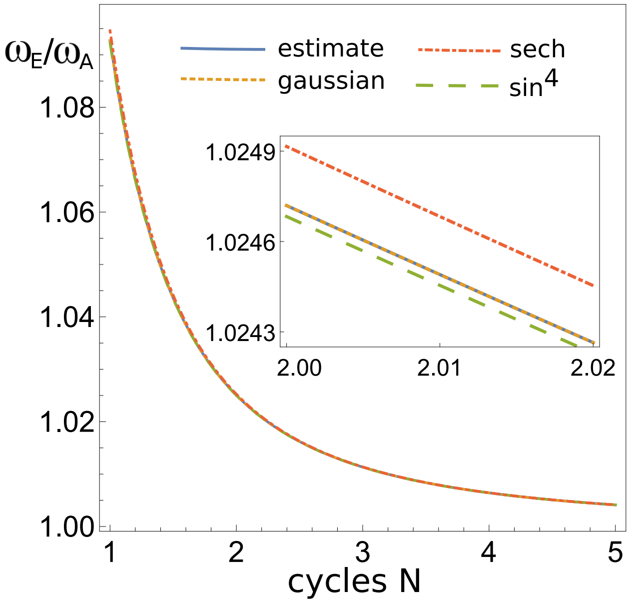

Figure 3.7: Ratio ω_E/ω_A as a function of the normalized number of cycles N defined in Eq. 3.45. The numerical results were calculated by maximizing $\tilde{E}(\omega)$ for Gaussian (dotted line), sech (dashed-dotted line), and $\sin^4$ (dashed line) envelopes and are compared with the simple analytic estimate (solid line) given in Eq. 3.43. The inset reveals a slight dependence on envelope shape, which can be attributed to the correction term in Eq. 3.43. (Figure from [236])

should determine ω_A such that it corresponds to the correct ω_E. There are two different methods to do this. The first one is to specify N, and use Eq. 3.43 to obtain ω_A. However since N depends implicitly on ω_A through Eq. 3.45, the envelope $f(t)$ must be stretched in time by the same factor such that N remains unchanged. The second method is to specify $f(t)$ instead of N. In that case, substituting Eq. 3.45 into Eq. 3.43 and solving for ω_A yields

$$\omega_A \approx \omega_E - \frac{\int_{-\infty}^{\infty} f(t)dt}{\omega_E \int_{-\infty}^{\infty} (t-t_0)^2 f(t)dt}. \tag{3.48}$$

Greater accuracy could be obtained in either case by including the correction term in Eq. 3.43; however, the results in Fig. 3.7 show that this is in general not necessary.

3.6.2 Applications

In this section we present results of numerical calculations and first-order perturbation theory which exemplify effects of the frequency shift on observables related to excitation, ionization and high harmonic generation induced by short laser pulses. The frequency shifts obtain using first-order perturbation theory and numerical calculations agree well with our analytical predictions shown in Section 3.6.1. To this end, we solved the 3D one-electron time-dependent Schrödinger equation (TDSE) in velocity gauge:

$$i\frac{\partial}{\partial t}\psi(\mathbf{r},t) = \left[\frac{\mathbf{p}^2}{2} - \frac{\mathbf{A}(t)\cdot\mathbf{p}}{c} + V(\mathbf{r})\right]\psi(\mathbf{r},t) \tag{3.49}$$

and length gauge

$$i\frac{\partial}{\partial t}\psi(\mathbf{r},t) = \left[\frac{\mathbf{p}^2}{2} + \mathbf{E}(t)\cdot\mathbf{r} + V(\mathbf{r})\right]\psi(\mathbf{r},t) \tag{3.50}$$

for atomic hydrogen with a soft-core Coulomb potential

$$V(\mathbf{r}) = -\frac{1}{\sqrt{\mathbf{r}^2+\alpha^2}}. \tag{3.51}$$

We consider a linearly polarized laser pulse within the dipole approximation, so $\mathbf{A}(t) = A(t)\hat{z}$ and $\mathbf{E}(t) = E(t)\hat{z}$. Taking advantage of azimuthal symmetry, the wavefunction can be represented in 2D cylindrical coordinates ρ and z. We used the second order finite difference method for spatial derivatives and the fully implicit second order Crank-Nicholson method for time propagation. The laser field magnitudes $A(t)$ and $E(t)$ were defined as in Eq. 3.41 and Eq. 3.42, with a Gaussian envelope function $f(t)$. Specifically,

$$A(t) = \frac{E_0 c}{\omega_A}\sin(\omega_A t)e^{-(2t/\tau)^2\ln 2}\ , \tag{3.52}$$

where τ is the FWHM pulse duration. The results presented below were obtained in velocity gauge, but additional test calculations in length gauge have confirmed that the results are gauge invariant.

In all calculations for single photon ionization, excitation and high harmonic generation we used $\alpha = 0.029$ a.u., a grid spacing of 0.1 a.u., and a time step of 0.1 a.u. The soft core parameter is used to match the ground state energy to that of atomic hydrogen, given by $E_{1s} = -0.5001$ a.u. on the grid, and an excited state energy of $E_{2p} = -0.12504$ a.u. To ensure the wavefunction remains on the grid for our calculation of the photoelectron spectrum, the grid extended 500 a.u. in the ρ-direction and 1000 a.u in the z-direction, with an exterior complex scaling absorbing boundary in the outer 50 a.u for single photon ionization (Sec. 3.6.2.1). The excitation (Sec. 3.6.2.2) and high harmonic generation (Sec. 3.6.2.3) calculations were preformed on a grid that extended over 100 a.u. in the ρ-direction and 200 a.u. in the z-direction, with an absorbing boundary over the outer 5 a.u.

3.6.2.1 Single photon ionization

First, we consider single photon ionization of the hydrogen atom by a few-cycle laser pulse with peak intensity 10^{13} W/cm^2 and central frequency $\omega_{\text{central}} = 2.0$ a.u. The central frequency is implemented either by setting $\omega_A = \omega_{\text{central}}$ or setting $\omega_E = \omega_{\text{central}}$, using the method described in the previous section. Photoelectron momentum spectra $P(k)$ were obtained by the following procedure: the TDSE was propagated for five times the FWHM pulse duration plus an additional 100 a.u. in time, then all bound states with principle quantum number $n \leq 8$ were projected out, and lastly the remaining unbound wavepacket ψ_{ionized} was projected onto Coulomb wave functions up to $l_{\text{max}} = 5$. That is,

$$P(k) = \sum_{l=0}^{l_{\text{max}}} \left| \int F_l(-\tfrac{1}{k}, kr) Y_{l0}^*(\hat{r}) \psi_{\text{ionized}}(\vec{r}) d^3\vec{r} \right|^2 . \tag{3.53}$$

The results in Fig. 3.8 show that in fact the photoelectron spectra for central frequency $\omega_A = 2$ a.u. (solid lines) and $\omega_E = 2$ a.u. (dashed lines) do not agree due to the frequency shift. As expected, the discrepancy is larger for 2 cycle FWHM (panel (b)) than for 10 cycle FWHM (panel (a)) pulses. These results however raise the question whether the central frequency of the vector potential ω_A or the central frequency of the electric field ω_E is the relevant quantity for further physical interpretation or a comparison with experimental data. To address this question, we consider the resonant population transfer between bound states by analyzing results of numerical calculation as well as those obtained using first-order perturbation theory in the next subsection.

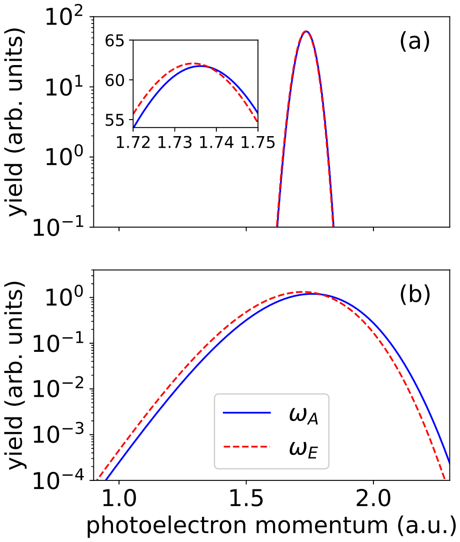

Figure 3.8: Photoelectron spectra $P(k)$ as function of photoelectron momentum obtained for interaction of hydrogen atom with laser pulses at central frequencies $\omega_A = 2$ (dashed line) and $\omega_E = 2$ (solid line) and duration of (a) 10 cycles and (b) 2 cycles FWHM. (Figure from [236])

3.6.2.2 Excitation

Next, we examine transitions to the $n = 2$ orbitals in the hydrogen atom as a function of both pulse length and central frequency of the vector potential (ω_A) and the electric field (ω_E). Typically, the excitation probability is largest when the central frequency of the laser matches the resonant frequency for n_p photon absorption, given by

$$\omega_{\text{res}} = |E_{\text{final}} - E_{\text{initial}}|/n_p, \tag{3.54}$$

where E_{final} and E_{initial} are the energy of the final and initial state, respectively. In view of the predicted frequency shift between the central frequencies ω_A and ω_E, we therefore expect that the results for resonant excitation will provide insights into the physical relevance of ω_A vs. ω_E.

Within first order perturbation theory, the excitation probability is given by:

$$\begin{aligned} P_{i\to f} &= |\tilde{A}(\omega_{\text{res}})|^2 \left(\frac{\mu\omega_{\text{res}}}{c}\right)^2 \\ &= \frac{\pi}{\ln 2}\left(\frac{\mu E_0 \omega_{\text{res}}\tau}{4\omega_A}\right)^2 \left[e^{-(\omega_A-\omega_{\text{res}})^2\tau^2/(16\ln 2)} \qquad - e^{-(\omega_A+\omega_{\text{res}})^2\tau^2/(16\ln 2)}\right]^2, \end{aligned} \tag{3.55}$$

Here we have used the pulse defined in Eq. 3.52 and $\mu = 2^{7.5}3^{-5}$ is the transition dipole for the hydrogen $1s \rightarrow 2p$ transition. Eq. 3.55 shows that the excitation probability $P_{i\rightarrow f}$ is not maximized at $\omega_A = \omega_{\text{res}}$, due to the prefactor of ω_A^{-2}. This prefactor originates from Eq. 3.41, where it ensures that the peak intensity is held fixed as ω_A changes.

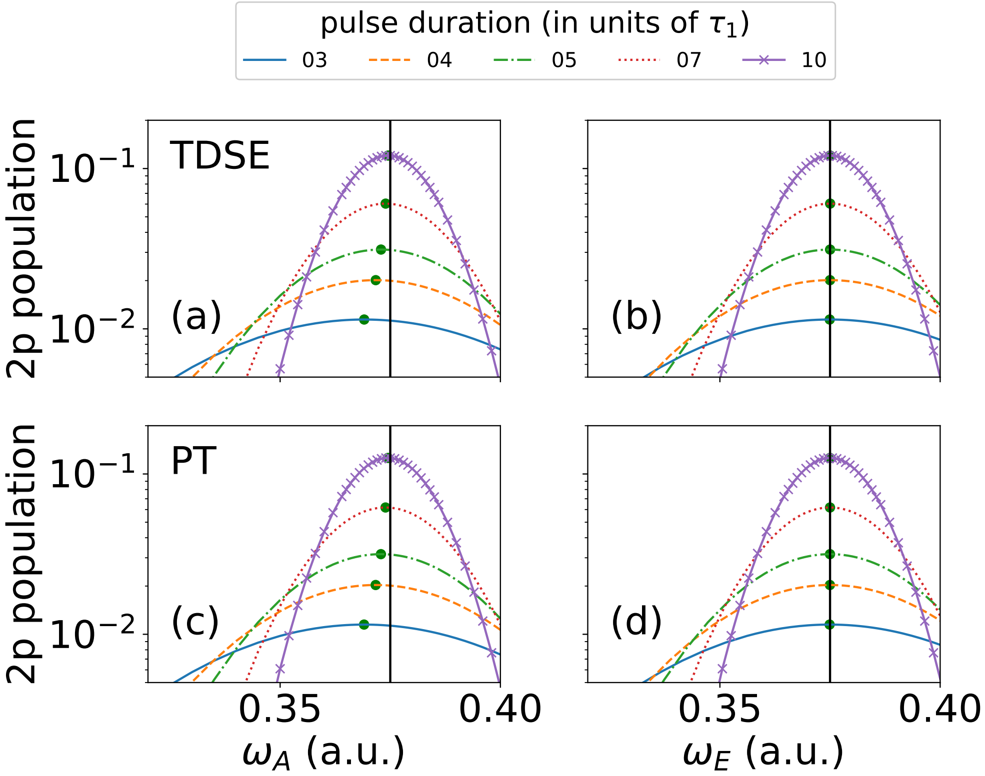

Figure 3.9: Population in $2p$ state following one-photon excitation of hydrogen atom with a laser pulse as a function of ω_A (left) and ω_E (right) for different pulse lengths at peak intensity 10^{12} W/cm^2. Each line represents results obtained for a fixed pulse duration in terms of $\tau_1 = 405$ as. The results from time-dependent Schrödinger equation (TDSE) calculations (a,b) and predictions within first-order perturbation theory (PT) (c,d) are in excellent agreement. The vertical line marks the energy difference between $2p$ and initial $1s$ state. The green dots indicate the maximum excited state population for each pulse duration. (Figure from [236])

We have also obtained the population in the $2p$ state due to single photon excitation by direct numerical solution of the TDSE. These numerical results are presented together with those obtained within first order perturbation theory, Eq. 3.55, in Fig. 3.9 as function of ω_A (left column) and ω_E (right column) for various pulse lengths. The pulse length τ is measured in multiples of the period associated with the resonant frequency

$$\tau_{n_p} = \frac{2\pi}{\omega_{res}} = \frac{2\pi n_p}{|E_{\text{final}} - E_{\text{initial}}|}, \tag{3.56}$$

such that $\tau_1 \approx 405$ attoseconds, $\tau_2 \approx 811$ attoseconds and so on for the $1s \to 2p$ transition. For long pulses the peak in the population (marked by a green dot) occurs at the expected frequency ω_{res} (marked by vertical line) for a resonant transition in all distributions. When the pulse length is decreased, the peak in the distributions as a function of ω_E (right column) remains at ω_{res}. In contrast, the peak shifts significantly towards lower frequencies in the distributions as a function of ω_A (left column) due to the frequency shift. We note that the results of our numerical calculations (upper row) are in excellent agreement with those obtained using first-order perturbation theory (lower row) and indeed both reveal the same dependence on the central frequencies ω_A and ω_E. Thus, the differences in the distributions as functions of ω_A and ω_E are not a numerical artifact but are due to the frequency shift. Furthermore, the observed shift agrees with our estimate obtained in the previous section. Thus, we can conclude that the central frequency of the electric field is the physically relevant quantity for interpreting laser induced excitation processes.

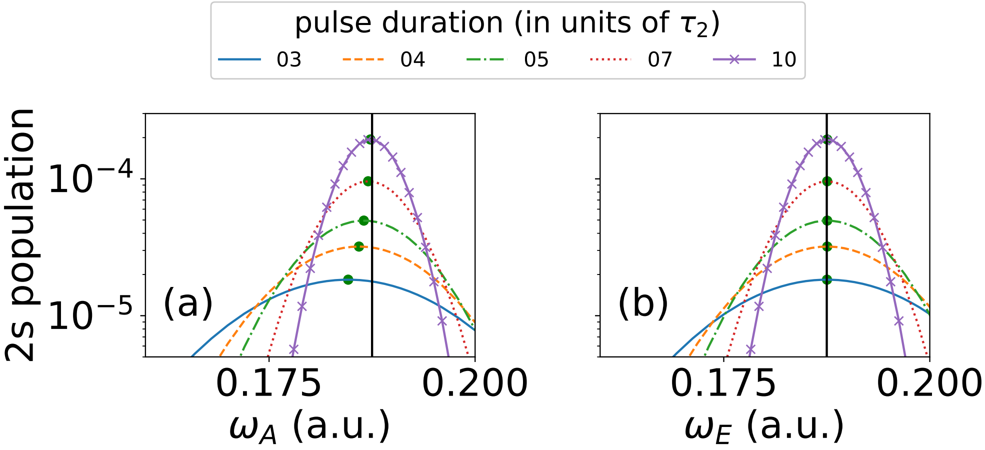

Figure 3.10: Numerical results for population in $2s$ state following two-photon excitation with $\tau_2 = 811$ as. The vertical line marks half of the energy gap between $1s$ and $2s$ representing the resonance condition for the two photon process. Other parameters are the same as in Fig. 3.9. (Figure from [236])

These conclusions are further supported by our numerical results for two-photon excitation from the $1s$ to the $2s$ state in Fig. 3.10. Whereas the peak of the population as a function of ω_E (panel b) occurs at ω_{res}, independent of the pulse duration, the peak of the population as a function of ω_A once again shifts to lower frequencies in Fig. 3.10(a). We note that, if the population as function of ω_A in Figs. 3.9 and 3.10 were used to determine the energy difference $|E_{\text{final}} - E_{\text{initial}}|$, the error caused by the frequency shift would be twice as much in the two-photon case as in the one-photon case, accounting for the difference in τ_{n_p}. This indicates that multiphoton processes may be affected by the frequency shift even more than few-photon processes. To further illustrate this point, we examine high harmonic generation.

3.6.2.3 High harmonic generation

Finally, we consider a highly nonlinear laser induced process. High harmonic generation (HHG) in atoms can be described as absorption of an odd number of photons leading to the excitation of a electron, followed by the emission of a single photon as the electron recombines into the ground state. Based on the results above, we expect that in this nonlinear process the frequency shift $\Delta\omega$ between ω_A and ω_E will lead to a shift of the energy of the n_pth harmonic by $n_p\Delta\omega$. In our calculations the HHG spectrum has been obtained by a Fourier transformation of the time dependent dipole acceleration along the laser polarization direction. A Hanning filter was used to return the dipole acceleration to zero at the beginning and end of the simulation.

Fig. 3.11 shows the various harmonics in a HHG spectrum as a function of the number of cycles in the driving laser pulse at a peak intensity of 1×10^{14} W/cm^2 and central frequencies $\omega_A = 0.0625$ a.u. (upper panel) and $\omega_E = 0.0625$ a.u. (lower panel), corresponding to a wavelength of 730 nm. The spectrum consists of odd harmonics and additional emission lines due to the population of excited states during the interaction with the laser pulse. While we will focus on the generation of harmonics, we note that the emission lines occur at photon energies between the 5th and 9th harmonics. The corresponding field-free energy differences between the excited states and the ground state in our numerical model of the hydrogen atom are marked, as reference, by white vertical dashed lines.

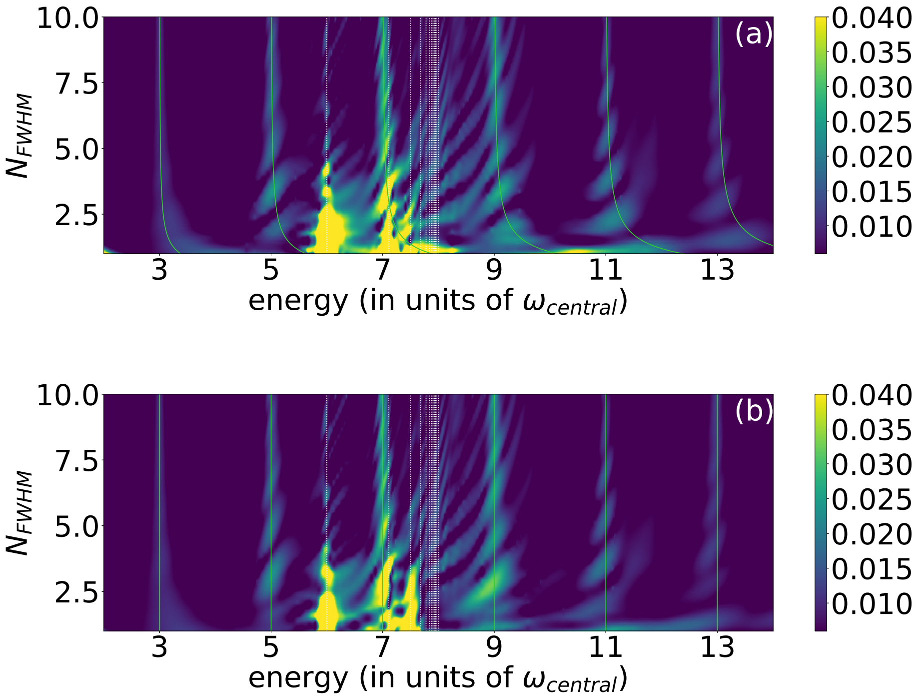

Figure 3.11: HHG spectrum at driver wavelength 730 nm ($\omega_{\text{central}} = 0.0625$ a.u.) vs. number of cycles N_{FWHM}. In the upper plot the central frequency $\omega_A = \omega_{\text{central}}$ while in the lower panel $\omega_E = \omega_{\text{central}}$. The vertical white dashed lines mark field-free transition energies between excited states and the ground state, while the green solid lines mark the harmonic energies $n_p\omega_E$ with respect to the central frequency of the electric field. (Figure from [236])

In the spectrum as function of multiples of ω_A (panel a) one can see that the centers of the harmonics do shift to energies larger than $n_p\omega_A$, as the pulse duration decreases. In fact, the energies of the harmonics follow the analytical predictions for $n_p\omega_E$ (green solid lines). As expected, the shift increases with larger the harmonic number. In contrast, in the HHG spectrum obtained as multiples of ω_E (panel b) the centers of the harmonics remain at the same energy, i.e. $n_p\omega_E$ (green solid lines), as the pulse duration decreases. This confirms the importance of the shift between the central frequencies of the vector potential and the electric field in nonlinear processes driven by ultrashort pulses. Furthermore, the HHG results confirm that the central frequency of the electric field ω_E is the physical relevant quantity for the interpretation of light induced processes. Consequently, if in a numerical simulation or theoretical analysis the vector potential is set via Eq. 3.41, it is necessary to consider the frequency shift between ω_A and ω_E to avoid a misinterpretation of the results. Our analytical estimates of the frequency shift in Eq. 3.43 and Eq. 3.48 provide formulas to obtain ω_A from the physically relevant ω_E.

To summarize, we have shown that the definition of the electric field of a laser pulse via the derivative of the vector potential, which guarantees that both quantities vanish at the beginning and end of the pulse, implies that the central frequencies of the spectral distributions of the vector potential and electric field do not coincide. In our analysis we have derived an analytical estimate of the frequency shift, which shows that the shift mainly depends on the number of cycles in the pulse and becomes most relevant for few-cycle pulses. Utilizing results of numerical simulations and first-order perturbation theory we have analyzed how the frequency shift affects excitation, ionization and high harmonic generation induced by short laser pulses. The effect is found to be most noticeable in nonlinear strong-field processes since the frequency shift scales with the number of photons involved. Both, numerical results and predictions based on first-order perturbation theory agree well with each other and confirm that the central frequency of the electric field is the physically relevant quantity for the interpretation of the light induced processes. Thus, the shift should be taken into account when setting the central frequency of the vector potential in numerical simulations to avoid potential misinterpretation of the theoretical results, specifically when compared to experimental data. Eq. 3.43 and Eq. 3.48 provide formulas to obtain ω_A from the physically relevant ω_E.

Chapter 4

Imaging attosecond wave packet dynamics with photoelectrons

In the previous chapter, we provided an overview of the theoretical methods used to study ultrafast laser-matter interactions. In this chapter, we will apply these tools to the process of atomic ionization. We will focus on the impacts of ultrashort pulses on few photon ionization, asymmetries that appear in the angular dependence of the emission of photoelectrons due to ionization of atoms in single states and superposition states, and a method to obtain amplitude and phase information of a wavefuction representing attosecond motion using photoelectron angular distributions (PAD).

In these studies we will consider interaction with lasers similar to experimentally available ultrabright light sources such as free-electron lasers [218] and table-top laser systems based on high-order harmonic generation [197, 38] that deliver high-intensity pulses of few- or sub-femtosecond duration. Nowadays, laser pulses with a duration as short as a few tens of attoseconds have been achieved experimentally [256, 37]. Isolated attosecond pulses or trains of attosecond pulses have been generated from the vacuum ultraviolet to the soft X-ray wavelength regime and the polarization of such pulses can nowadays be controlled. This recent progress in ultrafast laser pulse technology makes it possible to probe, steer and control the dynamics of electrons in atoms, molecules and solids [238, 187, 31, 249, 201, 188]. To name a few examples, the time-resolved measurement of the electron emission in the photoelectric effect has been realized [34, 216, 129, 226, 114]. Using an isolated attosecond pulse or a train of extreme-ultraviolet attosecond pulses to ionize an atom along with an infrared laser field interferograms have been measured to obtain information about phases of electron wavepackets, an important milestone towards reconstructing the wavefunctions of atoms [206, 161]. By extracting the phase and amplitude via application of photoelectron spectroscopy recently the birth of a photoelectron through a Fano resonance has been observed on the attosecond time scale [83].

The production of extreme-ultraviolet (EUV) pulses using high harmonic generation (HHG) and free-electron lasers (FEL) has led to a resurgence of multiphoton ionization studies in the perturbative intensity regime recently [177, 230, 220, 193, 65, 214, 86, 66, 112, 113, 153, 207, 82, 47, 103, 104, 25, 243]. Along with experimental techniques, such as velocity map imaging [131, 210] or cold target recoil ion momentum spectroscopy [229], the detection of angle-resolved emission of the photoelectron following few-photon ionization of atomic and molecular targets has become possible [153]. Probing atoms and molecules in their ground or excited states with ultrashort laser pulses opens a new regime where several linear and nonlinear ionization pathways compete and interfere [112, 153, 82, 47, 104, 25, 243, 235]. PADs are determined by the amplitudes and phases of the partial waves of all pathways contributing to the emission at a given energy into a given solid angle. PADs and related anisotropy parameters are therefore useful observables to obtain quantitative insights in the relative strength of the different pathways and their competition. This has been demonstrated in the past for the competition between resonant and non-resonant two-photon ionization pathways [112, 113, 153] and for one- and two-photon ionization channels [82, 47, 25]. In the simple case of photoionization from a single state, anisotropy and asymmetry parameters have been used in the past to identify and analyze interesting physical effects. For example, a significant circular dichroism via the asymmetry in the forward-backward electron emission from bromocamphor molecules induced by circularly polarized light has been identified [26]. Observation of the breakdown of the symmetry in the photoelectron emission of argon has been shown in the region of the Cooper minimum [110]. Interference between resonant and non-resonant pathways [112] or direct and autoionizing channels [39] can be identified via anisotropy and asymmetry parameters. Other examples can be found in double photoionization [160] or molecular vibrations and chirality [75] and applications range from studies of coherent control [199] to the characterization of ultrashort laser pulses [35].

In this chapter, we examine the PADs of electrons which are emitted when atoms are ionized by few photon processes during the interaction with ultrashort pulses with the goal to image attosecond dynamics. In Sec. 4.1 we study the impact of the increased bandwidth of these ultrashort pulses on the PAD for a two-photon process including intensity and pulse jitter studies. In this initial ionization study from a single state (i.e., the ground state of the atom), we will perform the analysis with conventional asymmetry and anisotropy parameters. Next, in Sec. 4.2 we extend these studies to the more general case of ionization from a superposition state. Since in these situations application of the conventional parameters fail, we will present a new set of generalized asymmetry parameters (GAPs) that is an extension of the standard front-back asymmetry parameter. It allows to study interference in the emission from states with differing magnetic quantum numbers that can be prepared via excitation with circularly and elliptically polarized laser pulses. Finally, we will consider the time dependent ionization of helium atom, prepared in the $1s - 2p_1$ superposition, and present tools capable of reconstructing dynamics that repeat over a 200 attosecond period from the PADs in Sec. 4.3.

4.1 Short pulse effect in ionization of ground-state helium atom[1]

Two-photon ionization of atoms, specifically the helium atom, has been studied in theory and experiment in the past, first concerning total ionization yields [177, 230, 220, 193, 65, 214, 66] and, more recently, with a focus on photoelectron angular distributions [112, 113, 153, 25]. It has been shown, that the PADs strongly depend on the pulse duration or, equivalently, the spectral width of the EUV pulses. Initially, theoretical studies by Ishikawa and Ueda revealed that the competition between resonant and nonresonant pathways depends on the pulse width [112, 113]. Changes in the PADs for 1 - 21 fs pulses at photon energies below the first ionization energy were characterized by the even anisotropy parameters β_2 and β_4. Via these parameters the relative phase between the s- and d-wave packets for the photoelectron emission can be determined. Related experimental work at the SPring-8 Compact SASE Source test accelerator verified the co-presence of the two pathways

---

[1] The content of this section has been also published in J. Venzke et al., J. Phys. B. **53**, 085602 (2020).

[153]. Very recently, Boll et al. extended these studies, covered a much wider photon energy range and explored the impact of radial and angular electron correlation [25]. They showed that in the low-energy regime a single-active electron picture is valid while at higher energies in the regime of autoionizing states angular correlations play a major role for the understanding of the PADs.

The ongoing quest in shortening pulses at extreme- and deep-ultraviolet wavelengths towards the single-cycle regime in duration are achieved via large spectral widths. Such broadband energy pulses give rise to competition between one- and two-photon (as well as three-photon) ionization processes for emission at a given energy. As mentioned in Ref. [25], in helium atom this leads to the additional interference of the *s*- and *d*-wave packets due to two-photon absorption with a *p*-wave packet from single photon absorption. In this section, we study the transition regime between single photon ionization and two-photon absorption. We first show how in this regime the PADs quickly change over a small window of pulse duration, about 1 cycle in full width at half maximum (FWHM). The variation is reflected in the anisotropy parameters β_i ($i = 1, 2, 3$ and 4), which show the transition as well as the interference between the ionization pathways. The dependence on pulse duration, photon energy as well as photoelectron energy is studied. We further consider how variation of pulse parameters, such as the carrier-envelope-phase (CEP), the peak intensity, and the partial coherence of FEL pulses, do impact the anisotropy parameters. Finally, we briefly study at which intensities three-photon ionization, which occurs for these large bandwidth pulses as well, may become observable. In order to accurately account for the different pulse parameters, we have performed simulations based on the time-dependent Schrödinger equation. Since a recent study has shown that for pulses with central photon frequency below the first ionization potential of the helium atom the single-active electron (SAE) picture remains valid [25], we have used a SAE potential for our numerical simulations.

We solve the time dependent Schrödinger equation for the interaction of a electron in a spherically symmetric SAE potential with the electric field $\mathbf{E}$ of a linearly polarized laser pulse (along the $\hat{z}$-direction) in dipole approximation and length gauge as described in Chapter 3. We have expanded the wavefunction in spherical harmonics up to $l_{max} = 20$ with $m = 0$ due to the symmetry of the problem. The radius is discretized using fourth order finite difference method with a grid spacing of 0.05 a.u. and a maximum radius of 300 a.u. We utilized the exterior complex scaling method on the outer 30 a.u. of the grid with a time step of 0.01 a.u. and apply a SAE potential given in Eq. 3.33. Our numerical simulations have been performed for laser pulses with central frequencies at or near to the energy difference between the field-free $1s$ and $2p$ state of the helium atom. In our SAE model of helium the ground state energy is -0.944 a.u., while the $2p$ energy is -0.128 a.u. To ensure that the electric field integrates to zero [35], we define the vector potential following the procedure described in Sec 3.6.

As result from our ab-initio numerical calculations we obtain the wavefunction at the end of the interaction with the laser pulse. Via projection on continuum states we can then determine the ionization probability as well as photoelectron energy and angular distributions. If more than one pathway, such as one- and two-photon ionization, contribute to the emission of the photoelectron at a given energy in a given direction, our numerical simulations do not allow to separate the respective probabilities for each channel easily. This is in contrast to calculations based on perturbation theory, in which the amplitude for each pathway is evaluated and can be analyzed separately. In order to analyze the dominant pathways for photoemission as functions of intensity, photoelectron energy and pulse duration, we therefore determine anisotropy parameters (β-parameters), which provide quantitative insights in the different pathways involved as well as the interference between them [82, 47, 25].

It has been shown [136] that the photoelectron angular distribution for an isotropic target is given by:

$$P(E,\theta) = \frac{\sigma(E)}{4\pi}\left[1 + \sum_{j=1}^{n} \beta_j(E) P_j(\cos(\theta))\right] \tag{4.1}$$

where θ is the angle of electron emission with respect to the polarization direction of the laser field, while $\sigma(E)$ is the ionization probability at E and P_j are the Legendre polynomials. The anisotropy parameters β_j depend on the amplitudes of the different pathways leading to emission of the photoelectron (for explicit expressions, see [82]). For combinations of one- and two-photon ionization processes, that will be the focus of our study, contributions from the first four β_j-parameters are expected. The contributions related to the odd polynomials indicate interference between partial waves resulting from one- and two-photon absorption. We also note that the impact of three-photon ionization, that we will briefly consider below, is expected to show up in the anisotropy parameter β_5 and higher order parameters.

We have determined the anisotropy parameters in our calculations using Equation (4.1) as follows. At the end of the simulations of the time-dependent Schrödinger equation we obtained the photoelectron angular distribution at a given momentum k by projecting the wavefunction onto the field-free continuum states on the numerical grid. The numerically obtained PAD has been then projected onto the j-th Legendre polynomial P_j $(j = 1, \ldots, 5)$ and the results have been normalized using the total ionization probability σ.

4.1.1 Results and Discussion

Following a general discussion of the processes involved in Sec. 4.1.1.1, we present PADs and related anisotropy parameters for pulses having a Gaussian envelope. The results are analyzed, in view of a competition between one- and two-photon ionization, as a function of pulse duration, central frequency and peak intensity in Sec. 4.1.1.2. Impact of shot-to-shot fluctuations of the carrier-envelope-phase, the peak intensity and the partial coherence of FEL pulses are studied in Sec. 4.1.1.3.

4.1.1.1 Impact of one-, two-, and three-photon processes in ultrashort pulses

To first illustrate the impact of the one-, two- and three-photon ionization pathways on the emission of the photoelectron in ultrashort laser pulses, let us consider an emission induced by a pulse with central frequency ω_0 tuned to the $1s - 2p$ energy gap. The broad energy spectrum of an ultrashort Gaussian pulse is schematically depicted in the panels of Figure 4.1 centered about the energy of the $2p$-state. Absorption of two photons by an electron in the ground state at the central frequency ω_0 (c.f., Figure 4.1(b)) will lead to its emission at energy $E = 2\omega_0 - |E_{1s}|$. If

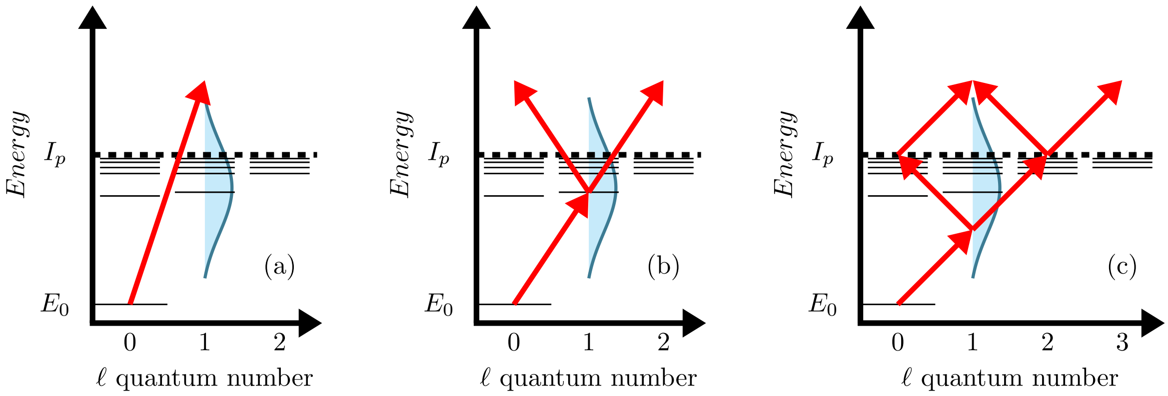

Figure 4.1: Schematic representation of one- (a), two- (b), and three-photon (c) ionization in an ultrashort pulse. The Gaussian distribution shows the spectral width of the ultrashort pulse centered about the energy of the $2p$-state. The red arrows represent the photon absorption pathways, and the black lines depict some of the resonant structure of the helium atom. (Figure from [235])

the bandwidth of the pulse is broad enough (i.e., the pulse duration is sufficiently short) ionization of a photoelectron with the same photoelectron energy can occur via absorption of one photon with energy $2\omega_0$ (c.f., Figure 4.1(a)) or via absorption of three photons with energy $\frac{2}{3}\omega_0$ (c.f., Figure 4.1(c)). We note that besides the two-photon and three-photon pathways with absorption of photons of equal energies, there exist more such pathways to a final photoelectron energy E for absorption of photons with unequal energy as long as the sum of the photon energies is equal to $2\omega_E$.

The occurrence of the one- and three-photon processes requires a broad spectral bandwidth of the pulse. That means, for long pulses we expect that only the two-photon ionization process is present. If the pulse is shortened to a few optical cycles, both the one- and three-photon channels become effective, since the probability of photon absorption at energies away from the central frequency increases. In the perturbative intensity regime the probability for a n-photon process scales as I^n, where I is the intensity of the pulse. We therefore expect that at a given ultrashort pulse duration at low intensities the one-photon process dominates over the two-photon process in an ultrashort laser pulse. As the intensity increases, first the two-photon process should then become dominant, before at significantly higher intensities contributions from the three-photon process will become detectable. In this section, we mainly study the transition from one- to two-photon processes, while the influence of the three-photon process will be given minor attention.

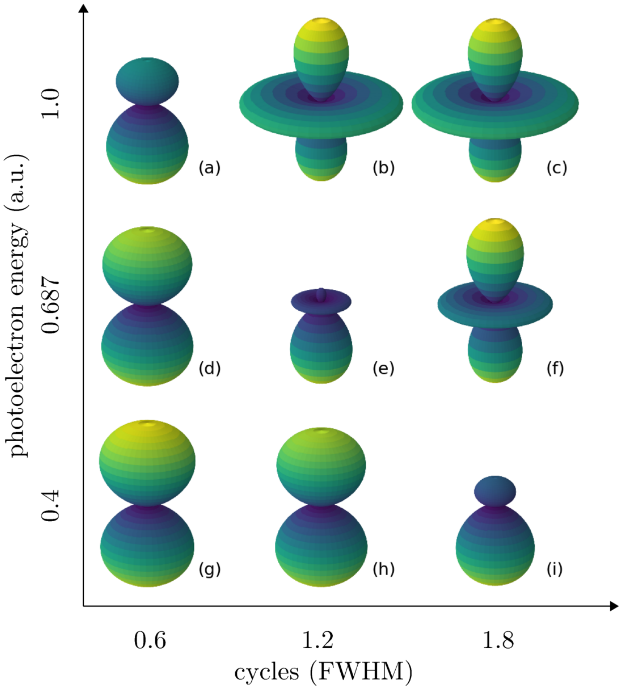

Figure 4.2: Photoelectron angular distributions for helium atom ionized by laser pulses at central photon energy $\omega_0 = 22.2$ eV, peak intensity $I_0 = 10^{11}$ W/cm^2, carrier-to-envelope phase $\phi = 0$ and three different pulse durations: $N = 0.6$ FWFM cycles (0.112 fs, left column), $N = 1.2$ FWHM cycles (0.224 fs, middle column) and $N = 1.8$ FWHM cycles (0.335 fs, right column). Angular distributions are obtained for three values of photoelectron energy $E = 1.45(2\omega_0 - |E_{1s}|) = 1.0$ a.u. (top row), $E = 2\omega_0 - |E_{1s}| = 0.687$ a.u. (middle row), and $E = 0.58(2\omega_0 - |E_{1s}|) = 0.4$ a.u. (bottom row), where E_{1s} is the energy of the $1s$ state in the SAE potential. (Figure from [235])

4.1.1.2 One- vs. two-photon ionization

In Figure 4.2 we present examples of PADs that show the transition from single photon ionization, illustrated by the p-wave character of the distribution (panels (d, g, h)), to an emission following two-photon absorption, highlighted by the dominating d-wave character in the PAD (panels (b, c, f)). The results are obtained for ionization by a laser pulse at a central photon energy $\omega_0 = 22$ eV, which corresponds to the energy difference between the $1s$- and $2p$-states in the single-active electron potential for helium used in the calculations, peak intensity $I_0 = 10^{11}$ W/cm^2

and carrier-to-envelope phase $\phi = 0$. At a given photoelectron energy, the transition occurs for a variation of the pulse duration, e.g. at $E = 2\omega_0 - |E_{1s}| = 0.687$ a.u. from 0.112 fs to 0.335 fs (middle row). Conversely, for a fixed pulse duration, the transition is seen for increase of the photoelectron energy, e.g. at $\tau = 0.224$ fs from 0.4 a.u. to 1.0 a.u. (middle column). In the transition regime the PADs exhibit the interference between the one- and two-photon ionization processes.

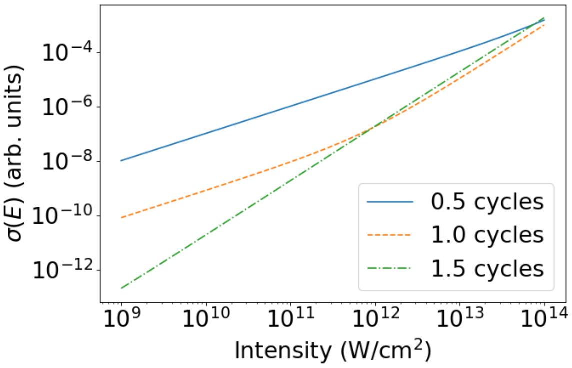

Figure 4.3: Cross section $\sigma(E)$ as a function of peak intensity for photoelectron emission at energy $E = 2\omega_0 - I_p = 18.7$ eV in 0.5-cycle (one-photon process dominates), 1.0-cycle (transition regime), and 1.5-cycle (two-photon process dominates). Central photon energy $\omega_0 = |E_{2p} - E_{1s}| = 22.2$ eV and carrier-to-envelope phase $\phi = 0$. (Figure from [235])

Further insights in the transition between the two processes can be found via the cross section $\sigma(E)$ and the first four anisotropy parameters β_i $(i = 1, \ldots, 4)$. In Figure 4.3 the results for the cross section are shown as function of peak intensity at fixed photon and photoelectron energies. The cross section for a 0.5 cycle pulse has a slope of one corresponding to the dominance of one photon ionization over the whole intensity regime. In contrast, the cross section obtained for the 1.5 cycle pulse is dominated by the two photon process due to the reduced bandwidth of the pulse. In the data for the 1-cycle pulse the transition from the one- to the two-photon process is seen to occur near 10^{12} W/cm^2.

In Figure 4.4 the results for the β-parameters are shown as function of pulse duration and peak intensity at fixed photon and photoelectron energies. The even β-parameters show the transition from dominant one-photon ionization ($\beta_2 > 0$, $\beta_4 \approx 0$) to dominant two-photon ionization ($\beta_2 \approx 0$,

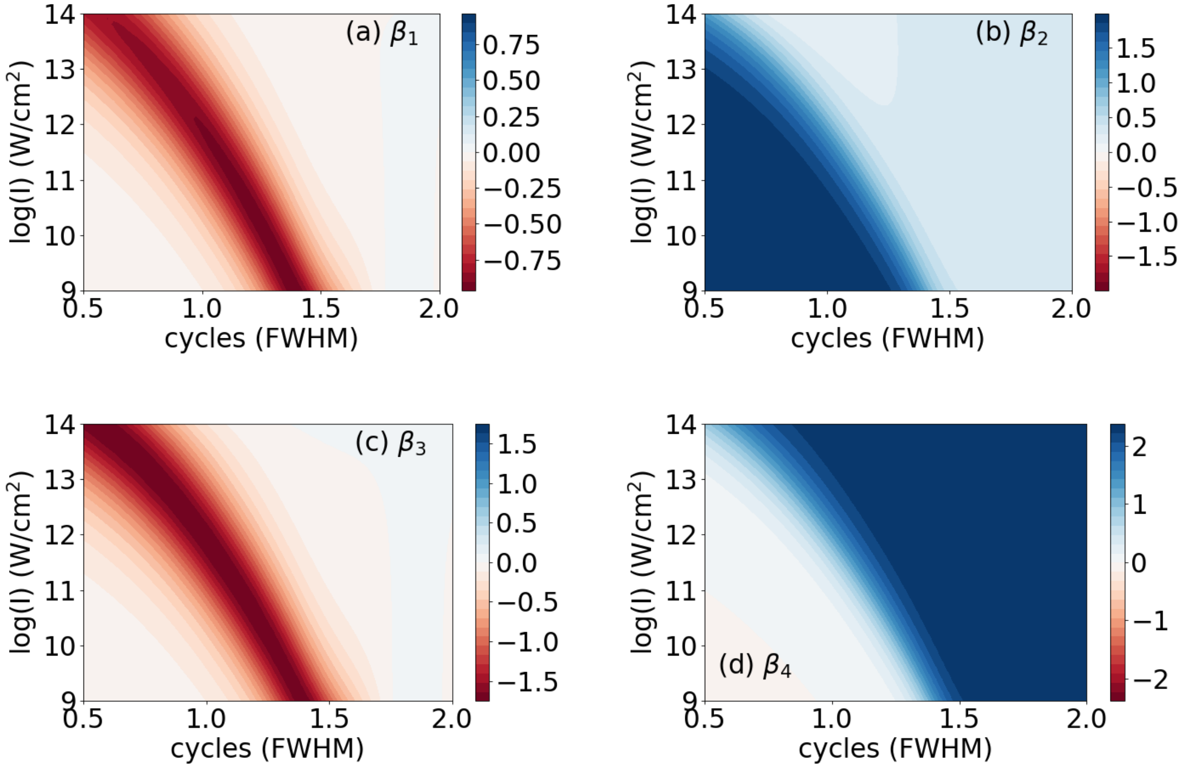

Figure 4.4: Parameters β_1 (a) to β_4 (d) as function of pulse duration (FWHM) and peak intensity. Central photon energy $\omega_0 = |E_{2p} - E_{1s}| = 22.2$ eV, carrier-to-envelope phase $\phi = 0$ and photoelectron energy $E = 2\omega_0 - I_p = 18.7$ eV. (Figure from [235])

$\beta_4 > 0$), while the odd β-parameters exhibit the regime of interference between the two processes ($\beta_1 < 0$ and $\beta_3 < 0$ for $\phi = 0$). The latter peak where the magnitudes of the two transition amplitudes coincide. At a given peak intensity the interference regime extends over a change of pulse duration of about 0.5 cycles at FWHM. For a fixed pulse duration, the interference regime extends over a variation of peak intensity by a factor of 2-5. We can therefore expect that the results are rather stable with respect to intensity fluctuations of the pulse. The impact of other potential pulse fluctuations in the experiment on the β-parameters will be discussed in subsection 4.1.1.3.

The transition probabilities of the one- and two-photon processes, σ_1 and σ_2, scale linearly and quadratically with intensity. Assuming that the two-photon ionization process involves predominantly the absorption of photons at equal energies, the peak intensity at maximum interference can be estimated as $I_{infer} \propto D^{(1)}(E)f(\Omega)/(D^{(2)}(E)f^2(\omega))$, where $D^{(i)}(E)$ is the square of the transition dipole moments for the one- and two-photon process, f is the spectral distribution of the pulse and $\Omega = 2\omega = E + |E_{1s}|$. Since $\omega = \omega_0$ for the results in Figure 4.4, $f(\omega) = f(\omega_0) = 1$ and $I_{infer} \propto f(\Omega)$. Thus, we expect that the interference between the two processes requires a larger spectral bandwidth, i.e. shorter pulse duration, the larger the peak intensity of the pulse. The results in Figure 4.4 confirm this expectation.

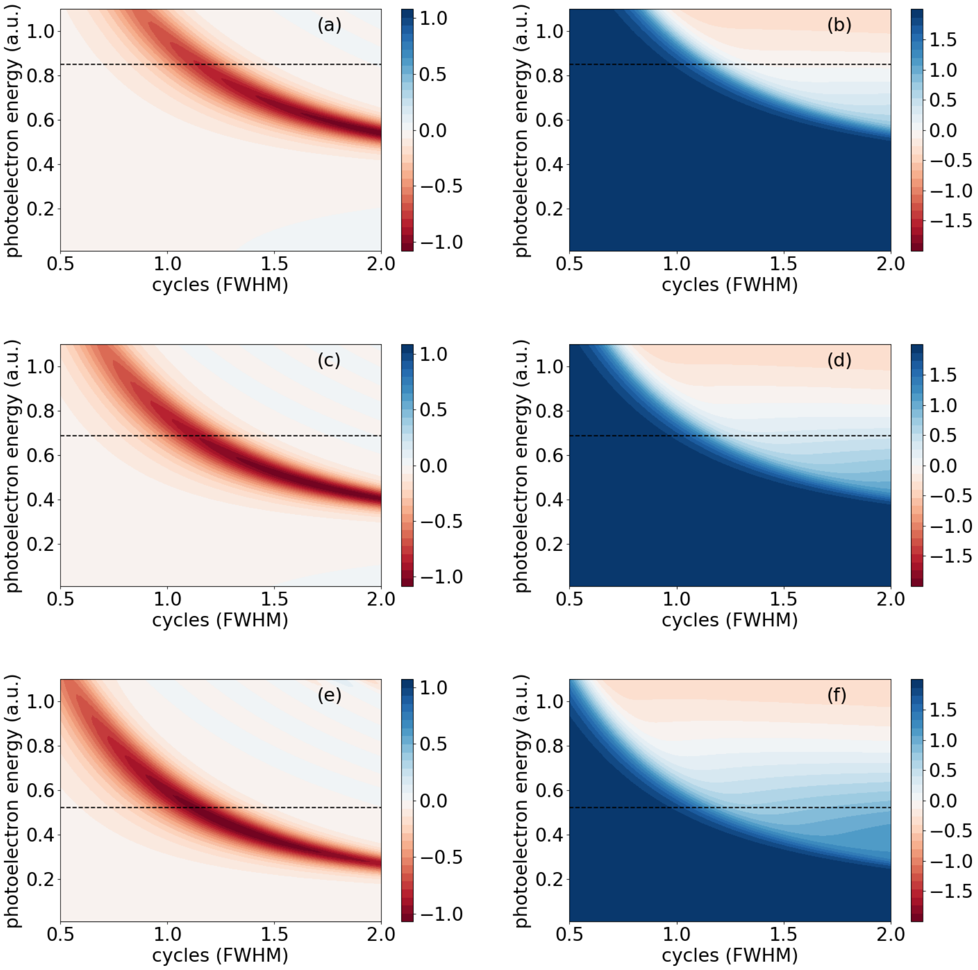

Figure 4.5: Anisotropy parameters β_1 (left) and β_2 (right) as function of pulse duration and photoelectron energy E for central frequencies $\omega_0 = 1.1|E_{1s} - E_{2p}|$ (top row), $\omega_0 = |E_{1s} - E_{2p}|$ (middle row) and $\omega_0 = 0.9|E_{1s} - E_{2p}|$ (bottom row) at peak intensity of 10^{11} W/cm^2 and $\phi = 0$. In each panel the dashed line corresponds to $E = 2\omega_0 - I_p$. (Figure from [235])

Next, we consider how the transition between the two pathways depends on the photoelectron energy and the central photon frequency at a given peak intensity $I_0 = 10^{11}$ W/cm^2 and carrier-to-envelope phase $\phi = 0$. To this end, we show in the Figure 4.5 the anisotropy parameters β_1 (left column) and β_2 (right column) as a function of photoelectron energy and pulse duration for central frequencies below (top row), on (middle row) and above (bottom row) resonance with the $1s - 2p$ transition in the helium single-active electron potential. We restrict ourselves to β_1 and β_2 since the higher order β-parameters contain equivalent information (see Figure 4.4). Also shown in Figure 4.5 is the photoelectron energy $E = 2\omega_0 - I_p$, corresponding to a two-photon transition at the central frequency ω_0.

The comparison shows that the transition regime depends on the central frequency, since the regime shifts for a given pulse duration to larger photoelectron energies as the central frequencies increases (from bottom to top). At a given central frequency, the pulse duration, at which the transition between the one- and two-photon ionization pathways occurs, increases as the photoelectron energy decreases. Qualitatively, this dependence can be understood using the relation $I_{infer} \propto D^{(1)}(E)f(\Omega)/(D^{(2)}(E)f^2(\omega))$. For photoelectron energies larger than $E = 2\omega_0 - I_p$ (dashed line), both ω and Ω are larger than the central frequency. Consequently, at large photoelectron energies a broader spectral distribution (shorter pulse duration) is required for the same value of $f(\Omega)/f^2(\omega)$ than at photoelectron energies below $E = 2\omega_0 - I_p$ (dashed line), where $\omega < \omega_0$ while $\Omega > \omega_0$.

Finally, we briefly mention that in the limit of short pulses and high intensities, both the one- and three-photon processes can interfere since the three-photon process scales with I^3. The results for the anisotropy parameter β_5 in Figure 4.6 confirm this expectation. At a photoelectron energy of $2\omega_0 - |E_{1s}|$ (panel (a)) a peak intensity of about 10^{14} W/cm^2 and a rather large spectral bandwidth is required to facilitate the three-photon process with significant probability since the corresponding photon energies are smaller than the central frequency. The distribution over photoelectron energy (panel (b)) shows that the impact of the three-photon ionization process is indeed more visible at energies near $E = 3\omega_0 - |E_{1s}|$.

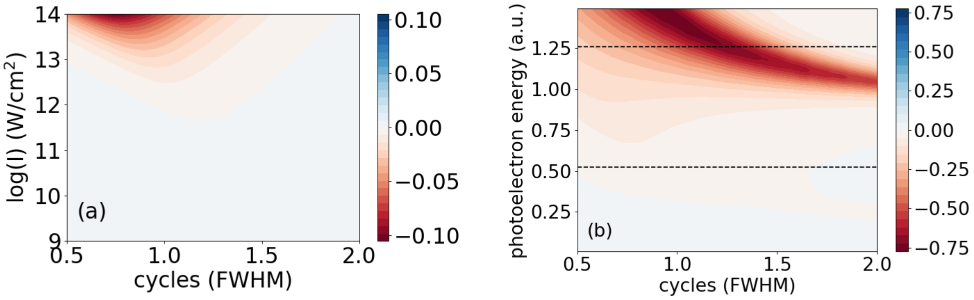

Figure 4.6: Anisoptropy parameter β_5 (a) as function of pulse duration and peak intensity at central frequency $\omega_0 = |E_{1s} - E_{2p}|$ and photoelectron energy $2\omega_0 - |E_{1s}|$ and (b) as function of pulse duration and photoelectron energy at central frequency $\omega_0 = 0.9|E_{1s} - E_{2p}|$ and peak intensity of 10^{13} W/cm^2. The dotted lines correspond to $E = 2\omega_0 - I_p$ and $E = 3\omega_0 - I_p$. The other parameters are as in Figures 4.4 and 4.5, respectively. (Figure from [235])

4.1.1.3 Impact of pulse fluctuations

For the discussion in the previous subsection we have considered results obtained at fixed pulse parameters. The results in Figures 4.4 and 4.5 show that the transition regime occurs over a rather small window of pulse duration while it appears to be rather stable for variations of the peak intensity up to half an order of magnitude. The photon energies in the extreme ultraviolet can be nowadays generated using high-order harmonics or free electron lasers. In view of the technical difficulties to control the carrier-to-envelope (CEP) of ultrashort pulses as well as the fluctuating pulse shapes in the self-amplified spontaneous emission (SASE) mode of free electron lasers, we have studied the impact of these variations on the anisotropy parameters.

To study the dependence on the CEP we have averaged the results about a given value ϕ_0 using a Gaussian distribution of width α as:

$$\beta_j^{(\alpha)}(\phi_0) = \frac{\sum_i \exp\left[-\frac{1}{2}\left(\frac{|\phi_i-\phi_0|}{2\pi\alpha}\right)\right]\sigma(\phi_i)\beta_j(\phi_i)}{\sum_i \exp\left[-\frac{1}{2}\left(\frac{|\phi_i-\phi_0|}{2\pi\alpha}\right)\right]\sigma(\phi_i)}\ , \tag{4.2}$$

where $\sigma(\phi_i)$ is the total ionization probability at CEP ϕ_i. The results for averages with (b) $\alpha = 0.2$ and (c) $\alpha = 0.4$ are compared in Figure 4.7 with the unaveraged results (panel (a)). As expected, the odd β-parameters, which reflect the interference between the one- and two-photon processes, strongly depend on CEP, while the even parameters are independent of it. Thus, the transition

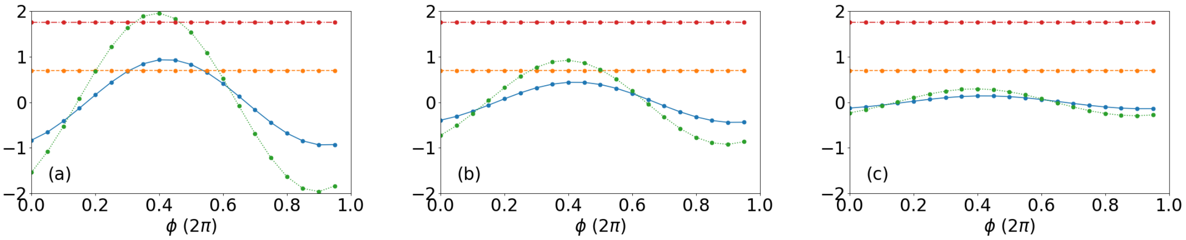

Figure 4.7: Anisotropy parameters β_1 (solid line), β_2 (dashed line), β_3 (dotted line) and β_4 (dashed-dotted line) as function of carrier-envelope-phase. The results averaged using a Gaussian distribution for the CEP (c.f., Eq. (4.2)) with widths of (b) $\alpha = 0.2$ (in units of 2π) and (c) $\alpha = 0.4$ are compared with the unaveraged results (a). Peak intensity: 10^{11} W/cm^2, central frequency: $\omega_0 = |E_{1s} - E_{2p}|$, pulse duration: 1.2 FWHM cycles and photoelectron energy $2\omega_0 - |E_{1s}|$. (Figure from [235])

from one-photon to two-photon ionization can be observed via β_2 and β_4 even in pulses without CEP stabilization. Although the odd parameters depend on CEP, the corresponding results appear to be indicative for the transition up to fluctuations of about $\pi/2$.

We have further studied the impact of fluctuations of temporal FEL laser pulse shapes [171]. We note that current FEL technology does not provide the bandwidth required to generate pulses down to the one- or two-cycle limit at the photon energies considered here. We may still attempt to give some theoretical insights concerning the robustness of the signal against the major fluctuations present in an FEL pulse. To this end, we have applied a partial coherence method, which has been used before to model longer FEL pulses [191]. We note that future technological progress towards generation of ultrashort FEL pulses in the EUV regime may necessitate to extent the current approach.

To generate the FEL pulses used in the numerical simulations, the spectrum of a vector potential with Gaussian envelope corresponding to peak intensity I_0 and FWHM pulse duration τ_0 is used as an input. Each spectral component is then multiplied with a random phase factor and an inverse Fourier transform is taken producing $A'(t)$, which is then normalized and windowed in time to give:

$$A_{FEL}(t) = A_0 f(t) \frac{Re\left[A'(t)\right]}{\max\left|Re\left[A'(t)\right]\right|} \tag{4.3}$$

where $A_0 = cE_0/\omega_A$ in Equation (3.41) and $f(t)$ represents the envelope, here a Gaussian envelope. The electric field of the FEL pulse is then obtained using Equation (3.42). The resulting pulse simulates the partially coherent nature of the SASE pulses produced by an FEL. The average of results from numerical simulations over an increasing number of shots is expected to resemble results similar to those produced during an FEL beam-time. Here, the β-parameters are calculated using a weighted average

$$\beta_j^{FEL}(E) = \frac{\sum_i^{N_{shots}} \sigma_i(E)\beta_{j,i}(E)}{\sum_i^{N_{shots}} \sigma_i(E)} \ , \tag{4.4}$$

to account for the photoelectron yield shot to shot.

In Figure 4.8 we compare the results for β_1^{FEL} (left) and β_2^{FEL} (right) as function of photoelectron energy and pulse duration of the Gaussian window used in modeling the FEL pulses, averaged over 10 (panels (c, d)) and 200 (panels (e, f)) FEL shots for each pulse length (i.e., 6,200 calculations in total) with the exemplary results from a single shot (panels (a,b)). A robust distribution for β_2^{FEL} emerges as the number of shots increases, clearly showing the transition from a one- to a two-photon process (the same conclusion holds for β_4^{FEL}, not shown). However, the interference in the photoelectron angular distributions cannot be determined via FEL laser pulses, since the results for β_1^{FEL} and β_3^{FEL} (not shown) average to zero in the transition regime. We note that the generated FEL pulses are not transform-limited and the pulse duration of the Gaussian window used in modeling the pulses does not correspond to that of Gaussian pulses used in the previous subsection 4.1.1.2. Comparing the data presented in Figure 4.8(f) with those in Figure 4.5(d) we estimate that the effective pulse duration of a bandwidth-limited Gaussian pulse with a spectrum corresponding to the average spectrum of the generated FEL pulses is about 0.6 times shorter than that of the Gaussian window.

4.1.2 Summary

In this Section we have provided theoretical results, obtained from numerical solutions of the time-dependent Schrödinger equation, for the competition between one-photon and two-photon ionization in an ultrashort extreme-ultraviolet laser pulse. We have shown that the transition

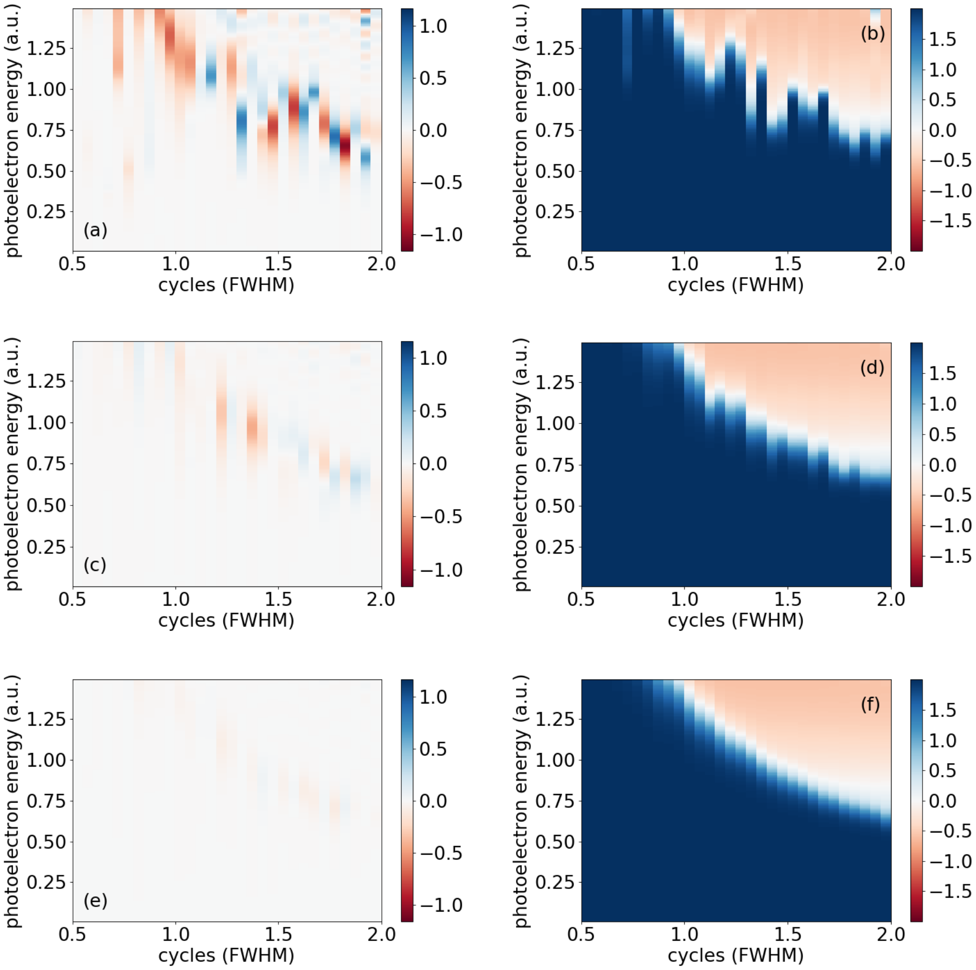

Figure 4.8: Anisotropy parameters β_1 (left) and β_2 (right) as function of pulse duration of the Gaussian window used in modeling the FEL pulses and photoelectron energy averaged over 10 (middle row) and 200 (bottom row) partially incoherent free electron pulses as compared to a single shot result (top row). Peak intensity of the Gaussian window: $I_0 = 10^{11}$ W/cm^2 and central frequency of the spectral distribution $\omega_0 = |E_{1s} - E_{2p}|$. (Figure from [235])

between the two processes can be observed in the photoelectron angular distributions and the related anisotropy parameters β_i $(i = 1, \ldots 4)$ as function of pulse duration, peak intensity, central photon frequency and photoelectron energy distribution. While the even β-parameters exhibit the transition via a change from zero to a finite value, the odd parameters indicate the interference regime. At given photon and photoelectron energies this regime extends over about 0.5 FWHM cycles in duration and a variation by a factor of 2-5 in peak intensity. The impact of three-photon ionization, which becomes available at these broadband pulses as well, is seen at high intensities and large photoelectron energies. Finally, we have considered typical variations in the CEP of ultrashort pulses, e.g. as produced in high harmonic generation, and fluctuating pulse shapes in free-electron laser pulses. It is found that the transition between one- and two-photon ionization can be observed via the even β-parameters in FEL pulses and pulses without CEP stabilization.

4.2 Generalized asymmetry parameters[2]

While studies of quantum systems in a single state are important, very interesting physics arises from the systems in superposition states. Nowadays the most prominent example of a two-level quantum mechanical system is a qubit with its important applications in quantum computation and quantum simulations [213]. Yet, also the internal motion of quantum mechanical systems, whether it is rotational, vibrational or electronic, is determined via superposition states. In ultrafast science the observation and resolution of such dynamics and, hence, the observation of atoms or molecules in superposition states has always played a central role. Currently, it is the superposition of atomic or molecular electronic states and the related attosecond electron dynamics that is the focus of studies in the field [80, 161, 105, 246]. Perhaps the simplest case of such dynamics is a helium atom in a superposition of $1s$ and $2p_1$ state which results in a wavepacket rotating in a plane around the nucleus with a period of ~ 200 attoseconds. The dynamics in such quantum systems in superposition states can be probed via ionization with an ultrashort laser pulse. Unlike for the ionization of a quantum system prepared in a single state, e.g. the ground state, conventional anisotropy and asymmetry parameters fail to provide comprehensive tools for the analysis of photoionization from atomic superposition states. As shown in the previous section, the simplest case of a competition between one- and two-photon ionization processes can be analyzed using asymmetry parameters if the atom is prepared in the ground state (see also, [112, 153, 82, 47, 104, 25, 243, 235]). In contrast, these analysis tools are either not applicable or do not provide a straightforward interpretation for the same processes if the atom is in the superposition of two states. Thus, an extension

---

[2] The content of this section has been also published in J. Venzke et al., Sci. Rep. **10**, 16164 (2020).

of the toolbox for the characterization of the states and the identification of competing pathways is desirable. In this section, we propose a new set of generalized asymmetry parameters which are sensitive to interference effects in the photoionization of atomic systems in superposition states. As we will show these new parameters can be used to identify the interplay of competing linear and nonlinear pathways at low and high intensities, as well as at ultrashort pulse durations. The application and relevance of the parameters is tested using state-of-the-art numerical solutions of the time-dependent Schrödinger equation. Our method provides a new approach to the analysis of experiments dedicated to resolving attosecond electron dynamics.

4.2.1 Generalized asymmetry parameters

We consider a prototypical example in ultrafast science and, more general, in atomic physics, which is schematically shown in Fig. 4.9. An atom in a superposition of two quantum states with different magnetic quantum numbers m, say the ground (g) and an excited (e) state is probed via ionization by an ultrashort linearly polarized laser pulse. The photoelectron emission is induced by a pulse with central frequency ω tuned to the energy gap of the two states. The broad energy spectrum of an ultrashort Gaussian pulse is schematically depicted in the panels of Fig. 4.9 centered about the energy of the excited state. There are three competing pathways leading to photoelectron emission with energy $2\omega - |E_g|$, where E_g is the ground state energy of the atom: (a) absorption of one photon at ω from the excited state, (b) absorption of two photons with sum frequency 2ω from the ground state and (c) absorption of one photon at 2ω from the ground state. While the ionization from the excited state (a) is the dominant pathway at low peak intensities and long pulse duration, the transitions from the ground state will interfere at higher peak intensities (two-photon process, (b)) and if the bandwidth of the pulse is broad enough (i.e., the pulse duration is sufficiently short, (c)). The exemplary results obtained from the solutions of the time-dependent Schrödinger equation in Fig. 4.9 for the interaction of neon atom, prepared in the superposition of $2p_{-1}$- and $3d_2$-states (d) or prepared in the same superposition but including additionally ionization from the $2p_0$ and $2p_1$ ground states (e), with a linearly polarized laser pulse show that the photoelectron

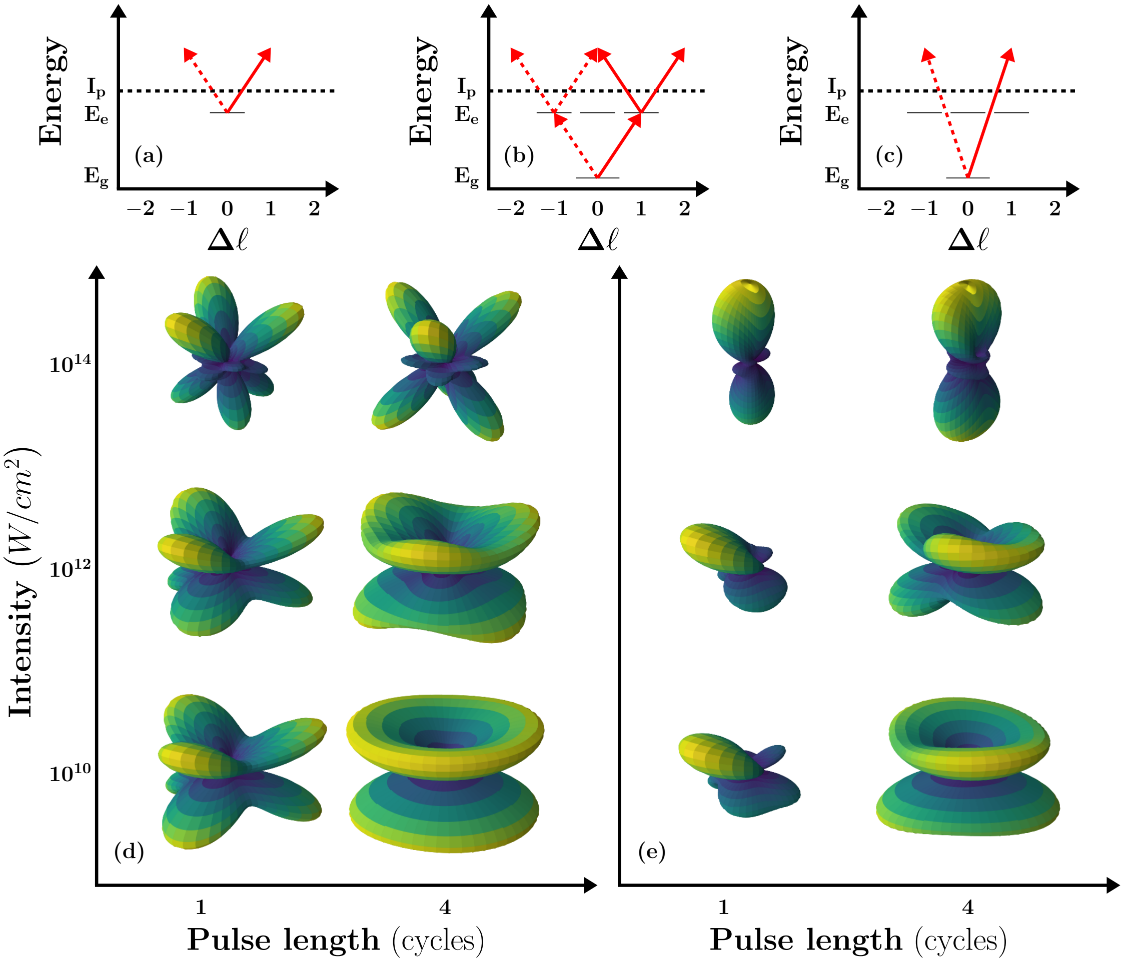

Figure 4.9: (a-c): Ionization pathways effective in different intensity and pulse length regimes. (d) Photoelectron angular distributions for ionization of neon atom, prepared in $2p_{-1} - 3d_2$ superposition, as function of intensity and pulse length. (e) The same as (d) including additionally ionization from the $2p_0$ and $2p_1$ states. (Figure from [232])

angular distributions (PADs) vary significantly as function of pulse duration and peak intensity. The forward-backward asymmetry, often used in the past, cannot be applied to identify the impact of the different pathways in these PADs. Therefore, a new set of asymmetry parameters is needed for photoionization from superposition states with ultrashort laser pulses.

4.2.1.1 Definition

We start by expanding the PAD as a coherent sum of spherical harmonics, assuming the atom is ionized by a linearly polarized pulse aligned along the z-axis as

$$P(\theta,\phi) = \left|\sum_{\ell} C_{\ell}^{m_g} Y_{\ell}^{m_g}(\theta,\phi) + C_{\ell}^{m_e} Y_{\ell}^{m_e}(\theta,\phi)\right|^2 \tag{4.5}$$

where m_g (m_e) are the magnetic quantum numbers of the ground (excited) state in the superposition, C_{ℓ}^{m} is the complex amplitude and $Y_{\ell}^{m}(\theta,\phi)$ is the spherical harmonic. The asymmetry in the PADs due to the interference between different channels is related to the relative phase and amplitude of the spherical harmonics. For each spherical harmonic, the sign of the phase is symmetric (asymmetric) across the xy-plane when $\ell+m$ is even (odd), while in the xy-plane the phase is proportional to $e^{im\phi}$.

In the xy-plane there are regions of destructive and constructive interference between the transition amplitudes from the ground and excited state, as illustrated on the left of Fig. 4.10. The regions can be labeled by

$$c_i = \left\lfloor \frac{(\phi-\phi_0)\Delta m}{\pi} \right\rfloor \tag{4.6}$$

where $\lfloor\rfloor$ is the floor function, ϕ_0 is a reference angle, and $\Delta m = |m_g - m_e|$ ($\Delta m = 3$ in Fig. 4.10). Setting ϕ_0 at an angle where the interference switches from constructive to destructive, regions of destructive interference signal are labeled by even c_i while odd c_i denote regions of constructive interference. Next we define the following integrals:

$$I_{\pm}^{even} = \sum_{even\ c_i} \int P(\theta,\phi)\, d\Omega_{c_i}^{\pm} \tag{4.7}$$

$$I_{\pm}^{odd} = \sum_{odd\ c_i} \int P(\theta,\phi)\, d\Omega_{c_i}^{\pm} \tag{4.8}$$

where $d\Omega_{c_i}$ is the solid angle for the region c_i in the positive ($z>0$) or negative ($z<0$) hemisphere with respect to the xy-plane. In the example in Fig. 4.10 (left) each integral represents the total photoelectron signal in the regions of a specific color (dark blue, light blue, dark red, light red). We now define general asymmetry parameters (GAPs) that account for the relative difference in the regions of constructive and destructive interference:

$$A_p^{\Delta m} \equiv \begin{cases} \left| \frac{(I_+^{even}+I_-^{even})-(I_+^{odd}+I_-^{odd})}{I_+^{even}+I_-^{even}+I_+^{odd}+I_-^{odd}} \right|_{max(\phi_0)} & \text{even } \gamma \\ \\ \left| \frac{(I_+^{even}+I_-^{odd})-(I_+^{odd}+I_-^{even})}{I_+^{even}+I_-^{even}+I_+^{odd}+I_-^{odd}} \right|_{max(\phi_0)} & \text{odd } \gamma \end{cases} \tag{4.9}$$

where $\gamma = \ell_e + m_e + \ell_g + m_g + N_p$ with ℓ_g (ℓ_e) are the quantum numbers of the ground (excited) state in the superposition, and $p = (\gamma \bmod 2)$ is the parity of γ. Each parameter $A_p^{\Delta m}$ is related to a certain total number of absorbed photons, $N_p = N_g + N_e$, where N_g (N_e) is the number of photons absorbed in the transition from the ground (excited) state. We note that GAPs cannot only be defined for ionization of superposition states with a linearly polarized laser pulse along the z-axis, but the definition can be extended, for example, to ionization with a circularly polarized ionizing laser pulse in the xy-plane. In that case $\gamma = \ell_e + m_e + \ell_g + m_g$, the number of photons is not included as both ℓ and m change by 1 for each photon absorbed. Using $\Delta m = |(m_g \pm N_{pg}) - (m_e \pm N_{pe})|$ for right (+) and left (-) handed circular polarized probe pulses, processes with different number of photons involved can be studied by analyzing the signals with different Δm. Here, in the further discussion and applications we, however, focus on the case of a linearly polarized probe pulse.

To exemplify the significance of the asymmetry parameters we consider the ionization of Ne atom, initially prepared in the $2p_{-1} - 3d_2$ superposition (i.e., $\ell_g = 1$, $m_g = -1$, $\ell_e = 2$, $m_e = 2$; and, hence, $l_g + m_g + l_e + m_e = 4$), by an ultrashort intense laser pulse. As discussed at the outset, we expect interferences between two kind of pathways depending on the peak intensity and the pulse duration. For an ultrashort pulse at low intensities one-photon transitions from the ground (Fig. 4.9(c), $N_g = 1$) and the excited states (Fig. 4.9(a), $N_e = 1$) will interfere, with $N_p = N_g + N_e = 2$, $\gamma = 6$ and $p = 0$. An examplary PAD, obtained via numerical TDSE solution in the relevant intensity and pulse duration regimes, is shown at the top of the right column in Fig. 4.10. For even γ the corresponding parameter A_0^3 relates to the difference between the total photoelectron signals in the dark red and light blue shaded regions, as depicted at the top of the middle column of Fig. 4.10. Comparison with the PAD shows that this difference indeed accounts

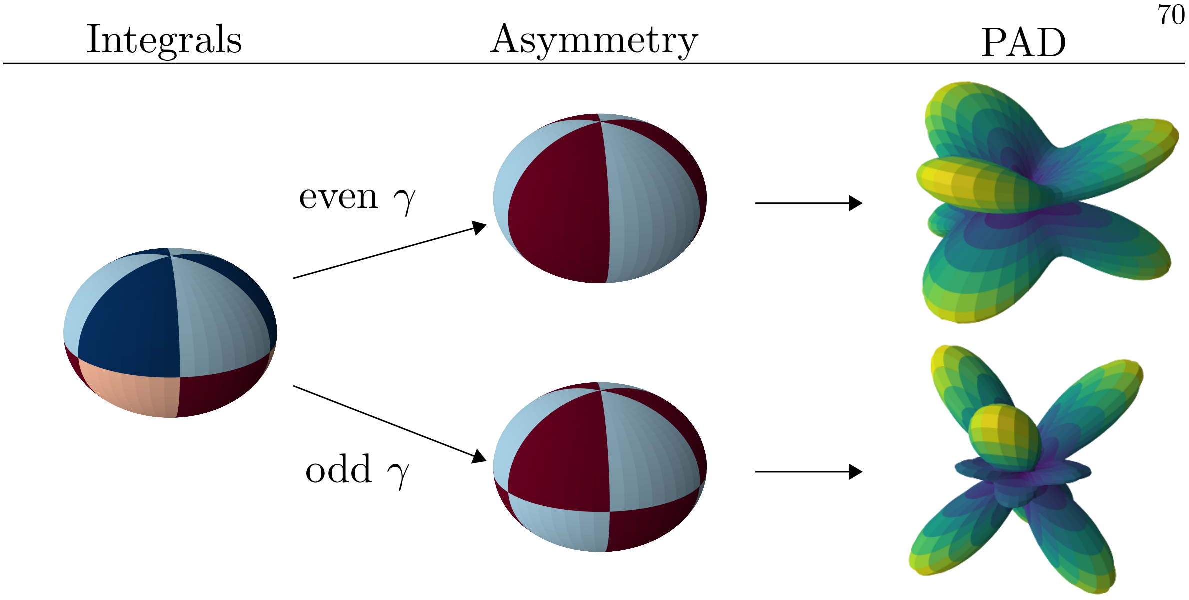

Figure 4.10: Conceptual illustration of GAPs (for $\Delta m = 3$). Left: Integrals $I_{\pm}^{even/odd}$, Eqs. (3,4), are defined over regions of constructive and destructive inferference, indicated by different colors (dark blue, light blue, dark red, light red), in xy-plane. Middle: GAPs are constructed based on the parity of the parameter $\gamma = l_e + m_e + l_g + m_g + N_p$ from the integrals over the regions denoted by a certain color (light blue, dark red). Right: Examplary PADs displaying the asymmetry captured by the parameters for even and odd γ. (Figure from [232])

for the asymmetry in the PAD induced by the interference of the transition amplitudes for the one-photon processes from the ground and the excited states. In contrast, due to the dependence of multiphoton transition amplitudes on the intensity of the pulse at longer pulse duration and higher intensities it is expected that the one-photon transition from the excited state (Fig. 4.9(a), $N_e = 1$) interferes with the two-photon absorption from the ground state (Fig. 4.9(b), $N_g = 2$), giving rise to $N_p = 3$, $\gamma = 7$ and $p = 1$ for ionization of Ne($2p_{-1} - 3d_2$). The regions relevant in the calculation of the asymmetry parameter A_1^3 and the corresponding exemplary PAD for the Ne atom are presented in the bottom row of Fig. 4.10. The comparison indicates the significance of the asymmetry parameter A_1^3 for the detection of the interference at high intensities.

4.2.1.2 Application via numerical simulations

For the application of the GAPs we have considered certain superpositions of two atomic states which are first prepared by a pump pulse and then probed by a linearly polarized pulse at a set time delay such that the relative phase between the two states is determined. In the calculations we have therefore simulated the interaction with the probe pulse only by using numerical solutions of the time-dependent Schrödinger equation (TDSE) for the interaction of a electron in a single-active electron (SAE) potential with the electric field **E** of a linearly polarized laser pulse (aligned along the quantization $\hat{z}$-axis) in dipole approximation and length gauge with a frequency corrected laser as described in Chapter 3. The present calculations are performed utilizing single active electron potentials for He atom and Ne atom [204] with the electron initially prepared in a superposition of the ground and an excited state. The TDSE has been solved by expanding the wavefunction in spherical harmonics (up to $\ell_{max} = 50$ for all relevant m values), as described in Sec. 4.1. The computations have been performed on a radial grid of 300 a.u. with a grid spacing of 0.05 a.u. using exterior complex scaling on the outer 15 a.u. of the grid. A time step of 0.05 a.u. has been used.

4.2.2 Results and discussion

For our applications we have considered individual superposition states in neon (Fig. 4.11) and realistic superposition states considering all possible initial m_g states of neon and helium atoms (Fig. 4.12). The central frequency of the applied electric field was set to the energy difference of the initially populated field-free states ($\omega_0 = |E_g - E_e|$). To analyze the relevance of both the short-pulse parameter $A_0^{\Delta m}$ and the high-intensity parameter $A_1^{\Delta m}$ calculations have been performed for one- and four-cycle probe pulses (FWHM pulse durations) as function of the peak intensity of the pulse. At the end of each simulation of the time-dependent Schrödinger equation we obtained the photoelectron angular distribution at a given momentum k (corresponding to a photoelectron energy of $E = 2\omega - |E_g|$) by projecting the wavefunction onto the field-free continuum states on the numerical grid. The asymmetry parameters $A_0^{\Delta m}$ and $A_1^{\Delta m}$ are then determined from the numerical PADs using Eq. (4.9).

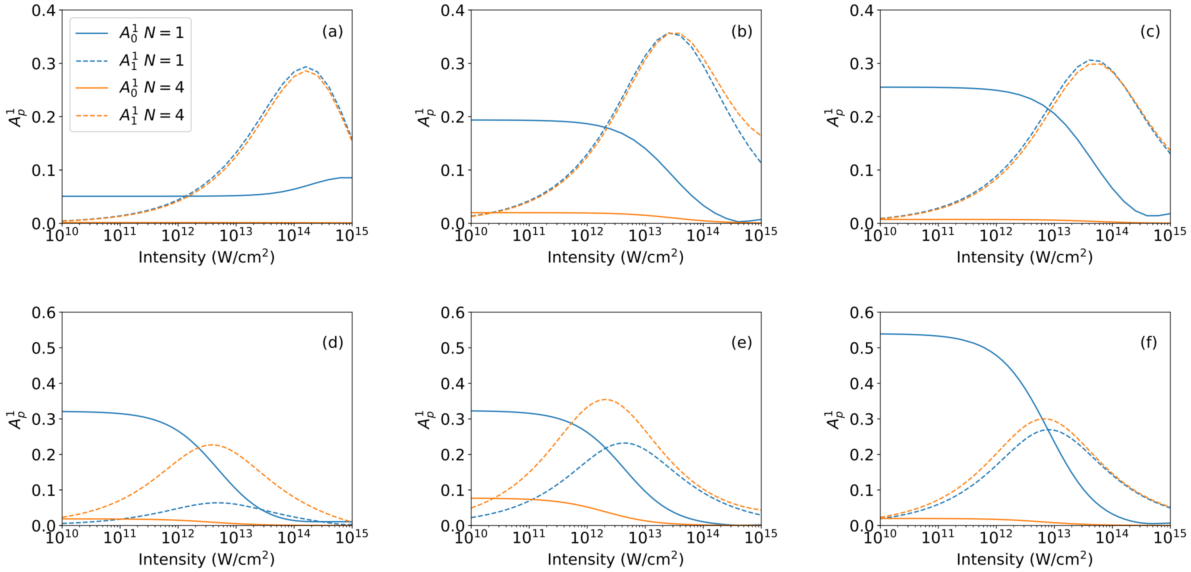

Figure 4.11: Generalized asymmetry parameters A_0^1 (solid lines) and A_1^1 (dashed lines) as function of intensity for ionization of superpositions of $2p_{-1} - 3d_0$ (a), $2p_0 - 3d_1$ (b), and $2p_1 - 3d_2$ (c) in neon atom with initial populatations of 0.5 for each state (top row). Results in bottom row for superpositions with populations of $P_{2p_{-1}} = 0.98, P_{3d_0} = 0.02, P_{4s_0} = 0.00057$ (d), $P_{2p_0} = 0.94, P_{3d_1} = 0.06$ (e), and $P_{2p_1} = 0.88, P_{3d_2} = 0.12$ (f). Results have been obtained for one-cycle (blue lines) and four-cycle (orange lines) pulses at photoelectron energy $E = 2\omega - I_p$. (Figure from [232])

To exemplify the application and provide basic insights in the relevance of the GAPs, we have first considered superpositions of individual sublevels in different shells of the neon atom as initial state. Fig. 4.11 shows results for the GAPs as a function of peak intensity for interaction of a neon atom, prepared in $(2p_{-1} - 3d_0)$ (a,d), $(2p_0 - 3d_1)$ (b,e), and $(2p_1 - 3d_2)$ (c,f) superpositions. For the results in the top row equal population in the two initial states has been considered, while for those in the bottom row populations, as produced via one-photon excitation by a 50 cycle, 10^{13} W/cm^2 right handed circulary polarized pump pulse, are used for the initial state (states with populations larger than 10^{-5} are considered, see figure caption for values). The central frequency of the ionizing probe laser pulse is tuned to the energy gap between the field-free ground and excited states.

Overall, except for the results in panel (a) which we will discuss below separately, the short-pulse parameter A_0^1 (solid lines) is large at low intensities and for the shorter of the two pulse durations. This is expected from our discussion above and confirms that the parameter is an indicator for the interference of the one-photon signal from the ground state and the one-photon signal from the excited state. Since both of these signals are first order in intensity, their relative strengths and, hence, the A_0^1 parameter are independent of intensity at low intensities for a given initial superposition state. As the intensity increases, the relative amplitude of the two-photon ionization channel increases and finally dominates over the one-photon channel from the ground state. This trend is reflected in both the short-pulse and the high-intensity parameters. The increase in A_1^1, resulting from the interference between the one-photon excited state signal and the two-photon ground state signal, shows in which intensity regime the two-photon signal starts to overtake the short pulse signal. Simultaneously with the increase of A_1^1 we observe a decrease of the A_0^1 signal, in agreement with our physical interpretation of the relevance of the different pathways. Parenthetically, we note the onset of an increase of the A_0^1 parameter at high peak intensities is likely due to pathways involving higher order processes with an even number of total photons.

While the general trends of the two parameters are similar in most of the cases, there is one exception where the details differ significantly. In the case of the $(2p_{-1} - 3d_0)/\sqrt{2}$ superposition (panel a), A_0^1 shows a different trend. It remains constant at low intensities before increasing at higher intensities. As the laser pulse and relative populations are fixed in the top row (a-c) of Fig. 4.11, the change in amplitude and shape of A_0^1 and A_1^1 are caused by changes in the cross-sections of the various states. We, therefore, attribute the different trend in the A_0^1 signal in panel (a) to be due to the dominance of the one-photon transition from the $3d_0$ state at all intensities, since $m = 0$ states are, in general, easier to ionize with a linearly polarized pulse than those with $|m| > 0$. This interpretation is further supported by the results in Fig. 4.11(d) for a superposition with much lower initial population in the $3d_0$-state. Despite the difference in magnitude of transition amplitudes, now the interference between the one-photon pathways is effective and the general expected trend for the short-pulse parameter A_0^1 is present.

Comparison of the results in the two rows of Fig. 4.11 shows that the intensity at which the transitions in the parameters occur depends on the population in the two states in the initial superposition. Since in the bottom row the populations in the excited states are low, the relative magnitudes of the corresponding one-photon transition amplitudes from the excited states as compared to those from the ground state levels are weaker than for the equally populated superpositions (top row). Therefore, we observe the impact of the two-photon pathway from the ground state at lower intensities in the results in the bottom row. Additionally, the A_1^1 signal becomes sensitive to changes in pulse length due to the weak signal from the excited state. Thus, the GAPs may also be useful to detect the population ratio in the superposition states. Here, we do not further analyze this feature, but focus on the more general application of the parameters to identify the presence of different ionization pathways.

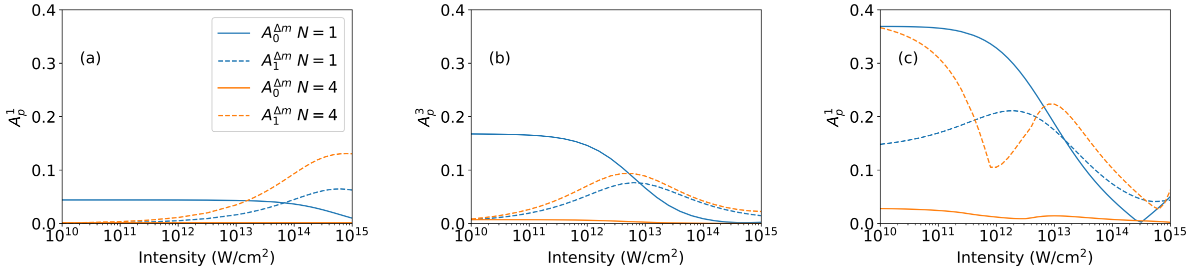

Figure 4.12: Same as Fig. 4.11 but for superpositions generated by a right-handed circularly polarized pulse via one-photon transition in helium atom (a), three-photon transition in neon atom (b), and one-photon transition in neon atom (c) (for details see text). (Figure from [232])

So far, in Fig. 4.11 we considered simple albeit somehow artificial superposition states restricted to certain sublevels of two shells in the neon atom. Now, we extend our analysis to three different initial states as they can be generated with right-handed circularly polarized pump laser pulses: (a) one-photon excitation of helium atom to the $2p_1$ state leading to $(1s-2p_1)/\sqrt{2}$ superposition, (b) three-photon excitation of neon atom to the $3d$ shell, leading to an initial state consisting of a superposition with equal population in $2p_{-1}$ and $3d_2$ along with populated $2p_0$, and $2p_1$ states (note, that the latter two $2p$ states cannot be excited by the absorption of three right-handed circularly polarized photons to the $3d$ shell), and (c) one-photon excitation of neon atom to the $3d$ shell leading to the combination of the three superposition states analyzed separately in the bottom row of Fig. 4.11. In Fig. 4.12, we present results for the GAPs of the corresponding calculations. The initial superpositions in case of the helium data (a) and the neon data in panel (b) consist of just one state in the excited shell and show the same general trends as those in the majority of the panels of Fig. 4.11 with the decrease of $A_0^{\Delta m}$ along with the increase of $A_1^{\Delta m}$ occurring in a certain intensity regime. The transitions in helium occur at a higher peak intensity due to the more tightly bound helium ground state, which is harder to ionize. The overall trends of the results in Fig. 4.12(c) for the more complex initial superposition, consisting of six states in the $2p$- and the $3d$-shell of neon. The one-cycle pulse data are similar to those discussed before, providing the same information about the impact of the two-photon transition from the ground state. However, the A_1^1 parameter, particularly at the longer pulse duration, shows an additional interference structure in the transition regime. It is likely that this is due to an interference between transitions originating from two excited states differing by $\Delta m = 1$, here between one-photon ionization signals from $3d_0$ and $3d_1$ as well as from $3d_1$ and $3d_2$. Although the number of absorbed photons in these transition is not 3, the resulting γ has the same parity as the signal from a $2p_m - 3d_{m+1}$ state.

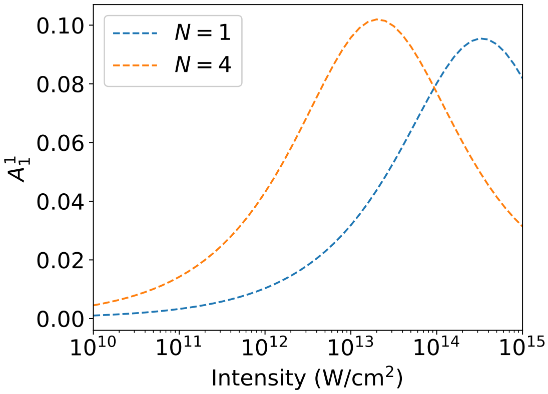

Figure 4.13: Asymmetry parameter A_1^1 for ionization of helium atom ($1s$-$2p_1$) with one- and four-cycle pulses at central frequency $\omega = 1.2\omega_0$. (Figure from [232])

The high-intensity asymmetry parameter $A_1^{\Delta m}$ is not only indicative of the general features concerning the interferences between the pathways discussed above, but also provides insights in more subtle aspects. In the top row of Fig. 4.11 the maximum of the asymmetry parameter $A_1^{\Delta m}$ occurs at the same intensity independent of the pulse duration. This is due to the fact that in the calculations the central frequency was set to the energy difference of the initially populated states. In this case the center of the photoelectron energy distributions due to the one-photon ionization from the excited state and the two-photon transition from the ground state nearly coincide. If the frequency is detuned from the resonance, the position of maximum interference strongly depends on the pulse duration. Due to the larger spectral width of the pulse at shorter pulse duration, the interference between the channels becomes most effective at higher intensities than the longer pulse duration results, at which the photoelectron distributions from the two channels have less overlap. This effect is seen in the results in Fig. 4.13 for photoionization at a central frequency of 1.2 times the energy difference between the $1s$- and $2p_1$-states in helium atom.

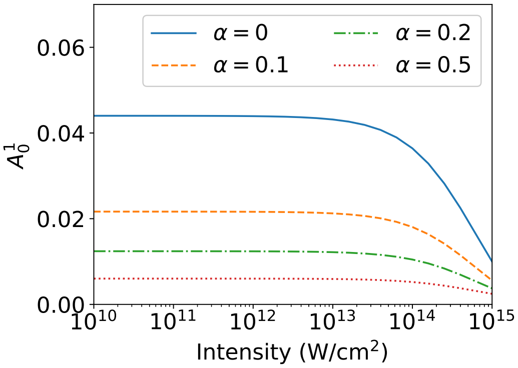

Figure 4.14: Asymmetry parameter A_0^1 for ionization of helium atom ($1s$-$2p_1$) with one-cycle pulses at central frequency ω_0. Results of averages over different Gaussian distributions of CEP with width α are compared with those at fixed CEP ($\alpha = 0$, solid line). (Figure from [232])

Finally, it is important to consider variations in the laser parameters relevant for an application of the generalized asymmetry parameters in an experiment. Typically, the peak intensity of the applied laser pulse may vary from shot to shot as well as over the interaction volume. The results in Fig. 4.11 and Fig. 4.12 show that the two GAPs vary rather slowly as a function of peak intensity. Thus, we can expect that variations in intensity in an experiment will not impact the results significantly. Another parameter that is usually difficult to control is the CEP of a laser pulse, which typically becomes most important for ultrashort pulses. In the present study the high-intensity A_1^1 parameter is independent of variations in CEP. To study the dependence on the CEP for the short-pulse low-intensity asymmetry parameter A_0^1 we have obtained results as a function of the CEP and averaged the results about a given value φ_0 using a Gaussian distribution of width α (in units of 2π) as:

$$A_p^{\Delta m}(I,T;\alpha) = \frac{\sum_i \exp\left[-\frac{1}{2}\left(\frac{|\varphi_i-\varphi_0|}{2\pi\alpha}\right)\right]\sigma(\varphi_i)A_p^{\Delta m}(\varphi_i,I,T)}{\sum_i \exp\left[-\frac{1}{2}\left(\frac{|\varphi_i-\varphi_0|}{2\pi\alpha}\right)\right]\sigma(\varphi_i)}\ , \tag{4.10}$$

where $\sigma(\varphi_i)$ is the total ionization probability at CEP φ_i. In the calculations we have assumed that the pump pulse (for the preparation of the initial state) has the same CEP as the probe pulse. The comparison of the results for different averages in Fig. 4.14 with the results for fixed CEP (solid line) shows that for He atom the short-pulse asymmetry parameter A_0^1 is indicative for the interference up to fluctuations of about $\pi/2$ in the CEP.

4.2.3 Summary

In summary, in this section we have introduced a set of generalized asymmetry parameters (GAPs) which characterize the interference of linear and nonlinear pathways to ionization of atoms, prepared in superposition states, due to the interaction with a linearly polarized intense ultrashort laser pulse. These parameters may provide a new tool to analyze data in attosecond experiments. The relevance of the parameters is demonstrated via the results of numerical simulations of ionization of helium and neon atom. The impact of short pulse and nonlinear effects, as they arise in experiments with free-electron lasers and high-order harmonic generation, is shown. The dependence on the central frequency of the applied laser pulse and the impact of variations of laser parameters, such as the peak intensity and the carrier-to-envelope phase, are analyzed and discussed.

4.3 Wavefunction reconstruction method[3]

As mentioned above, one of the simplest cases of a superposition of atomic states with different orbital angular momentum and magnetic quantum numbers is that of a helium atom in the $1s$ and $2p_1$ states. It results in an ultrafast electron dynamics given by a wave packet rotating in a plane around the nucleus with a period of $\sim$ 200 attoseconds. We now use this dynamics as a prototype example to study the reconstruction of the corresponding wave packet via ionization with an ultrashort linearly polarized probe laser pulse. To this end, we analyze the photoelectron angular distributions as a function of time delay from the instant of preparation of the atomic superposition states. The concept is based on the idea to utilize quantum beating signals, where the imaged wave packet is interfered with a reference wave, to reconstruct a wave function [185, 173, 161, 130, 198, 116]. Accounting for the phase accumulation, ionization cross sections, and characterization of the reference wave packet that is used in the measurement is a non-trivial task. In this section we present a method for wave packet reconstruction based on quantum beating signals that utilizes perturbation theory. Since the method requires knowledge of the average values for intensity, carrier-to-envelope phase and pulse duration of the probe pulse we perform a sensitivity study to show the impacts of noise produced in an experiment and the limits in peak laser intensity on the reconstruction method. Finally, we consider the extension of the method to imaging of wave packets consisting of superpositions of more than two states.

The rest of the section is organized as follows: In section 4.3.1 we first present and discuss the ionization scheme on which the reconstruction method is based. Then we briefly review the methods for the numerical methods used for the reconstruction algorithm. In section 4.3.2 we present the application of the method to the reconstruction of a circular wave packet in helium atom. Aspects of the error analysis with respect to the accuracy of the observation of the PADs and the variation of the laser parameters will be presented. Furthermore, the impact of different pathways on the reconstruction process will be studied. Finally, we briefly discuss the extension of

---

[3] The content of this section has been also published in J. Venzke et al., PRA. **103**, 042808 (2021).

the method to superpositions of more than two states along with results for a specific three-state superposition. The section ends with a summary.

4.3.1 Concept and theoretical methods

4.3.1.1 Pump-probe scheme

In this study, we focus on the reconstruction of a wave function and the related imaging of the dynamics via photoelectron angular distributions (PAD). To this end, we start our simulations in a superposition state of the atom. An experiment will require a pump pulse to generate the superposition. There are a few requirements for the pump pulse itself to apply the reconstruction scheme. Since the scheme relies on the measurement of the PADs at various time delays between the pump and the probe pulse, the pump must be a reproducible pulse with a fixed carrier envelope phase (CEP) such that the superposition generated for each measurement is very similar from shot to shot if not the same. However, the form of the electric field of the pump pulse does not need to be known. Next, the delay between the pump and probe pulses must be controlled on the attosecond time scale to allow for measurements as a function of the delay. The shot-to-shot measurements should be taken for time delays within one cycle of the probe pulse giving rise to the requirement of an attosecond control over the delay. The total delay is irrelevant as long as the two pulses do not overlap in time and the state to be imaged does not decay. Furthermore, photoelectrons generated by the pump pulse have to be separated from those produced by the probe pulse. It might be therefore useful to limit ionization by the pump pulse.

The method studied here can be applied to simple superpositions, consisting of population in two or three atomic states. As prototypical example we consider a helium atom in a $1s - 2p_1$ superposition, which represents a circular wave packet rotating around the nucleus. This superposition with equal population in the two levels can be created with a ~ 23 cycle laser pulse at 10^{14} W/cm^2 tuned to the resonance frequency. Fig. 4.15(a) shows the dynamics via isosurfaces of the wave function (i.e., $|r\Psi|^2$) rotating in the $x - y$ plane on an attosecond time scale.

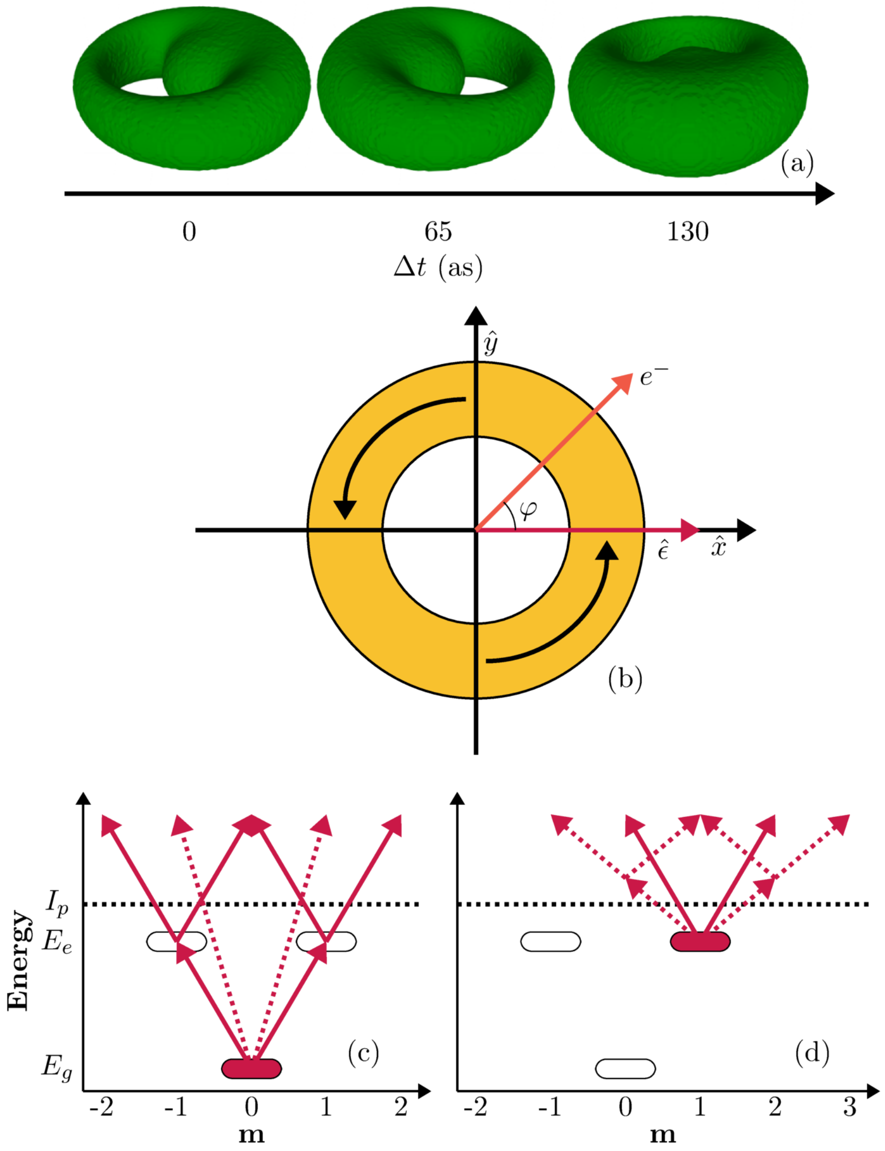

Figure 4.15: (a) Isosurfaces of the $1s - 2p_1$ wave function ($|r\Psi|^2$ is shown) evolving in time. (b) Ionization scheme in the $x - y$ plane. The laser polarization along the x-axis is depicted in red, the direction of the ionized electron is shown in orange, and the charge migration is shown in yellow. Selection rules for ground state signal (c) and excited state signal (d). The solid lines illustrate the transitions of photons absorbed at the central frequency and the dashed lines show the pathways for short pulse effect due to the large bandwidth of an ultrashort pulse. (Figure from [233])

To characterize the motion, and in turn reconstruct the wave function, we expand the initial wave function in the eigenbasis of stationary states and write the wave function at some time t as:

$$\Psi(\boldsymbol{r}, t) = a_0 \psi_0(\boldsymbol{r}, t) + \sum_{j=1}^{N-1} a_j e^{i\theta_j} \psi_j(\boldsymbol{r}, t) \tag{4.11}$$

where a_j is a positive real number, θ_j is a relative phase, and $\{\psi_j = \Psi_{nlm}; j = 0, \ldots, N-1\}$ is the eigenstate basis. While the basis may contain an infinite number of eigenstates, for practical means in the numerical calculations and any application it has to be truncated at some finite number N. Thus, the wave function depends on $N-1$ phases and N amplitudes since the global phase is not a physically relevant quantity. In this framework, the time dependence is contained in the states $|\psi_j(t)\rangle$ and the initial wave function is completely reconstructed if all a_j and θ_j for $j \geq 1$ are obtained since a_0 is fixed by the normalization and we set the phase of ground state $|\psi_0\rangle$ to zero. If the wave function generated by the pump pulse can be reconstructed at a given time, the full time dependent motion of the wave function has also been obtained.

In the reconstruction scheme that we consider the electron dynamics is probed via ionization by an intense ultrashort laser pulse as a function of time delay after the end of the pump pulse. In the scheme predictions of first- and second-order perturbation theory (PT) are used to determine the unknown phases and amplitudes from the photoelectron angular distributions (PADs). The latter may be determined in an experiment but in this theoretical study we utilize ab-initio numerical calculations. For the case of a helium atom in a $1s-2p_1$ superposition, we apply a probe laser pulse linearly polarized along the x-axis and detect the photoelectron angular distribution in the $x-y$ plane, i.e. for $\theta = \pi/2$, as a function of the angle φ from the x-axis as shown in Fig. 4.15(b). The absorption of a photon will induce transitions with $\ell \to \ell \pm 1$ and $m \to m \pm 1$ due to the selection rules. The pathways from the ground (c) and the excited state (d) are shown in Fig. 4.15. The solid arrows represent the pathways for the transitions at the central frequency of the probe pulse. I_p is the ionization potential and the ovals indicate possible resonances. Since we analyze photolelectron emission induced by ultrashort pulses, we need to consider additional pathways due to the broad bandwidth of the pulse (Sec. 4.1). These pathways are the ionization from the ground state with a single photon and the two-photon transition from the excited state, which are represented by the dotted arrows in Fig. 4.15. Since states in the continuum with the same energy and quantum numbers can be reached via different pathways, the photoelectron angular distribution will change in both shape and yield as the relative amplitudes and phases of each signal varies.

4.3.1.2 Numerical solution of time-dependent Schrödinger equation

In order to test the applicability and limits of the reconstruction method we use numerical solutions of the time-dependent Schrödinger equation (TDSE) as substitute for actual measurements of the photoelectron angular distributions. We consider the TDSE in length gauge and single-active electron approximation as described in Chapter 3. We use a Helium SAE potential giving a ground state energy of -0.944409 a.u. and a $2p$ energy of -0.12847 a.u. The potential has been constructed for benchmark tests between TDSE and time-dependent density functional theory (TDDFT) calculations [204]. The energies match those of the corresponding DFT potential while the experimental values for the ground and the $2p$ state in helium are -0.9037 a.u. and -0.12382 a.u.

For the solution we have expanded $\Psi(\mathbf{r}, t)$ in spherical harmonics up to $l_{max} = |m_{max}| = 20$ and discretized the radius using fourth order finite difference. The wave function has been propagated in time with a time step of 0.01 a.u., on a grid with spacing of 0.05 a.u., maximum radius of 300 a.u., and exterior complex scaling on the outer 30 a.u. of the grid utilizing the Crank-Nicolson method for time propagation. The numerical code has been tested against previously used codes as well as results from numerical calculations published in the literature [217]. The electric field is a frequency corrected sine squared pulse. Once the wave function has been propagated to the end of the pulse we have obtained the photoelectron angular distribution by projecting onto numerical continuum states.

4.3.1.3 Perturbation theory

To reconstruct the initial wave function, i.e. determine amplitudes and phases, we invert the photoelectron angular distributions (here, TDSE results) as a function of time delay by utilizing perturbation theory (PT) described in Sec. 3.2. To evaluate the PT wavefunction, we use the bound states of the TDSE field free Hamiltonian for the initial states, and expand the Green's function for 200 dipole allowed states per ℓ and m block. The states represent the bound part of the spectrum and a discretized continuum up to an energy of ~ 59 eV. The matrix elements and time integrals are performed numerically.

The PT results are then used to obtain a residual

$$R(\mathbf{a}) = \sum_{k,\phi,\tau} \left| \frac{P_{\mathrm{TDSE}}}{\sum\limits_{k,\phi,\tau} |P_{\mathrm{TDSE}}|} - \frac{P_{\mathrm{PT}}(\mathbf{a})}{\sum\limits_{k,\phi,\tau} |P_{\mathrm{PT}}(\mathbf{a})|} \right|^2 \tag{4.12}$$

where P_{TDSE} and P_{PT} are the TDSE and PT photoelectron distributions for all utilized final momenta, time delays, and detection angles. The state vector $\mathbf{a}$ that minimizes $R(\mathbf{a})$ gives the reconstructed wave function. The normalization maintains the relative yields at each final momentum. To minimize $R(\mathbf{a})$ for the two (three) state system considered below, 1000 (250) evenly spaced samples were used. For the current applications, this minimization technique is sufficient. For superpositions involving more states the dimensionality of the minimization space increases. It is likely that for such studies more advanced minimization methods such as stochastic gradient descent will be needed. We also note that the method is applied to image field-free wave packets, i.e. $\mathbf{a}$ is time independent. For cases, in which $\mathbf{a}$ changes with time, an extension of the present method is needed.

4.3.2 Results and discussion

4.3.2.1 Reconstruction of two-state superposition: Intensity limits and number of samples

To apply the minimization and therefore reconstruct the wave packet, the photoelectron angular distributions (PADs) have to vary as a function of time delay. It is therefore first interesting to see at which laser parameters a significant variation in the PADs can be observed. To this end, in Fig. 4.16 we show how the PAD varies within one optical cycle of the pump pulse. The delay $\Delta\tau$ in the Figure refers to some fixed reference time τ_0 after the end of the first pulse. Comparison of the TDSE results for a two-cycle (~ 190 as FWHM, left column) and a ten-cycle (~ 950 as FWHM, right column) laser pulse at three peak intensities ranging from 10^{10} W/cm^2 (bottom row) over 10^{12} W/cm^2 (middle row) to 10^{14} (top row) W/cm^2 is shown. In these calculations the photon energy

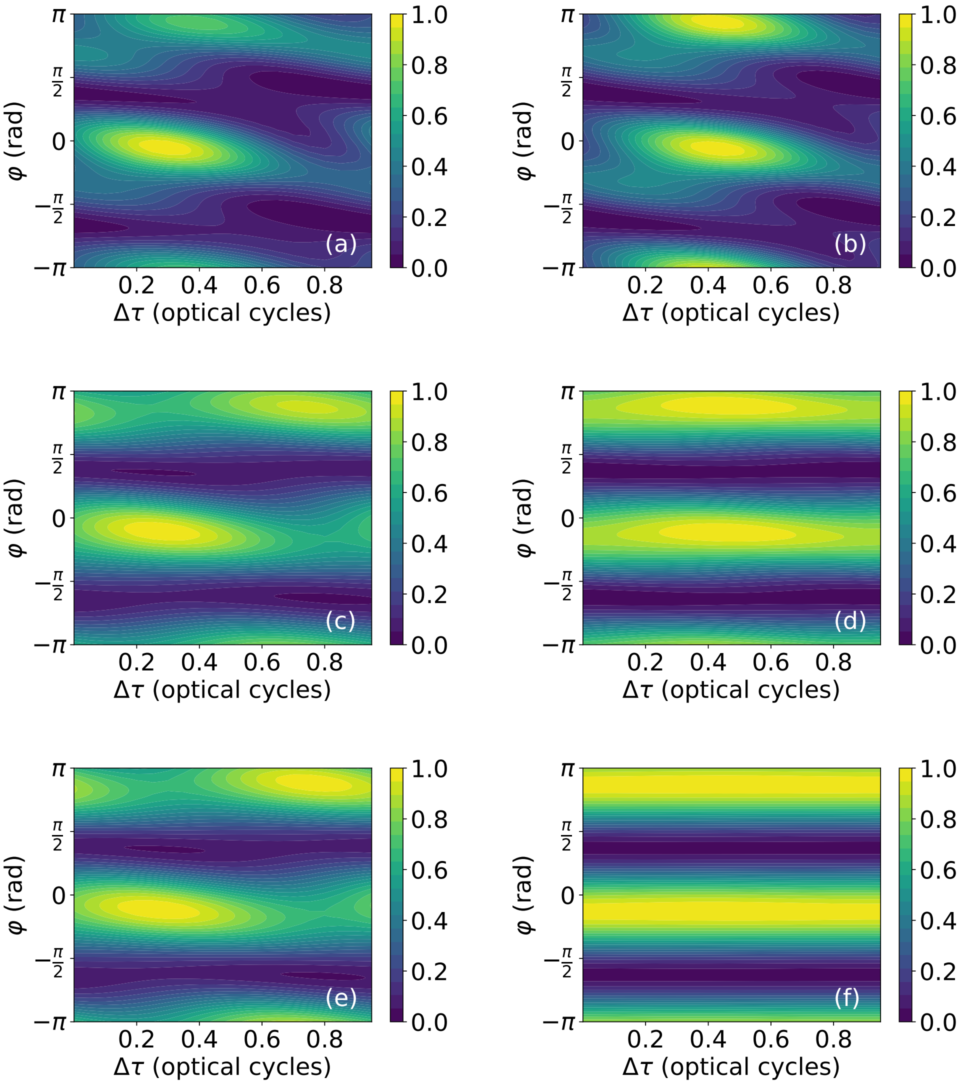

Figure 4.16: Results of TDSE calculations for photoelectron angular distributions over one cycle of the probe pulse field for ionization of $1s - 2p_1$ superposition with ultrashort two-cycle (left column) and ten-cycle (right column) laser pulse with peak intensities of 10^{14} W/cm^2 (top row), 10^{12} W/cm^2 (middle row), and 10^{10} W/cm^2 (bottom row). The time delays $\Delta\tau$ are given with respect to a reference time τ_0 after the end of the first pulse. (Figure from [233])

ω_E has been set to the energy difference between the initially equally populated field-free $1s$ and $2p_1$ states in helium atom $((|1s\rangle + |2p_1\rangle)/\sqrt{2})$. The angular distribution is taken at photoelectron energy $E = 2\omega_E - I_p$, where ω_E is the central photon energy and I_p is the ionization energy.

Although the laser pulse has a FWHM of similar or even longer duration than the charge migration in the present application, the time delayed PAD shown in Fig. 4.16 has significant enough variation for the minimization technique to converge. This is due to the coherent nature of the applied laser light. Since the laser is tuned near the resonance, the oscillation of the electric field approximately agrees with that of the superposition to be imaged. This allows for subcycle time dependence to be encoded in the PAD signal.

At the lowest intensity (Fig. 4.16, bottom row) we observe that the two-cycle signal varies significantly. This is due to the interference between the one-photon ionization channels from the excited state and the ground state. The pathway from the ground state provides a significant contribution to the electron emission due to the broadband spectrum of the ultrashort two-cycle pulse (Sec. 4.1 and Sec. 4.2). Thus, as the time delay varies, the relative phase of the ground and excited states changes producing a quantum beating. In contrast, for the longer ten-cycle pulse the spectrum of the pulse is more narrow. Consequently, the contribution from the one-photon pathway from the ground state is much smaller. Hence, the PAD for the ten-cycle pulse at the lowest intensity shows minimal variation as a function of time delay since it is dominated by ionization of the excited state.

As the intensity increases, the relative contribution of the two-photon ionization pathway from the ground state increases because the power dependence of the signals scales with the number of photons absorbed. Since the two-photon channel depends on the absorption of photons at the central energy the significance of the contribution does not depend on the pulse duration. As a result, we observe that at the largest intensity considered in Fig. 4.16 (top row) both the two- and the ten-cycle PADs vary strongly as function of the time delay. This is due to the interference between the one-photon ionization from the excited state and the two-photon ionization from the ground state.

To demonstrate the reconstruction method the errors in reconstructing the amplitude (a, d) and phase (b, e) of the superposition state $(|1s\rangle + |2p_+\rangle)/\sqrt{2}$ in helium atom as a function of peak intensity are shown in Fig. 4.17. The error is obtained via $\Delta a = a' - a$ where a is the amplitude or phase of the original wave function and a' is the corresponding amplitude or phase

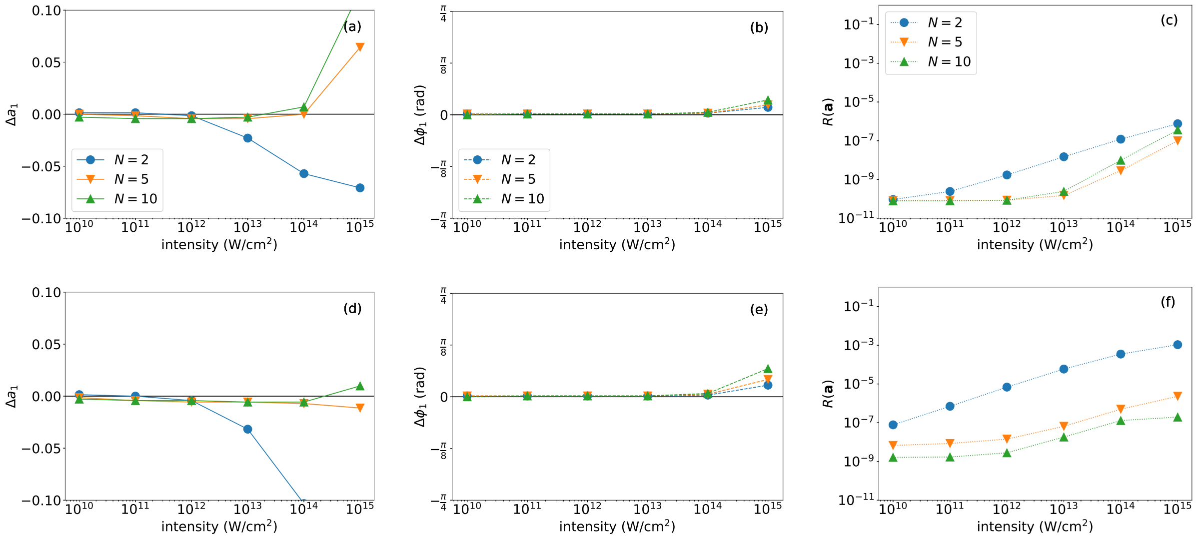

Figure 4.17: Errors in amplitude (a, d) and phase (b, e) for the two-state reconstruction using PADs generated with laser pulses at two, five and ten cycle pulse duration. Also shown is the residual $R(\mathbf{a})$ (c, f). The reconstructions are based on PADs at 20 time samples ($\Delta t = \tau/20$) using PADs in the full $x - y$ plane (upper row) and photoelectron signals in forward-backward direction (lower row). (Figure from [233])

of the reconstructed wave function. The reconstruction is based on PADs taken at 20 time delays over one period of quantum beating $\tau = 2\pi/|E_{2p_1} - E_{1s}|$. Also shown are the final results of the minimization for $R(\mathbf{a})$ (panels (c) and (f)).

Reconstructions of two cases are compared in which either the full PAD in the $x - y$ plane via signals at 6,285 equally spaced angles (upper row) or only the signals in the forward-backward direction along the polarization axis of the probe pulse (lower row) are used. The results in in the upper row show that the reconstruction method reproduces the initial state up to peak laser intensities of about 10^{13} W/cm^2 if the full $x - y$ plane and 20 time samples are used. The increase of the errors at intensities larger than 10^{13} W/cm^2 indicates that higher-order processes begin to contribute leading to the breakdown of the present second-order reconstruction method. For a two-state superposition just two amplitudes and the relative phase have to be determined. Using the full PAD with several thousand signals is oversampling for the reconstruction method. This is confirmed by the results for the reconstruction (d-f) using the PAD signals in forward-backward direction only.

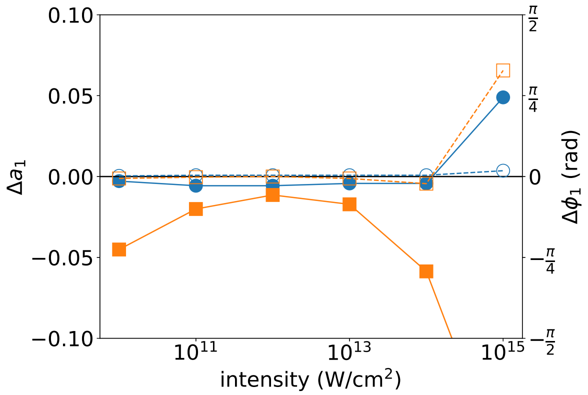

Figure 4.18: Same as Fig. 4.17 but based on PADs at just two time delays. Errors in amplitude (filled symbols with solid lines) and phase (open symbols with dashed lines) are shown for using PADs in the full $x - y$ plane (blue squares) and in forward-backward direction (orange circles). (Figure from [233])

Next, we have studied if one can limit the number of PAD samples over time. To this end, we present in Fig. 4.18 the errors in amplitude and phase based on a reconstruction using just two PADs over one period of quantum beating $\tau = 2\pi/|E_{2p_1} - E_{1s}|$. If the full PAD in the $x - y$ plane is used (blue squares) the reconstruction method remains successful over the same intensity regime as before. However, when the available signals are limited to the forward-backward direction (orange circles), the data are insufficient for a one-to-one mapping between the initial state and the obtained photoelectron signal. Consequently, the reconstruction fails at nearly all peak laser intensities, since for just two time samples the normalization leads to a greater chance that multiple values for amplitudes and the relative phase produce a given signal.

Thus, for the basic case of equal population in a two-state superposition and probing with a pulse having a central frequency equal to the field-free energy difference of the state, our results show that the reconstruction method is successful for intensities in the perturbative regime up to 10^{13} W/cm^2. If the PADs can be measured over a broad range of angles probing at two times over one cycle of the probe pulse field is sufficient. In contrast, if only the forward-backward asymmetry signals are measured more time samples are needed.

4.3.2.2 Impact of different pathways

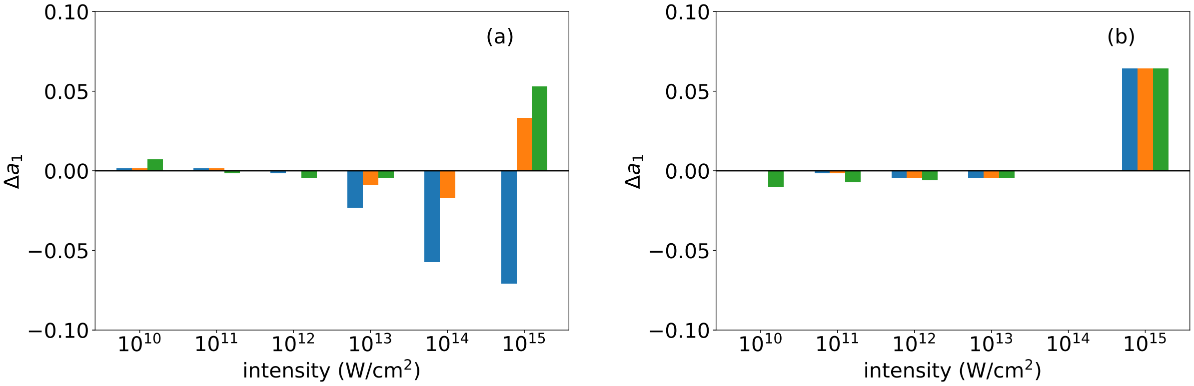

Figure 4.19: Comparison of amplitude error for (a) two and (b) five cycle probe pulse from calculations using full second order PT (blue), neglecting only the two-photon transition from the excited state (orange) and neglecting both the one-photon transition from the ground state and the two-photon amplitude from the excited state (green) in the reconstruction. (Figure from [233])

The reconstruction depends on the effective interference of at least two amplitudes to have a quantum beating. In the full reconstruction we consider the contributions from four pathways (one- and two-photon transitions from ground and excited states). It is interesting to ask which pathways contribute effectively besides the one-photon transition from the excited state. To study this question, we have deliberately neglected individual amplitudes in the reconstruction. In Fig. 4.19 we compare the results of these calculations with those of the full reconstruction (blue bars) based on the full $x-y$ plane and 20 time samples. We show the results for the amplitude error only and note that those for the phase error lead to the same conclusions.

We performed two set of test calculations: First, we utilized all amplitudes except the two-photon signal from the excited state (orange bars). Next, we have removed the one-photon signal from the ground state and the two-photon signal from the excited state from the reconstruction (green bars). Both transition amplitudes are expected to have an impact at ultrashort durations due to the broad bandwidth of the pulses. Indeed, we do see noticeable changes for the two-cycle data (a) while there appears to be insignificant impact for the five-cycle pulse (b) at all intensities.

For a two-cycle probe pulse, at intensities less than 10^{13} W/cm^2, the reconstruction without the two-photon amplitude from the excited state matches the full data (Fig. 4.17(a)). At higher intensities, the results deviate which agrees with the expectation. Removing also the one-photon transition from the ground state from the reconstruction causes the results to deviate from the full results at 10^{10} W/cm^2 and above 10^{13} W/cm^2. At the lowest intensity it is the one-photon signal from the ground state that provides a dominant contribution to the PAD, leading to the deviation at 10^{10} W/cm^2. At intensities above 10^{13} W/cm^2, the additional exclusion of the one-photon signal leads to a better reconstruction than for the full data and when the two-photon pathway from the excited state is neglected. This can indicate that inadvertently the two ultrashort amplitudes have an opposite effect on the reconstruction or that an even higher-order amplitude is more dominant than the lower-order processes.

4.3.2.3 Variation of central frequency and population

So far, we have considered a special case with equal population in the two states and the central frequency tuned to the energy difference between the two field-free states. We will now study deviations from this special case. First, we consider a laser pulse detuned from the energy difference between the two equally populated states. We have calculated the photoelectron distribution at $E = \omega_E - |E_e|$, where E_e is the energy of the excited $2p_1$-state. Given a sufficiently broad spectral range, i.e. sufficiently short pulse, the one-photon ground state signal (peaking at about $E = \omega_E - |E_g|$) at low intensities will interfere with the excited state signal creating the same quantum beating as before allowing for the reconstruction process to work. In Fig. 4.20 we show the reconstruction results for a laser with central frequency of $\omega_E = 0.8\omega_0$ (upper row) and $\omega_E = 1.2\omega_0$ (lower row). The results lead to the same conclusion as for the resonant case, namely that the reconstruction method can be applied in the perturbative intensity regime up to 10^{13} W/cm^2.

To show that the reconstruction works for a two-state superposition with arbitrary unknown amplitudes and phases, we have performed a ‘blindfold experiment’ where the population of the states were chosen randomly. The random values were held unknown and were only accessed to obtain the final error at the end of the reconstruction procedure. We have used this approach

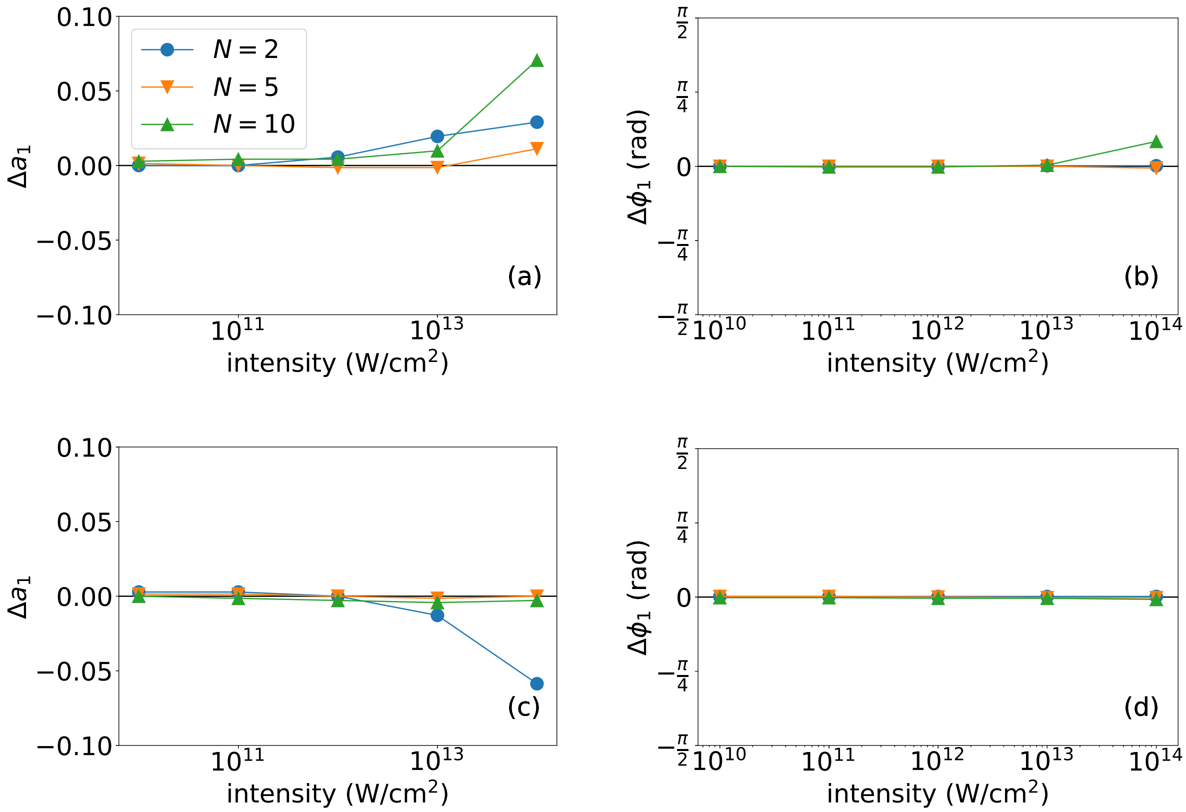

Figure 4.20: Amplitude (a, c) and phase (b, d) errors for ionization at a detuned photon frequency of $\omega = 0.8\omega_0$ (upper row) and $\omega = 1.2\omega_0$ (lower row). The reconstructions are based on full PADs in $x - y$ plane at 20 time delays. (Figure from [233])

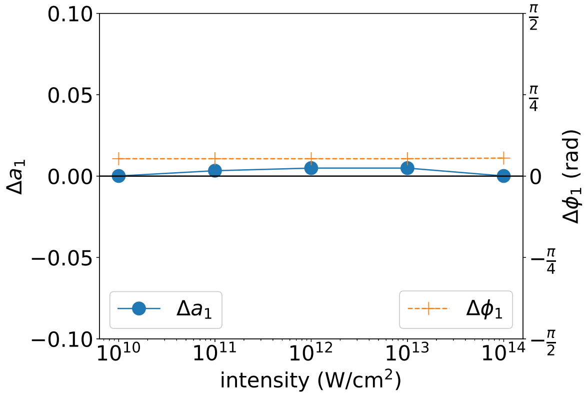

Figure 4.21: Amplitude and phase error for the reconstruction of an arbitrary unknown two-state superposition. Reconstruction is based on full PADs in $x-y$ plane at 20 time delays with a five-cycle probe pulse. (Figure from [233])

in several calculations and for probe pulses of different duration, with results leading to the same conclusion. As an example, one set of results for this ‘blindfold’ experiment is presented in Fig. 4.21, showing that the reconstruction is successful with the same low errors as in the other cases studied.

4.3.2.4 Detector accuracy and variation of laser parameters

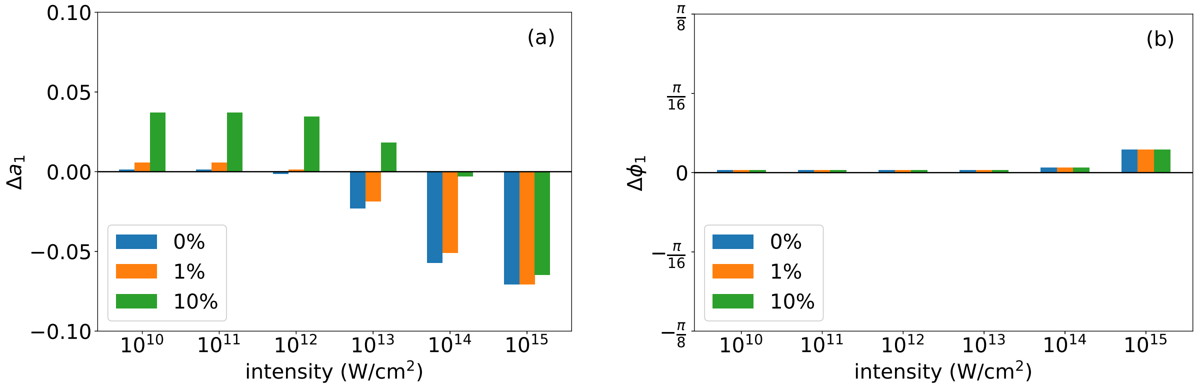

Figure 4.22: Comparison of (a) amplitude and (b) phase error for reconstruction using PADs at machine precision (blue) and with accuracy limited to 1% and 10%. (Figure from [233])

For the reconstructions so far we have used results from TDSE calculations up to machine precision. Since detectors in experiment do not operate with the same precision we have studied how less accurate data may impact the success of the reconstruction. To this end, we have deliberately added random noise at a certain percentage level of the maximum signal in the PADs to the TDSE data. In Fig. 4.22 we compare the results for the reconstruction with added noise at the 1% and 10% level with those at machine precision using the signals from the full $x - y$ plane and 20 time samples. It is seen that an accuracy of detection at the 1% level is sufficient to reconstruct the wavefunction with similar error as in the full calculation with TDSE data at machine precision. Similar results and conclusions have been obtained for the other cases presented in Figs. 4.17 and 4.18. We expect that this limit can be achieved in a measurement.

We have further considered variations in the laser parameters relevant for an application of the reconstruction method in an experiment. Typically, the peak intensity of the applied laser

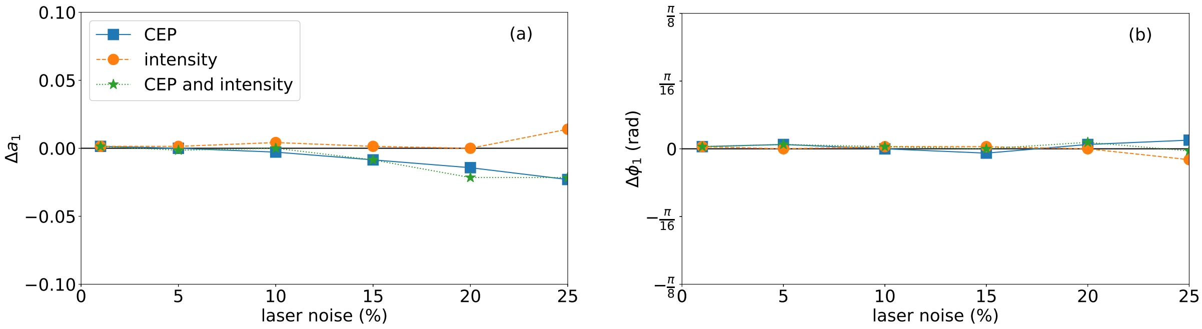

Figure 4.23: Amplitude (a) and phase (b) error for variation of CEP only (blue squares with solid lines), intensity only (orange circles with dashed lines) and both CEP and intensity (green stars with dotted lines) at peak intensity of 10^{11} W/cm^2 and pulse duration of 2 cycles. Reconstruction is based on full PADs in $x-y$ plane at 20 time delays. (Figure from [233])

pulse may vary from shot to shot as well as over the interaction volume. Another parameter that is usually difficult to control is the carrier-to-envelope phase (CEP) of a laser pulse, specifically for ultrashort pulses. To study the impact on the reconstruction, CEP, peak intensity, and both CEP and peak intensity have been varied randomly within a certain percentage in the TDSE results. The results in Fig. 4.23 show that the reconstruction method still works well up to 10% variation in both parameters before significant errors occur. Perhaps most surprising is the rather large acceptable tolerance in the CEP even for the shortest pulses, since CEP variations often lead to large changes in experimental observables. We assume that the shot to shot variation is 'averaging out' over the various time delays leading to a quality in the reconstruction similar to fitting a linear regression to noisy data.

4.3.2.5 Extension to superpositions of more than two states

Finally, we consider the extension of the reconstruction method to a superposition of more than two states. The ionization scheme shown in Fig. 4.15(c) and (d) can be applied to each excited state in the superposition separately, taking the waves generated via one- and two-photon transitions from the ground state as reference. For the reconstruction measurement of PADs at separate energies for each excited state in the superposition is required. Based on PT results, residuals $R(\mathbf{a})$ (Eq. 4.12) have been obtained, taking into account both final momenta to reconstruct the wave function.

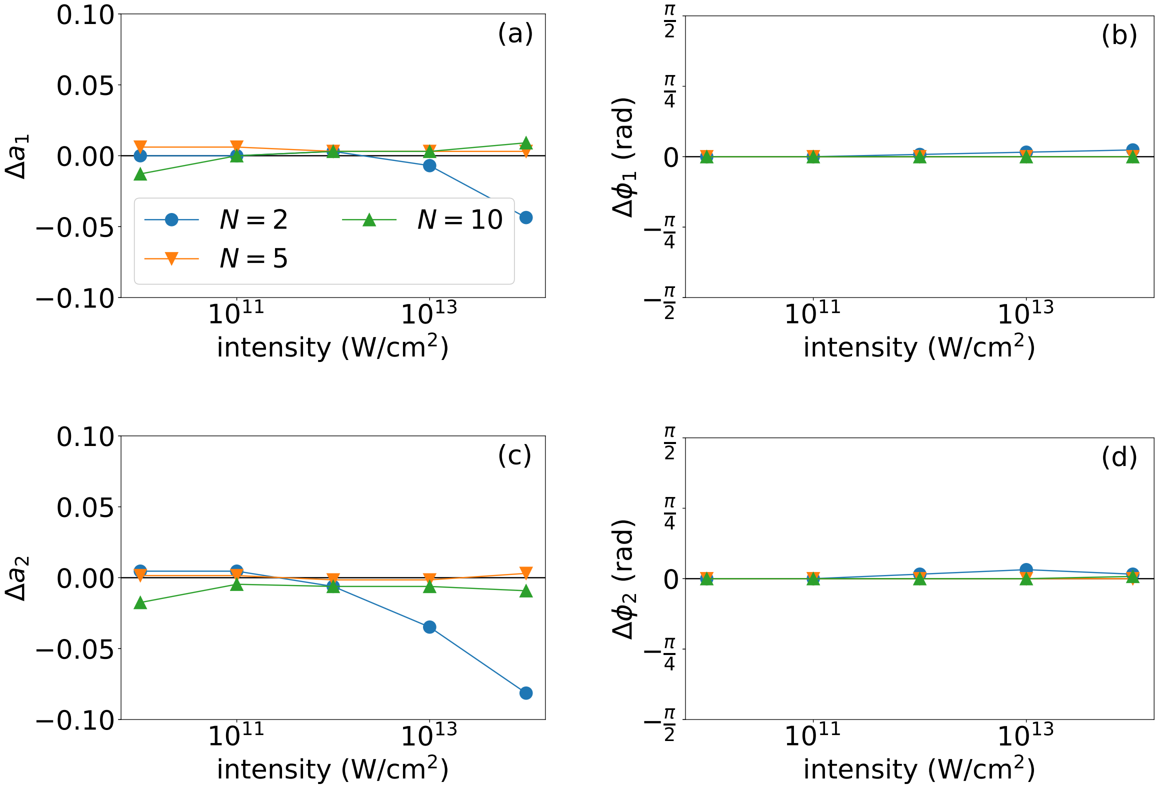

Figure 4.24: Amplitude (a, c) and phase (b, d) errors for the reconstruction of the superposition $(|1s\rangle + |2p_1\rangle + |3p_1\rangle)/\sqrt{3}$ in the helium atom (upper row: errors for $2p$-state, lower row: errors for $3p$-state). (Figure from [233])

To test the extension of the method we have considered the helium atom in the $(|1s\rangle+|2p_1\rangle+|3p_1\rangle)/\sqrt{3}$ superposition. A probe laser pulse at central photon energy tuned halfway between the $|2p_1\rangle$- and $|3p_1\rangle$-state and measurement of PADs at both $E = \omega - |E_{2p}|$ and $E = \omega - |E_{3p}|$ have been applied. The results of the reconstruction, based on PADs in the full $x-y$-plane taken at 20 time delays, are shown as function of peak intensity for different pulse durations in Fig. 4.24. The results show that a similar degree of accuracy in the reconstruction as for the two-state superposition is achieved within the same intensity limits. The example indicates that the present method may be extended to even more complex wave packets and electron dynamics.

Extension of the reconstruction method to more complex superpositions will however require attention to the interference with the ground state signal and the increased dimensionality of the minimization space. Since the minimization process appears to be convex, a standard minimization algorithm, like stochastic gradient descent, may be sufficient for an efficient reconstruction. For each additional state in the interference scheme, the signal at the photoelectron energy chosen must include interference with at least one other state. This can be achieved if all transitions from the excited states interfere with that from the ground state by using a short pulse. If only longer pulses are available, coupling over many pairs of states reduces the required bandwidth for a reconstruction. Finally, due to the selection rules some initial states do not generate a signal in the xy-plane. In this case it may be required to utilize a full 4π-PAD for reconstruction of the corresponding superposition.

4.3.3 Summary and outlook

In this section we have studied the use of perturbation theory to reconstruct an atomic wave function representing ultrafast field-free charge migration. In the reconstruction scheme the photoelectron angular distributions obtained by ionizing an atom, prepared in a superposition of two or three states, are used. The electron dynamics are encoded in the PAD signal via interference of the ground and excited state ionization signals. Time delayed measurements allow for the extraction of all amplitudes and phases of the initial wavefuction that fully characterizes the charge migration. Results of applications based on TDSE calculations show that the reconstruction is highly accurate for probe pulse intensities below 10^{13} W/cm^2 while allowing for CEP (intensity) variations of 10% (20%) from shot to shot. Additionally, a detection accuracy for the PADs of about 1% for a reconstruction with small error is required.

These results may provide some basic guidelines for future experimental progress in imaging electron motion on its fundamental time scale via the detection of photoelectron angular distributions. However, the results also show that experimental challenges remain. Controlling the creation of ultrashort laser pulses, especially those with attosecond pulse duration, is a non-trivial task. For the current method to be applied, average values for intensity, CEP and pulse duration of the electric field of the probe pulse must be obtained and shot-to-shot variations must be limited up to a certain degree. Given the rate of advancement in attosecond laser pulse technology over the last decade, this level of pulse control may be, however, achieved in the coming years.

Additionally, precise knowledge of one- and two-photon transition dipoles is required to perform perturbation theory calculations for the target atom with high accuracy. Over the last decades several standard theoretical methods, such as multielectron theories, density functional theory or calculations using accurate single active electron potentials, have been developed to perform such calculations. As theoretical methods for bound and continuum wave functions further advance, the current and other reconstruction methods will become increasingly accurate.

Chapter 5

Rydberg state excitations induced by intense near-infrared radiation

In the previous chapter, we have studied ionization of atoms involving few photons. We will now turn our attention to processes in strong-field physics where many-photon processes driven by intense IR lasers are studied. When large numbers of photons are absorbed, the discrete nature of the multi-photon picture begins to blurs, allowing for processes to be understood in a complementary way through classical trajectory analysis and tunneling processes. Fundamental processes in strong-field atomic physics are above-threshold ionization (ATI) [4], high harmonic generation (HHG) [71, 164, 62], and non-sequential double ionization [239]. These highly nonlinear processes are induced by the absorption of multiple photons from the laser field, which in the limit of a large photon number can also be described as a tunneling process. Excitation of the atom is known to play an important role in each of the processes. It has been initially observed via resonant enhancement in the population of excited states [42, 119] and structures in the energy spectrum [72, 190, 3] and in energy-resolved angular distributions [209] of photoelectrons. These resonance effects have been explained by multiphoton absorption through Rydberg states, which are AC-Stark shifted in the presence of a laser field. More recently, significant excitation of atoms has also been observed in the tunneling regime and described by the frustrated tunneling ionization model [180].

For linearly polarized lasers, the latter observation has renewed the general interest in the mechanisms leading to the population of excited (Rydberg) states during the interaction of an atom with an intense laser pulse (most recently, e.g., in Refs. [38, 145, 144, 260, 221, 32, 142, 59, 27, 73, 152, 219, 89, 176, 248, 19, 138, 261, 22, 74, 115, 109, 156, 247, 194]). The important role of Rydberg states in various strong-field ionization processes and harmonic generation has been discussed. For example, resonant enhancement of below-threshold harmonics [227, 38, 32], emission from excited states via free induction decay [32, 19], high harmonic emission through ionization from excited states and recombination to the ground state [23, 19] have been predicted and observed.

Recent theoretical studies of the excitation mechanism in linearly polarized strong fields mainly consider the distribution of the population as a function of the principal quantum number of the excited states [145, 144, 261, 247, 194]. It was shown that the modulation of the excitation probability is related to the channel closing effect [134, 145, 144, 194]. Theoretical analysis of the angular momentum distribution in the populated Rydberg states by linearly polarized fields is less advanced. Predictions of Floquet theory for a monochromatic laser field [134] and results of numerical calculations for laser pulses with a trapezoidal envelope [194] yield that the angular momentum of the excited Rydberg states has the same parity as $N_p - 1$, where N_p is the minimum number of photons needed to ionize the atom. Furthermore, the angular quantum number of the states with the largest population in numerical calculations [145, 144, 194] agrees well with semiclassical estimations [6], initially performed for low-energy angular resolved photoelectron distributions.

Besides interactions with linear polarized laser pulses, recently studies on the interaction of atoms and molecules with intense fields generated by the superposition of two circularly polarized laser pulses have seen an upsurge in activity in strong-field experiment and theory. For the most part, the renewed interest results from the capability to control the polarization of emitted light in high-order harmonic generation with such pulses. The physical principle has been proposed and applied first two decades ago [53, 150]. More recently, efficient phase matching of circularly polarized high-order harmonic beams in the EUV and soft X-ray regime using bichromatic beams with counter-rotating circular polarization has been demonstrated [64, 196, 125, 58, 100]. Since then, much experimental and theoretical work on high-harmonic generation [169, 165, 170, 36, 17, 98, 149, 159, 10, 203, 181, 46, 63, 258, 195, 18, 139, 7, 43, 12, 108, 117, 99, 184, 143], ionization and photoelectron momentum distributions [175, 254, 167, 157, 168, 156, 189, 29, 101, 146, 1, 30, 50, 141, 87, 49, 148, 55, 76, 124, 2], double ionization [155, 51, 21, 44, 252, 107, 154] and other strong-field processes [253, 28, 84] driven by bichromatic circularly polarized laser pulses has been performed. One interesting aspect in these kind of strong-field interactions is the control of ionization via the helicity of the applied bichromatic pulses [167, 157, 148]. Such studies complement related work on the dependence of the ionization rate by one-color circularly pulse on the relative helicity between the pulse and the electron in the atomic orbital [14, 122, 96, 15, 16, 13, 182, 90, 47, 244, 241, 255, 52, 147, 228].

For the interaction with bichromatic circularly polarized laser pulses resonant excitation also plays an important role. It has been observed that the probability to ionize an atom is significantly enhanced if the two fields are counter-rotating as compared to co-rotating fields [157]. The experimental observations were interpreted as due to the increased density of excited states accessible for resonant enhanced multiphoton ionization in the case counter-rotating fields. Results of numerical solutions of the time-dependent Schrödinger equation in Ref. [157] did confirm a close relation between the ratios of total excitation and ionization probabilities for counter-rotating and co-rotating circularly polarized laser pulses. However, the results for excitation of the atom were not further resolved by distributions over the quantum numbers (principal, angular momentum, magnetic). Such analysis potentially can shed further light on the role of excited states in the pathways to ionization since excitation in a resonant multiphoton process should rely on the spin-angular momentum selection rules for the absorption of circularly polarized photons ($\Delta l = \pm 1$ and $\Delta m = \pm 1$).

In this chapter, we present results for excitation of atoms with linearly polarized (Sec. 5.1) and bi-circular (Sec. 5.2) laser pulses. Interpretation of the distributions of excitation over the states with different quantum numbers will be given using multiphoton selection rules.

5.1 Linear polarization[1]

As mentioned before, for the interaction with linear polarization earlier work for monochromatic laser fields [134] and laser pulses with a trapezoidal envelope [194] have been performed.

---

[1] The content of this section has been also published in J. Venzke et al., Physical Review A **98**, 043434 (2018).

Here, we extend these previous analysis by considering excitation in laser pulses with more realistic sine-squared and Gaussian envelopes. This gives us the opportunity to study if the parity of the populated angular momentum states in such pulses agrees with the selection rules obtained for monochromatic fields and how the results depend on the pulse length at low and high intensities. In Sec. 5.1.2 we then investigate how the population of angular momentum states leaves its footprints in the radiation generated via transitions from the excited states to the ground state.

For our studies we have made use of results of numerical solutions of the time-dependent Schrödinger equation (TDSE) for the interaction of the hydrogen atom with an intense linearly polarized laser pulse. Specifically, we are solving the time-dependent Schrödinger equation (TDSE) for the interaction of an atom with a linearly polarized intense laser pulse in the velocity gauge (Eq. 3.3) for the Hydrogen atom ($V_{SAE}(r) = -1/r$). The code utilizes cylindrical coordinates and second order finite difference. In all calculations presented below we used a grid ranging up to $\rho =$ 750 a.u. and $z = \pm 750$ a.u. with a grid spacing of $\Delta = 0.1$ a.u. in both directions and a time step of $\Delta t = 0.15$ a.u. We use the outer 37.5 a.u. of the grid in both directions for the ECS potential. This grid can easily fit bound states up to $n = 14$ within the real portion of the grid.

5.1.1 Angular momentum distributions

5.1.1.1 Parity effect in pulses

We study the angular momentum distribution in Rydberg states of the hydrogen atom. To this end, we consider processes during which these states are shifted into resonance with multiphoton absorption from the initial ground state of the atom (with energy E_i). Assuming that the energy shift of high lying excited states under the influence of an intense laser field is approximately equal to the ponderomotive shift [3] and the shift occurs instantaneously during the pulse [93], the intensity for a N_p photon process to resonantly excite approximately with an excited state with energy E_n is then given by:

$$I = 4\omega_E^2(N_p\omega_E + E_i - E_n). \tag{5.1}$$

In our calculations we have considered peak intensities such that the $n = 8$ states are in resonance at central frequency ω_E, corresponding to a wavelength of 800 nm, with $N_p = 10, 11, \ldots, 15$ photon processes. Since we study the interaction with laser pulses, instead of monochromatic fields, more than one manifold of states can be resonantly excited. For example, the bandwidth of a 20 cycle sine squared pulse at 800 nm covers all excited states $n \gtrapprox 6$ within the same N_p photon process. We further note that in the present cases, the $n = 3$ and $n = 2$ states are approximately resonant via $N_p - 1$ and $N_p - 2$ photon processes, respectively, assuming that the energy shift of these states equals the ponderomotive energy as well.

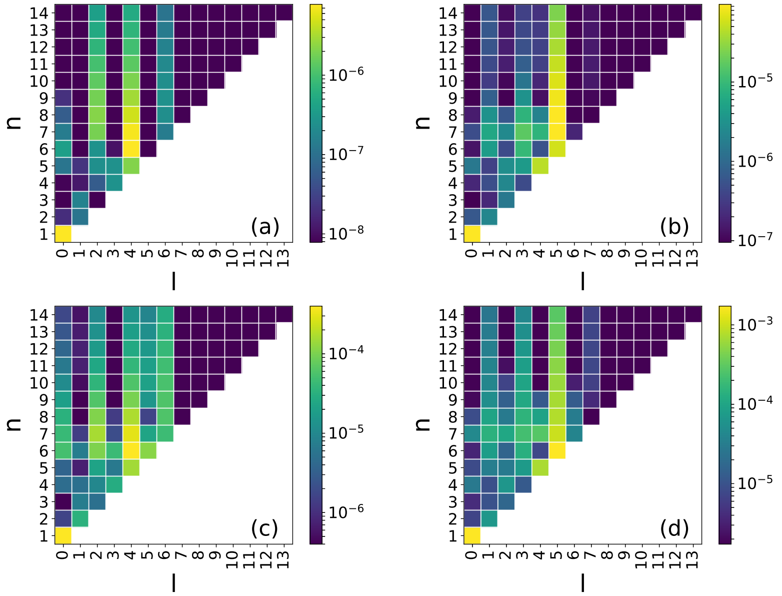

Figure 5.1: Excited state distribution as function of n (vertical axis) and l (horizontal axis) at the end of 20 cycle pulses with sine-squared envelope and peak intensities: (a) $I_0 = 3.4 \times 10^{13}$ W/cm^2, (b) $I_0 = 6.0 \times 10^{13}$ W/cm^2, (c) $I_0 = 8.6 \times 10^{13}$ W/cm^2, and (d) $I_0 = 1.12 \times 10^{14}$ W/cm^2. Left (right) column corresponds to cases in which the Rydberg states are resonant with an even (odd) number of photons. (Figure taken from [237])

The population in each quantum state (n, l) at the end of the pulse is shown in Fig. 5.1 (20 cycle pulses with sine-squared envelope) and Fig. 5.2 (14 FWHM cycle pulses with Gaussian envelope) for intensities between 10^{13} and 10^{14} W/cm^2. The results shown in the left (right) column correspond to cases in which the Rydberg states are resonant with an even (odd) number of photons. In all cases we see that the highest angular momentum states ($l > 7$) are not vary

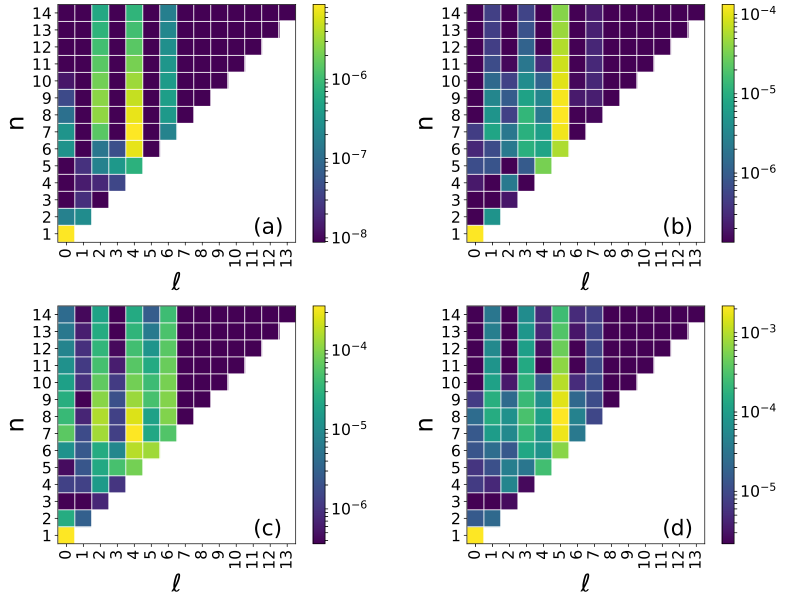

Figure 5.2: Same as Fig. 5.1 but for pulses with Gaussian envelope and 14 cycles FWHM. The pulse duration approximately matches that for the sine-squared pulses in Fig. 5.1 at FWHM. (Figure taken from [237])

populated, in agreement with previous studies [194] and semiclassical estimates [6]. In the results we indeed observe signatures of the selection rules resulting in dominant population of states with an even (odd) angular momentum quantum number for the absorption of even (odd) photons in the plots on the left (right). This shows that in the intensity regime of 10^{13} to 10^{14} W/cm^2 the parity selection rules, previously studied for monochromatic fields and flat-top pulses, are effective for long pulses of about 20 cycles. Since the parity effect is found to occur independent of the form of the envelope we restrict ourselves below to pulses with sine-squared envelope. However, we observe that the contrast between the population in even and odd states is stronger at lower intensities. We will further discuss this aspect in subsection 5.1.1.2.

The results also show that for an odd parity process (right column) predominantly one angular momentum state ($l = 5$) is populated. This is in agreement with the results presented by Li et al. [144], who conjectured that electrons in the low angular momentum states more easily absorb additional photons resulting in suppression of population in these states due to ionization. However, our results for even parity processes exhibit a pattern, alternating in l, showing that both low and high angular momentum states, except for the s-states, remain populated at the end of the pulse.

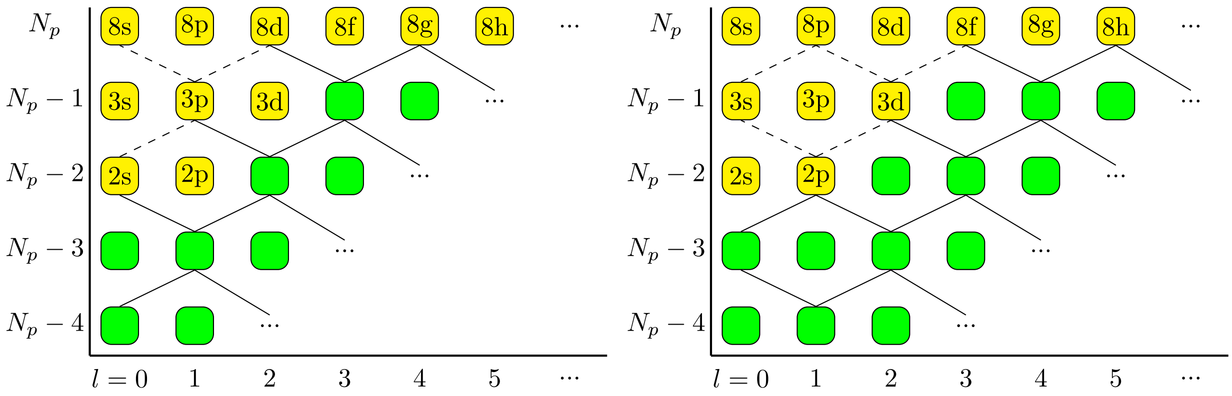

Figure 5.3: The absorption pathways in an even (odd) photon process in the left (right) panel. Green squares represent virtual states with energy $N\omega$ above the ground state and angular momentum l. The yellow squares represent real states labeled by the quantum numbers. Solid lines refer to open pathways while dashed lines represent pathways which are suppressed due to population trapping in a lower excited state. (Figure taken from [237])

We therefore put forward an alternative explanation. To this end, in Fig. 5.3 we show the various pathways leading to a resonant population in the $n = 8$ (and the other Rydberg) states for absorption of an even (top panel) or an odd (bottom panel) number of photons, termed by N_p. Starting from the 1s ground state, the absorption of successive photons proceeds through virtual states (depicted via empty green squares in Fig. 5.3), following the selection rule $\Delta l = \pm 1$. As mentioned above, for the hydrogen atom and a pulse at a central wavelength of 800 nm the (shifted) $n = 3$ and $n = 2$ states are approximately resonant via $N_p - 1$ and $N_p - 2$ photon processes, as shown in Fig. 5.3 (real states are depicted by yellow squares labeled with quantum number nl). Assuming that the resonant transitions to lower lying energy levels cause a trapping of population in these states, further absorption from these states will be suppressed. Such suppressed pathways are denoted by dashed lines in Fig. 5.3, while other (open) pathways are represented by solid lines. Following the pathways, we see that in the manifold of the Rydberg levels for an even number photon process (left panel) the $l = 2$ state is partially and the $l = 4, 6, \ldots$ states are fully accessible, while the $l = 0$ (s-state) should be suppressed, which is in agreement with the pattern, alternating in l, that we observe in Figs. 5.1 and 5.2 (left columns). In contrast, for an odd number photon process (right panel) the pathways to the $l = 1$ states are strongly and those to the $l = 3$ states are partially suppressed, making the states with $l = 5$ state the first fully accessible states among the Rydberg levels, in agreement with the results presented in Figs. 5.1 and 5.2 (right columns).

5.1.1.2 Short vs. long pulses and CEP effects

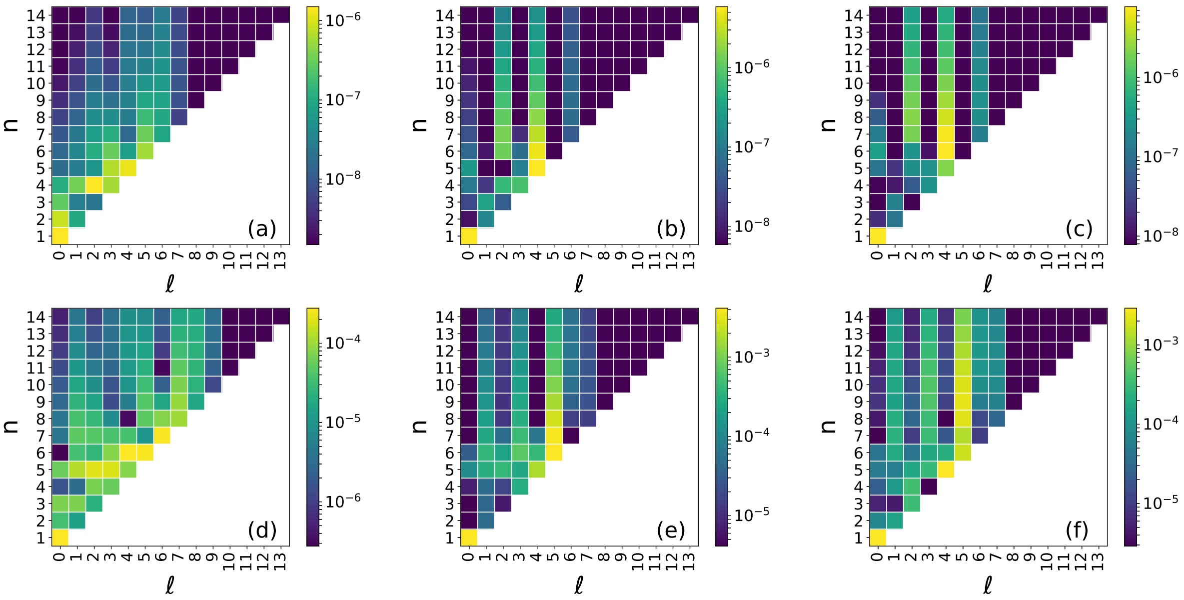

Figure 5.4: Excited state distribution as function of l (horizontal axis) and n (vertical axis) at the end of 2 cycle (panels on left), 10 cycle (panels in middle), and 20 cycle (panels on right) pulses, at low peak intensity $I_0 = 3.4 \times 10^{13}$ W/cm^2 (top row), and high peak intensity $I_0 = 1.64 \times 10^{14}$ W/cm^2 (bottow row). (Figure taken from [237])

The time-frequency uncertainty relation yields that a pulse spectrum broadens as the number of optical cycles decreases. Consequently, in an ultrashort pulse an excited state can be reached via absorption of different number of photons. Due to this mix of even and odd number of photon processes one may expect that in such pulses a separation in population of odd vs. even angular momentum quantum states cannot be achieved. This is confirmed by the results of our numerical calculations at low and high intensities, shown in Fig. 5.4(a) and (d). For a 2 cycle pulse there is a smooth distribution over the lower angular momentum states for each principal quantum number at low (3.4×10^{13} W/cm^2, panel (a)) and high (1.64×10^{14} W/cm^2, panel (d)) peak intensity.

In contrast, the narrowing of the energy spectrum as pulse duration increases does not necessarily lead to an increase of the population in the angular momentum states of one parity over the other. For the low intensity 10-photon resonant process (3.4×10^{13} W/cm^2, Fig. 5.4, upper row) we observe in the numerical results that Rydberg states with a well defined angular momentum parity are predominantly populated when the pulse duration is increased to 10 and 20 cycles. On the other hand, at the higher intensity (1.64×10^{14} W/cm^2, Fig. 5.4, lower row) we observe some contrast between the population in the angular momentum states of different parity for the 10 cycle pulse (panel (e)), while the differences in the population of the different channels further blurs when the duration is increased to 20 cycles (panel (f)).

Within the interpretation of resonant excitation the loss of the parity effect for long pulses with high peak intensities can be understood as follows. At the higher peak intensity, the highly excited states are shifted into resonance for 10-14 photon processes over the rising and trailing parts of the pulse, before they are resonantly excited with a 15 photon process at the peak intensity. Although the excitation probability raises with an increase of the intensity during the pulse, the time intervals over which the states are in resonance with a certain photon-order process increase with the pulse length. Thus, there is a significant excitation of the Rydberg states due to the absorption of odd as well as even numbers of photons in a pulse at high peak intensity and long duration.

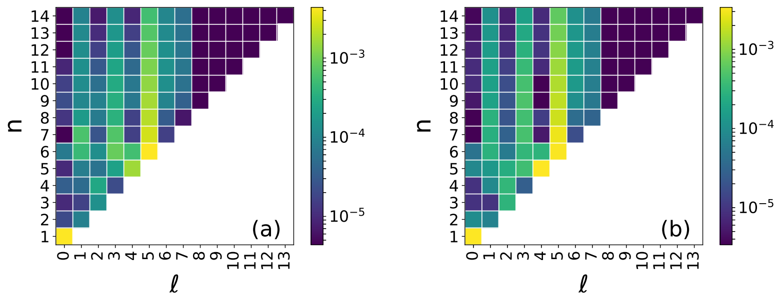

Figure 5.5: Population of excited states from a 20 cycle pulse with peak intensity of $I_0 = 1.64 \times 10^{14}$ W/cm^2 and CEP of $\phi_A = 0.204\pi$ (a) and $\phi_A = 0.882\pi$ (b). (Figure taken from [237])

Furthermore, excitation channels driven by absorption of different numbers of photons with the same parity may interfere, leading to the enhancement or suppression of population in certain angular momentum states and the loss of the parity effect. Interference effects in excitation have been studied extensively in the few-photon regime. Among others, it has been shown that the excitation probabilities can be controlled via the carrier envelope phase (CEP) of the pulse, even in the long pulse limit (e.g., [257, 245]). We observe in the results presented in Fig. 5.5 that the population distribution in the angular momentum states driven by the present more complex multiphoton processes indeed changes significantly with variation of the CEP at high intensities, indicative of potential interference effects.

We note that there may exist alternative explanations for the loss of the parity effect in the distribution at long pulses with high peak intensity. For example, in the tunneling regime the mechanism of frustrated ionization has been explored [180]. According to that mechanism highly excited states are populated during the trailing edge of the pulse by deceleration of the electron over many laser cycles and electron recapturing once the laser pulse ceases. Since excited states of any angular momentum can be populated during the recapturing, the loss of the parity effect for long pulses at intensities in the tunneling regime is consistent with the frustrated ionization mechanism as well.

5.1.2 Radiation spectra

It has recently been discussed [38, 32, 19] that the population of excited Rydberg states leads to the emission of radiation due to the transition from the excited states into the ground state, which can be observed in the below-threshold part of high harmonic spectra. In the case of atomic hydrogen such emission is associated with an excitation of the *np* states. In view of the parity effect in the excitation of the Rydberg states according to the absorption of an even or odd number of photons, we expect that the emission may be enhanced or suppressed in certain intensity regimes. To allow for the separation between the field induced and field free radiation we have calculated the high harmonic spectrum from the dipole acceleration $a(t)$ such that

$$f_{HHG}(\omega; t_f) \propto \int_{-\infty}^{t_f} a(t')e^{-i\omega t'}dt'. \tag{5.2}$$

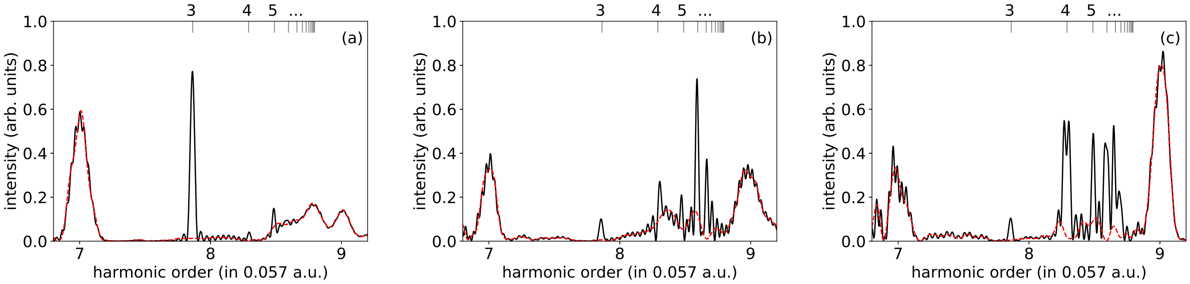

Figure 5.6: Radiation spectra generated during the pulse (red dashed lines) and those including line emissions after the pulse (black solid lines) are shown for peak intensities: (a) $I_0 = 3.4 \times 10^{13}$ W/cm^2, (b) $I_0 = 6.0 \times 10^{13}$ W/cm^2, and (c) $I_0 = 1.64 \times 10^{14}$ W/cm^2. The vertical gray lines show the field free energy differences between the np energy levels (up to $14p$) and the $1s$ ground state. (Figure taken from [237])

In Fig. 5.6 we present the radiation spectrum in the region of the 7th and 9th harmonics produced by a 20 cycle, sin squared, 800 nm pulse at intensities (a) $I_0 = 3.4 \times 10^{13}$ W/cm^2, (b) $I_0 = 6.0 \times 10^{13}$ W/cm^2, and (c) $I_0 = 1.64 \times 10^{14}$ W/cm^2. In each panel the red dashed line shows the spectrum generated during the pulse ($t_f = \tau$) while the black solid line includes free propagation after the pulse has ended ($t_f = 2\tau$). The difference between the two spectra exhibits the radiation related to the transitions from the populated excited np states at the end of the pulse to the ground state, which has previously been identified in both experiment [38] and macroscopic simulations [32, 19].

Comparison of the spectra obtained at the two intensities clearly exhibits the expected difference in the features related to the parity effect in the population of the Rydberg states. At an intensity of 3.4×10^{13} W/cm^2 (Fig. 5.6a), the (shifted) Rydberg energy levels are resonantly excited with a 10 photon process leading to population of the even angular momentum states. Consequently, the spectrum is free of line emission from the almost unpopulated Rydberg p-states while we find a strong line corresponding to the strongly populated $3p$ state, which is near resonant with a 9 photon process. In contrast, by shifting the states by the energy of an additional photon, at an intensity of 6.0×10^{13} W/cm^2 (Fig. 5.6(b)) we observe a rich line emission spectrum just below the 9th harmonic line emissions from the *np*-states, that are resonantly populated by a 11 photon process. We note that the 6*p* and 7*p* states are the most populated *np* states and as a result have the strongest emission lines. On the other hand the line corresponding to the 3*p* state, which cannot be populated by absorption of 10 photons, is strongly suppressed.

As discussed in section 5.1.1.2, at the highest intensity $I_0 = 1.64 \times 10^{14}$ W/cm^2, the population distribution in the angular momentum well defined parity begins to blur. This leads to a relatively even population in states with principle quantum number 4 to 14 seen in (Fig. 5.4(f)). As a result, we see in Fig. 5.6(c) line emission from all populated *np* states with similar strengths for the states resolved in our spectrum.

5.1.3 Summary

We have analyzed in this section the angular momentum distribution in the Rydberg states of a hydrogen atom excited by a short strong laser pulse, based on numerical results of the time dependent Schrödinger equation, which we solved using a second order Crank-Nicolson scheme. At low intensities the pattern in the population across the angular momentum states can be explained via a parity effect due to the selection rules in multiphoton absorption along with the suppression of pathways due to population trapping in low excited states, if the applied laser pulse is not too short. At high intensities the parity effect gets lost even for long pulses, potentially since the Rydberg states are in resonance with photon processes of different orders for a significant time during the rising and trailing parts of the pulse. We predict that the parity effect can be observed via the strengths of the line emissions from the *np* states emitted after the end of the pulse.

5.2 Bi-circular polarization[2]

The time-dependent Schrödinger equation for the interaction of a electron in the potential of the hydrogen atom with a superposition of two circularly polarized intense laser pulses in dipole approximation and velocity gauge is given in Eq. 3.3[3] . The wavefunction Ψ is expanded in spherical harmonics up to $l_{max} = 45$ and $m_{max} = 45$. The radius is discretized using fourth order finite difference method with a grid spacing of 0.1 a.u. and a maximum radius of 750 a.u. with exterior complex scaling on the outer 38 a.u. of the grid. The wavefunction is propagated in time using the Crank-Nicolson method with a time step of 0.05 a.u. The choice of gauge was based on the faster convergence of calculations in the velocity gauge for expansions of the wavefunction in spherical harmonics [41, 88].

The interaction with the bicircular laser pulse is implemented via the total vector potential as:

$$\mathbf{A}(t) = \mathbf{A}_{\omega}(t) + \mathbf{A}_{2\omega}(t) \tag{5.3}$$

where

$$\begin{aligned} \mathbf{A}_{\Omega}(t) &= A_{0,\Omega} \sin^2\left(\frac{\pi t}{\tau_{\Omega}}\right) \\ &\quad \times \left[\sin\left(\Omega t\right)\hat{\mathbf{x}} + \epsilon_{\Omega}\cos\left(\Omega t\right)\hat{\mathbf{y}}\right] \end{aligned} \tag{5.4}$$

for $\Omega = \omega$ and 2ω, respectively. $A_{0,\Omega} = \frac{c\sqrt{I_{\Omega}}}{\Omega}$, $\tau_{\Omega} = \frac{2\pi N_{\Omega}}{\Omega}$, and c is the speed of light, where I_{Ω} is the peak intensity and N_{Ω} denotes the number of cycles. $\epsilon_{\Omega} = \pm 1$ denotes the helicity of the fundamental and 2nd harmonic pulse, respectively.

We have performed numerical calculations for the interaction of hydrogen atom with co- and counter-rotating bicircular pulses operating at the central wavelengths of 800 nm and 400 nm. Intensities of the two pulses were varied to study the distribution in the excited states as function

---

[2] The content of this section has been also published in J. Venzke, Y. Gebre, et al., Phys. Rev. A **101**, 053425 (2020).

[3] The corresponding numerical code has been developed by another graduate student (Y. Gebre). Results of that code have been tested well against results obtained using length gauge with the numerical program described in this thesis.

of all quantum numbers, principal, angular momentum and magnetic. For the results presented below we have used pulses with the same pulse duration in time.

5.2.1 Excitation with co-rotating pulses

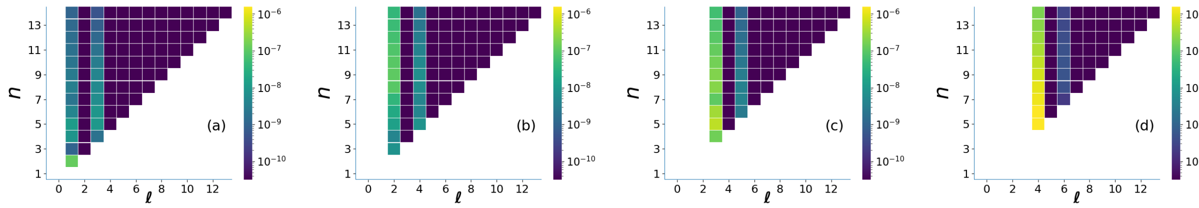

Figure 5.7: Excited state distribution as function of n (vertical axis) and ℓ (horizontal axis) for (a) $m = -1$, (b) $m = -2$, (c) $m = -3$ and (d) $m = -4$ at the end of 20 (at 800 nm) cycle pulses (40 cycle at 400 nm) with sin squared envelope and total peak intensity of 1×10^{14} W/cm^2 for co-rotating laser pulses of equal intensity. (Figure taken from [234])

Selection rules for (single-)photon absorption from circularly polarized light are given by $\Delta l = \pm 1$ and $\Delta m = \pm 1$, where the change in the magnetic quantum number is positive (negative) if the helicity of the light is right- (left-)handed. Extending the concept to multiphoton absorption, the simultaneous change in both quantum numbers puts distinct constraints on the parity and helicity of the accessible excited states in the atoms upon absorption of multiple photons. Specifically, it is expected that states in which ℓ and m are either both even or both odd are being populated during the interaction with the field. This selection holds for the interaction with a single circularly polarized pulse as well as for the case of a superposition of two (or more) of such fields, independent of the relative helicity of the two pulses.

In Fig. 5.7 we show examples of the population in the excited states of hydrogen atom as a function of n and ℓ for various m values at the end of the interaction with bichromatic co-rotating left-handed circularly polarized pulses. The results clearly confirm the expected population distribution in states with either odd or even parity for a given value of m according to the selection rules upon multiphoton absorption. The present results have been obtained for interaction with equal peak intensities $I_{400} = I_{800} = 5 \times 10^{13}$ W/cm^2.

Due to the correlation in changes of m and ℓ the observed pattern is independent of total peak intensity, ratio of peak intensities and pulse duration, as long as the dipole approximation holds. In our studies we have verified this up to intensities of 1×10^{14} W/cm^2. This is different from the case of linear polarization [237], where selective population concerning the parity of the populated excited states is observed for long pulses and low peak intensities only. In that case the restriction to a given m-channel and a broad energy spectrum (for short pulse durations) or a significant Stark shift of the excited states (at high peak intensities) leads to a mixing of population over the states with odd and even orbital angular momentum quantum numbers.

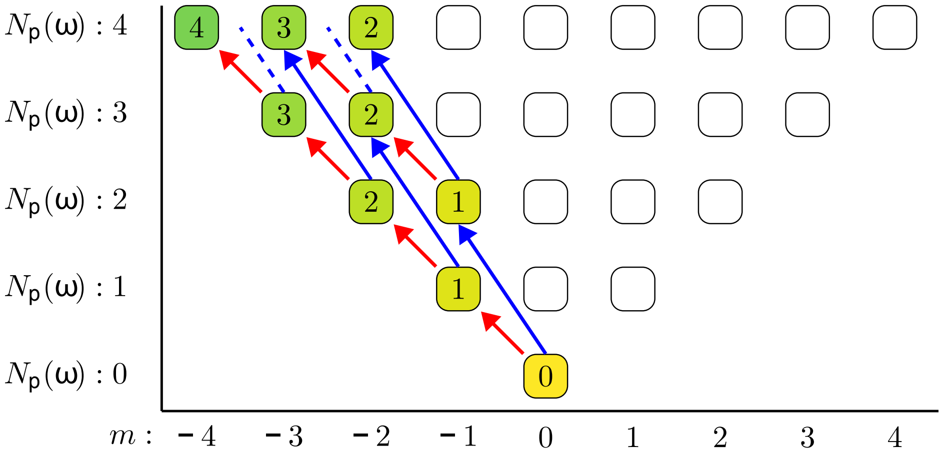

Figure 5.8: Absorption pathways in co-rotating laser pulses at frequencies ω and 2ω starting from a $m = 0$-state. Without lack of generalization it is assumed that both pulses have left-handed helicity. Absorption of a photon at frequency ω and at frequency 2ω is represented by a red and blue arrow, respectively. The numbers in the boxes denote the minimum number of photons to reach a certain level. (Figure taken from [234])

In co-rotating bicircular laser pulses all the photons have the same spin (either +1 or −1), consequently the magnetic quantum number always changes either by $\Delta m = +1$ or by $\Delta m = -1$ upon absorption of each photon. For our studies we have chosen left-handed helicity for both pulses and, hence, only excited states with negative m can be populated upon absorption of photons from the ground state with $m = 0$ (c.f., Fig. 5.8). Therefore, as already mentioned in Ref. [156], only Rydberg states with high orbital angular quantum number ℓ are accessible. For example, for excitation of Rydberg states (with $n \geq 4$) in the hydrogen atom, the absorption of at least 4 photons in laser field at 400 nm or at least 8 photons at 800 nm is required. Thus, Rydberg states with $\ell < 4$ (and $m > -4$) cannot be populated just via photon absorption alone.

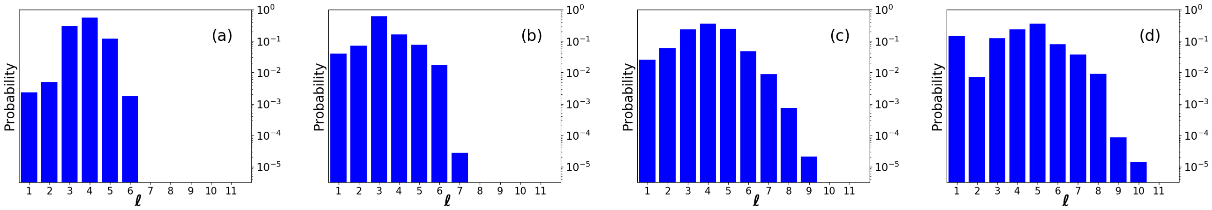

Figure 5.9: Excited state distribution as function of orbital angular quantum number ℓ summed over $n \geq 4$ and m at (a) $I_{400} = 5 \times 10^{13}$ W/cm^2, $I_{800} = 5 \times 10^{12}$ W/cm^2, (b) $I_{400} = 5 \times 10^{13}$ W/cm^2, $I_{800} = 1 \times 10^{13}$ W/cm^2, (c) $I_{400} = 5 \times 10^{13}$ W/cm^2, $I_{800} = 5 \times 10^{13}$ W/cm^2, and and (d) $I_{400} = 1 \times 10^{13}$ W/cm^2, $I_{800} = 5 \times 10^{13}$ W/cm^2. Pulse durations: 20 cycles at 400 nm, 10 cycles at 800 nm. (Figure taken from [234])

Accordingly, the angular momentum distribution in the Rydberg states is controlled via the relative intensity of the two fields at the fundamental and second harmonic frequency. This is demonstrated in Fig. 5.9, where the excited state distribution as a function of ℓ, summed for $n \geq 4$ and all m, is shown. For large ratio of $I_{400}/I_{800} = 10$ (panel (a)) the distribution is centered, as expected, about $\ell = 4$. As the intensity ratio decreases, high orbital angular momentum states get increasingly populated due to the impact of the laser pulse at 800 nm.

Another interesting feature in Fig. 5.9 is that the population in angular momentum states with $\ell < 4$ increases significantly when the intensities of the two pulses are similar. Further insight can be gained by the distribution over the magnetic quantum number, which is displayed in Fig. 5.10(c) for the case of equal intensities. It is clearly seen that Rydberg states with magnetic quantum numbers between $m = 0$ and $m = -3$ are populated. In view of the number of photons needed to reach the Rydberg levels, the population in these states cannot be explained by absorption of photons only.

Instead, we propose the following mechanism: Initially, Rydberg states with $\ell \geq 4$ are populated via the absorption pathways shown in Fig. 5.8. Then a redistribution of population occurs via Raman-type Λ-transitions (c.f., [81, 60]). In the present bichromatic laser field the Λ-process

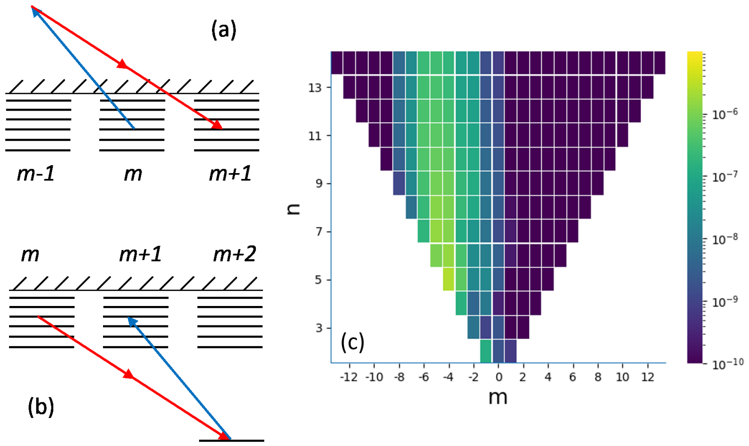

Figure 5.10: Excited state distribution as function of n (vertical axis) and m (horizontal axis) summed over ℓ. Laser parameters: 20 (800 nm) cycle pulses with sin squared envelope and total peak intensity of 1×10^{14} W/cm^2 for co-rotating laser pulses of equal intensity. (Figure taken from [234])

leads to a change in the magnetic quantum number, if photons from both fields are involved. For the absorption of one 400 nm photon and emission of two 800 nm photons the magnetic quantum number between initial and final state changes by $\Delta m = +1$.

The order of absorption and emission may vary, i.e., the redistribution process can either proceed via the continuum (absorption first, Fig. 5.10(a)) or via a lower excited state (emission first, Fig. 5.10(b)). A larger change in m is achieved either via a sequence of these Λ-processes or by higher order processes (e.g., absorption of two 400 nm photons followed by emission of four 800 nm photons leading to $\Delta m = +2$). We note that similarly the absorption of two photons at 800 nm and the emission of a 400 nm photon will lead to a change of $\Delta m = -1$ in the present set-up and, hence, contribute to population of states with higher ℓ and m.

Our interpretation is further supported by the results in Fig. 5.11, which shows how the population in states of certain quantum numbers for (a) $\ell = 2$ and (b) $\ell = 3$ changes as function of the relative intensity of the two pulses. It is clearly seen that the population in these quantum states, which are not accessible via direct absorption of photons from the ground state, increases as the intensity of the pulse at 800 nm increases. Thus, these results provide further indications that the

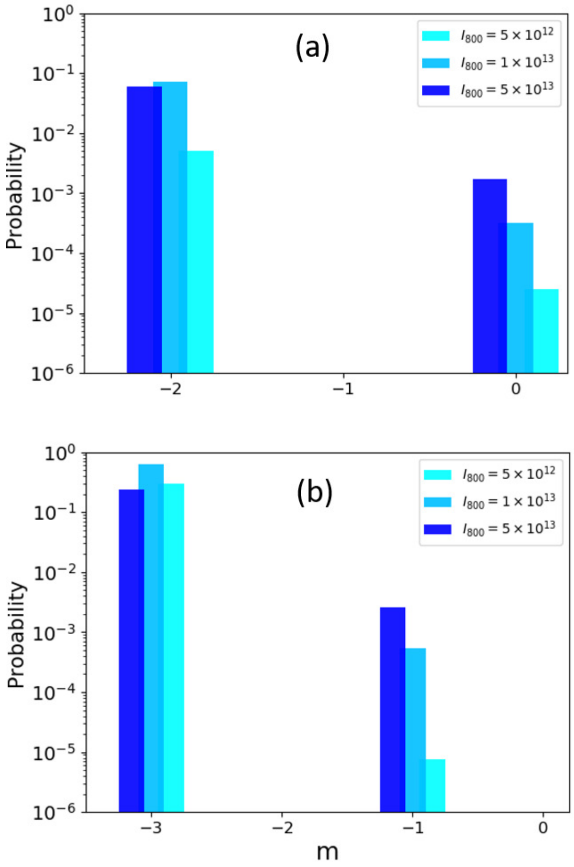

Figure 5.11: Distribution in magnetic quantum states for (a) $\ell = 2$ and (b) $\ell = 3$ and different peak intensities of the 800 nm pulse. $I_{400} = 5 \times 10^{13}$ W/cm^2 and other parameters are as in Fig. 5.10. (Figure taken from [234])

presence of the redistribution process depends on the impact of both pulses and its effectiveness increases with increase of the total intensity, in agreement with our interpretation of a Λ-type process. The redistribution of population in Rydberg states via higher-order Raman-like process induced by co-rotating bi-circular laser fields has been further studied in a project led by another graduate student [77].

5.2.2 Excitation with counter-rotating pulses

As discussed in the previous subsection, the selection rules by which only states with ℓ and m either both even or both odd hold independent of the relative helicity of the two pulses. This

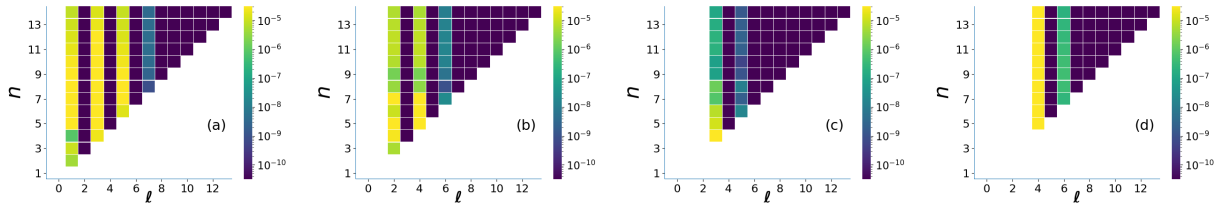

Figure 5.12: Same as Fig. 5.7 but for counterrotating laser pulses. (Figure taken from [234])

is confirmed by the results that we obtained for the interaction with two counterrotating pulses at equal intensities and equal pulse duration presented in Fig. 5.12. Depending on whether m is even or odd, the distribution over the orbital angular momentum shows population in states with even or odd parity. As in the case of corotating pulses, the observed pattern is found independent of total peak intensity, ratio of peak intensities and pulse duration.

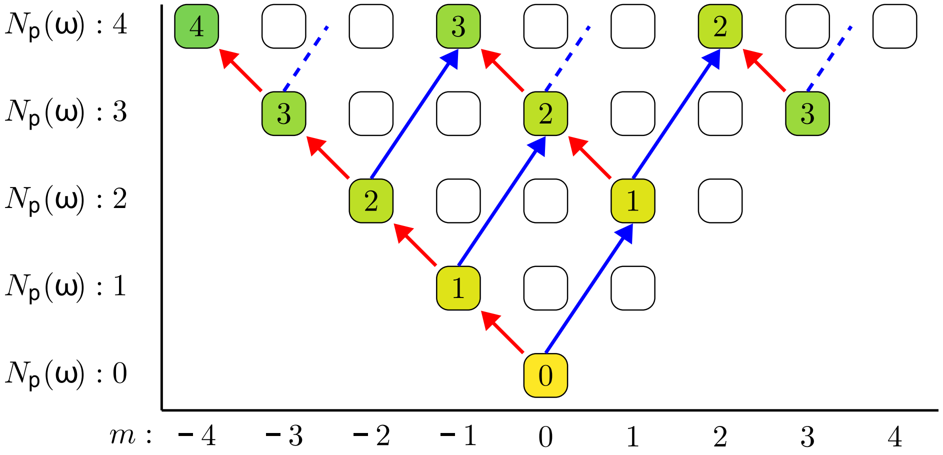

Figure 5.13: Absorption pathways in counter-rotating laser pulses at frequencies ω and 2ω starting from a $m = 0$-state. Without lack of generalization it is assumed that the pulses at frequency ω has left-handed helicity, while the second harmonic pulse has right-handed velocity. Other symbols as in Fig. 5.8. (Figure taken from [234])

Since in counter-rotating bicircular laser pulses photons of the two fields have opposite spin, starting from the ground state with $m = 0$, excited states with both positive and negative magnetic quantum numbers can be populated. The absorption pathways for the set-up chosen in the present studies, namely right-handed helicity for the 800 nm pulse and left-handed helicity for the second harmonic, are shown in Fig. 5.13. As can be seen from the Figure, the magnetic quantum number reflects the difference between the number of 400 nm photons and that at 800 nm absorbed. Furthermore, it can be seen that for a given total photon energy absorbed states with magnetic quantum numbers separated by $\Delta m = \pm 3$ are populated.

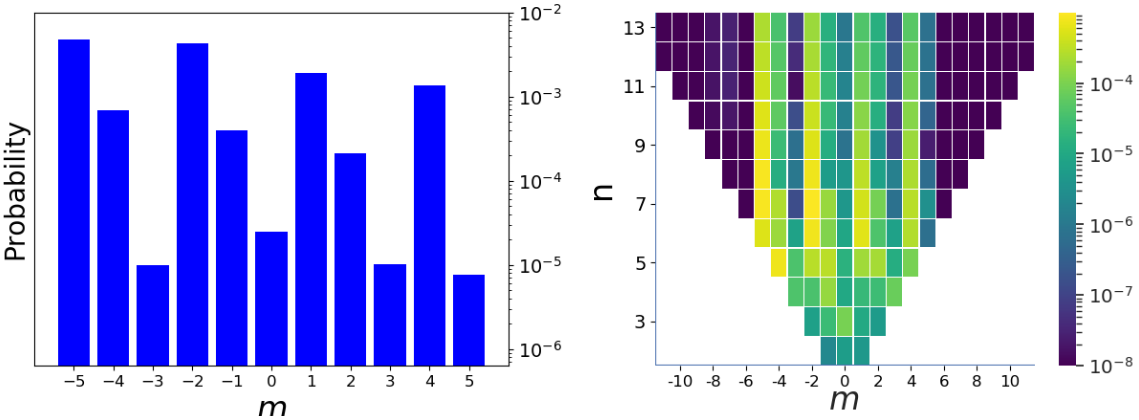

Figure 5.14: Excited state distributions as a function of m, summed over $n \geq 4$ and ℓ (top), and as a function of n and m, summed over ℓ (bottom), for the interaction with a left-handed circularly polarized laser pulse at 800 nm (20 cycles) and a right-handed circularly polarized laser pulse at 400 nm (40 cycles). Both pulses have the same peak intensity of 5×10^{13} W/cm^2. (Figure taken from [234])

These features are clearly present in the population distributions as function of m, summed over n and ℓ (top), and of n and m, summed over ℓ (bottom), in Fig. 5.14, which show the results for counter-rotating pulses of equal peak intensity. In the Rydberg manifold ($n \geq 4$) the highest populated m-states differ by $\Delta m = \pm 3$, other states show some but lower population as the manifold is AC-stark shifted during the interaction with the pulses. In view of the nonlinearity of multiphoton processes, it is likely that the states showing the largest probability are being populated near the peak of the pulses at which the highest total intensity is present. Overall, the strongest population is seen for states with negative magnetic quantum numbers, leading to the conclusion that it most likely that either five (for excited states with $m = -5$) or two (for excited states with $m = -2$) more 800 nm photons with left-handed helicity than 400 nm photons with right-handed helicity are being absorbed.

The distributions in Fig. 5.14 do not extend much beyond $|m| = 5$, which is consistent with

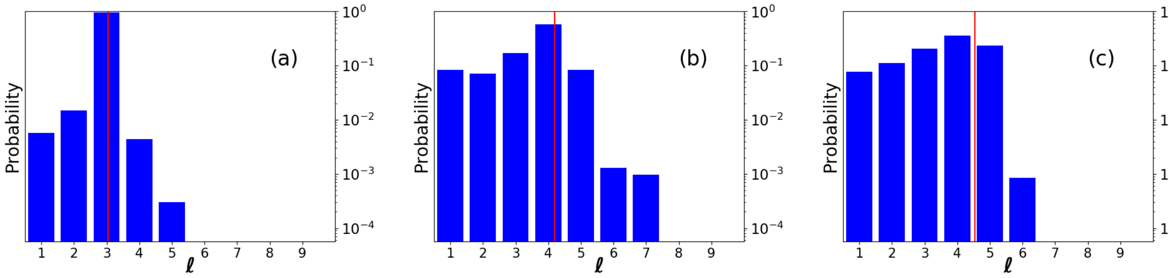

Figure 5.15: Orbital angular momentum distributions in excited states induced by counter-rotating laser pulses at 400 nm (20 cycles) and 800 nm (10 cycles) at peak intensities of (a) $I_{400} = 5 \times 10^{13}$ W/cm^2, $I_{800} = 5 \times 10^{12}$ W/cm^2, (b) $I_{400} = 5 \times 10^{12}$ W/cm^2, $I_{800} = 5 \times 10^{13}$ W/cm^2, and (c) $I_{400} = 5 \times 10^{13}$ W/cm^2, $I_{800} = 5 \times 10^{13}$ W/cm^2. (Figure taken from [234])

the results shown in Fig. 5.15 showing that there appears to be a highest orbital angular momentum number ℓ_{max} beyond which the population in the states drops off quickly. This is in agreement with previous studies for Rydberg state excitation [194, 237] and low energy angular momentum distributions [6]. In Ref. [6] a random walk analysis of the absorption pathways between the accessible quantum states is used to obtain the classical orbital angular momentum for a electron with zero energy in a laser field has been derived as $L = \sqrt{2Z\alpha_0}$ where Z is the charge of the residual ion and α_0 is the quiver radius. Relating classical orbital angular momentum and the orbital angular momentum quantum number by $\ell \approx L - 1/2$ we have estimated the maximum ℓ gained in the bicircular counter-rotating pulse. The estimates, shown by the solid red lines in Fig. 5.15, are in good agreement with the cut-offs seen in the numerical results. We note that the random walk analysis of Ref. [6] can be applied in the case of counter-rotating pulses, since in each absorption step $\Delta m = \pm 1$ and hence, in general, $\Delta \ell = \pm 1$ is possible. In contrast, for co-rotating pulses the changes in magnetic and angular quantum number are determined in each absorption step ($\Delta m = -1$, $\Delta \ell = +1$) and hence a random walk analysis is not applicable and a cut-off cannot be derived.

5.2.3 Summary

In this section we have studied the distributions over the orbital angular momentum (ℓ) and magnetic (m) quantum numbers in Rydberg states due to the interaction with bichromatic circularly polarized laser pulses. Multiphoton selection rules lead to population of states in which ℓ and m are either both even or both odd, independent of relative helicity, peak intensity and pulse duration. In the case of co-rotating pulses the results show that the distribution over the magnetic quantum number can be controlled via the intensities of the two pulses. Furthermore, we propose that the states are populated via direct absorption from the ground state and via Λ-type transitions between Rydberg states of different ℓ and m, involving two photons at the fundamental wavelength and one photon at the second harmonic. For bicircular laser pulses with opposite helicities Rydberg states with magnetic quantum numbers that differ by $\Delta m = \pm 3$ are predominantly populated. The pattern allows to gain insights into the relative number of photons absorbed from the two fields. The distribution is however restricted by the maximum orbital angular momentum quantum number that can be estimated by classical considerations.

Chapter 6

Towards studies of correlation effects in attosecond electron dynamics

Solving the TDSE for two active electrons is a computationally difficult task. A naive approach would be to discretize the six spatial dimensions using finite difference. This approach would provide a straightforward solution and runs well on supercomputing systems, however, the size of the wavefunction scales like N^6 where N is the number of grid points in each dimension. Therefore, if one were to use a typical grid of 1000 points in each dimension, the wavefunction would be 10^{18} points in size. Merely writing down the wavefunction in double precision floating point numbers would require 16 Exabytes of RAM, approximately 100 times more RAM than exists on the largest supercomputer in the world (Summit, Oak Ridge Leadership Computing Facility). Instead, it is more convenient to choose a coordinate system and basis that greatly reduces the size of the problem. One common approach is to use bi-spherical harmonics (e.g. [231]). In this case, the position of each electron is expanded in 3D spherical coordinates. The radius is discretized with finite difference, B-splines, finite-element discrete variable representation (FEDVR), or similar method, and the two angular coordinates are expanded in the standard 3D spherical harmonics in the same way a single-active electron code would do. When taking the tensor product of the two electrons, the electron-electron repulsion term is then expanded in spherical harmonics such that

$$\frac{1}{|\mathbf{r}_1 - \mathbf{r}_2|} = 4\pi \sum_{\ell=0}^{\infty} \sum_{m=-\ell}^{m=\ell} \frac{1}{2\ell+1} \frac{r_<^{\ell}}{r_>^{\ell+1}} Y_{\ell m}^*(\theta_1, \phi_1) Y_{\ell m}(\theta_2, \phi_2). \tag{6.1}$$

This results in a representation of the 6D space that can be used to solve the problem of two electrons in a molecular or atomic potential interacting with a laser.

In the bi-spherical codes, one must discretize two radii. As the grid increases in size, the code still scales like N^2. To circumvent this problem, we have implemented a code that contains a single hyper-radius (R) and five angles that are expanded in 6D hyperspherical harmonics. Therefore, as the grid size is increased, the code scales like N and the number of spherical harmonics is controlled by the laser parameters. In the following section, we will describe the details to utilize two different "coordinate systems" that solve the two active electron problem. The first is based on the use of Jacobi coordinates, which allows for the finite mass of the nucleus to be accounted for. The second is applied when using the infinite mass approximation for the nucleus, which allows that the distance between the two electrons to be accessed more directly. The two problems can be solved with similar sized wavefunctions, however, the time to calculate matrix elements is greatly reduced in the second method.

This chapter covers the background for the TDSE program developed in hyperspherical coordinates in Sec. 6.1 including the definition of hyperspherical harmonics in Sec. 6.1.1, the application of Jacobi coordinates in Sec. 6.1.2, and the application of electron coordinates in Sec. 6.1.2. A discussion of the implementation of the code and first tests will be presented in Sec. 6.2 while Sec. 6.3 provides a brief overview of the challenges that remain and useful next steps which could make it possible to run fully correlated two-electron calculations on desktop machines.

6.1 TDSE in hyperspherical coordinates

The TDSE

$$i\frac{\partial}{\partial t}\Psi = \hat{H}\Psi \tag{6.2}$$

with Hamiltonian written in hyperspherical coordinates is given by

$$\hat{H} = -\frac{1}{2}\left[\frac{1}{R^5}\frac{\partial}{\partial R}\left(R^5\frac{\partial}{\partial R}\right) - \frac{\hat{K}^2(\Omega_5)}{R^2}\right] + \frac{W(\Omega_5)}{R}\,, \tag{6.3}$$

where $R = \sqrt{\sum_i x_i^2}$ is the hyperradius with x_i being a Cartesian coordinate, $\hat{K}$ is the angular momentum operator, Ω_5 is the solid angle in 6D (5 angles), and $V(\mathbf{R}) = W(\Omega_5)/R$ being the potential. We will use the hyperspherical harmonics which contain two-3D sub spaces as described in Sec. 6.1.1. The resulting volume elements are

$$d\tau = R^5 dr d\Omega_5 \tag{6.4}$$

$$d\Omega_5 = \cos^2\alpha \sin^2\alpha d\alpha d\omega \tag{6.5}$$

$$d\omega = \sin\theta_{\mathbf{r_1}} d\theta_{\mathbf{r_1}} d\phi_{\mathbf{r_1}} \sin\theta_{\mathbf{r_2}} d\theta_{\mathbf{r_2}} d\phi_{\mathbf{r_2}} \tag{6.6}$$

where θ_i and ϕ_i denote the angles in the $i = \mathbf{r_1}$ and $i = \mathbf{r_2}$ sub coordinate systems and α is the angle produced by the right triangle with sides R, r_1, and r_2 as shown in Fig. 6.1. r_1 and r_2 will denote the Jacobi Coordinates, if a finite mass nucleus is considered, or the single electron coordinates when the infinite mass approximation is made.

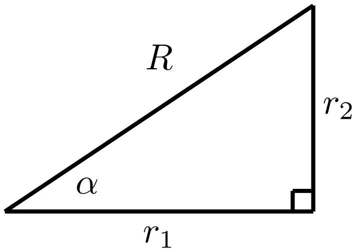

Figure 6.1: Relation of the hyperradius (R) to the two single-electron sub coordinate systems (r_1, r_2).

As for the 3D TDSE, it is beneficial to remove the first derivative in the radial equation. This is accomplished by substituting $\Psi = \psi/R^{5/2}$ to get as Hamiltonian

$$\hat{H} = -\frac{1}{2}\left[\frac{\partial^2}{\partial R^2} - \frac{\hat{K}^2(\Omega_5) + 15/4}{R^2}\right] + \frac{W(\Omega_5)}{R}. \tag{6.7}$$

The wavefunction can now be written as

$$\psi = \sum_{\mathbf{K}} U_{\mathbf{K}}(R) Y_{\mathbf{K}}(\Omega_5) \tag{6.8}$$

with $U_{\mathbf{K}}(R)$ being the hyperradial part of the wavefunction and $Y_{\mathbf{K}}(\Omega_5)$ being the 6D hyperspherical harmonics described in Sec. 6.1.1. Since hyperspherical harmonics are eigenfunctions of $\hat{K}^2$ with eigenvalue $K(K+4)$, the Hamiltonian becomes

$$\hat{H}_K = -\frac{1}{2}\left[\frac{\partial^2}{\partial R^2} - \frac{K(K+4) + 15/4}{R^2}\right] + \frac{W(\Omega_5)}{R}. \tag{6.9}$$

We solve this equation using finite difference to discretize the hyperradial function $U_{\mathbf{K}}(R)$. For $W(\Omega_5) = 1$ the equation is the 6D hydrogen atom (i.e. an electron interacting with a Coulomb potential in 6 spacial dimensions, rather than the typical 3 spacial dimension) with an analytic solution that can be used to test the hyperadial portion of the code (see [222] for energy levels). The angular portion of the equations is then expanded in hyperspherical harmonics. The details of the expansion are the focus of the remainder of this section.

6.1.1 Hyperspherical harmonic definition

There are multiple ways to define hyperspherical harmonics in 6D. Since they are equivalent up to a unitary rotation, it is best to choose those that match the symmetry of the problem. In our case, we choose spherical harmonics that contain a hyperangle α that connects two-3D spaces as shown in Fig. 6.1. The 3D spaces belong to coordinates $\mathbf{r}_1$ and $\mathbf{r}_2$ with radii r_1 and r_2 respectively. These spaces will either represent a Jacobi coordinate (Sec. 6.1.2) or the space of each electron (Sec. 6.1.3). The resulting 6D spherical harmonics are given by

$$Y_{K,L,M}^{\ell_{r1},\ell_{r2}}(\Omega_5) = N_K^{\ell_{r1},\ell_{r2}} P_n^{(\ell_{r1}+1/2,\ell_{r2}+1/2)}(\cos(2\alpha)) \cos^{\ell_{r1}}(\alpha) \sin^{\ell_{r2}}(\alpha) \tag{6.10}$$

$$\times \sum_{m_{r_1},m_{r_2}} \langle L, M|\ell_{r_1}, m_{r_1}, \ell_{r_2}, m_{r_2}\rangle \left[Y_{\ell_{r_1},m_{r_1}}(\hat{r}_1) Y_{\ell_{r_2},m_{r_2}}(\hat{r}_2)\right] \tag{6.11}$$

with

$$N_K^{\ell_{r1},\ell_{r2}} = \sqrt{\frac{2(K+2)(n!)\Gamma(n+\ell_{r_1}+\ell_{r_2}+2)}{\Gamma(n+\ell_{r_1}+3/2)\Gamma(n+\ell_{r_2}++3/2)}}. \tag{6.12}$$

where $P_n^{(\alpha,\beta)}$ is the Jacobi polynomial, $\langle L, M|\ell_{r_1}, m_x, \ell_{y_1}, m_y\rangle$ is a Clebsch–Gordan coefficient (CGC), Γ is the gamma function, $Y_{\ell_r,m_r}(\hat{r})$ is the standard 3D spherical harmonics, Ω_5 is the 6D solid angle containing five angular dimensions, and $n = (K - \ell_{x_1} - \ell_{y_1})/2$. K, L, M, ℓ_{r_1} and ℓ_{r_2} are the quantum numbers with $K = 2n + \ell_{x_1} + \ell_{y_1}$ being the grand angular momentum, $\ell_{r_1} \geq 0$ and $\ell_{r_2} \geq 0$ being the angular momentum for the $\mathbf{r}_1$ and $\mathbf{r}_2$ coordinates, respectively, $|\ell_{r_1} - \ell_{r_2}| \leq L \leq \ell_{r_1} + \ell_{r_2}$ and $-L \leq M \leq L$. We define $\mathbf{K} = \{K, L, M, \ell_{r_1}, \ell_{r_2}\}$ allowing for the simplified notation $Y_{\mathbf{K}}(\Omega_5)$.

The hyperspherical harmonics contain three parts, each depending on one free parameter α, $\mathbf{r}_1$, and $\mathbf{r}_2$. By defining

$$\tilde{P}_n^{\ell_{r1},\ell_{r2}}(\alpha) = N_K^{\ell_{r1},\ell_{r2}} P_n^{(\ell_{r1}+1/2,\ell_{r2}+1/2)}(\cos(2\alpha)) \cos^{\ell_{r1}}(\alpha) \sin^{\ell_{r2}}(\alpha) \tag{6.13}$$

hyperspherical harmonics become

$$Y_{K,L,M}^{\ell_{r1},\ell_{r2}}(\Omega_5) = \tilde{P}_n^{\ell_{r1},\ell_{r2}}(\alpha) \sum_{m_{r_1},m_{r_2}} \langle L, M|\ell_{r1}, m_{r1}, \ell_{r2}, m_{r2}\rangle \left[Y_{\ell_{r_1},m_{r_1}}(\hat{r}_1) Y_{\ell_{r_2},m_{r_2}}(\hat{r}_2)\right] , \tag{6.14}$$

which highlights the three main components including the dependence of the angles in the spaces $\mathbf{r_1}$ and $\mathbf{r_2}$ as well as the dependence on the hyperangle α that couples the two spaces.

6.1.2 Jacobi coordinates

Jacobi coordinates are often used for studying many body interactions. They are defined by choosing a particle and defining a relative coordinate between the chosen particle and a second particle. The next particle is defined by a coordinate connecting the center of mass of all the previous particles to the new particle. The pattern continues until all particles have been included. The result is a set of coordinates that has dimension $3(N-1)$ assuming the exact location of the center of mass R_{cm} in space is irrelevant. For a three particle system, the center of mass is given by

$$\mathbf{R}_{cm} = \frac{m_1\mathbf{r}_1 + m_2\mathbf{r}_2 + m_3\mathbf{r}_3}{M} \tag{6.15}$$

with m_i being the mass of the ith particle, $\mathbf{r}_i$ being its spatial coordinate, and $M = \sum_{i=1}^{3} m_i$. The three convenient sets of Jacobi coordinates are

$$\mathbf{x}_1 = \left[\frac{m_2 m_3 M}{m_1(m_2+m_3)^2}\right]^{1/4} (\mathbf{r}_3 - \mathbf{r}_2); \quad \mathbf{y}_1 = \left[\frac{m_1(m_2+m_3)^2}{m_2 m_3 M}\right]^{1/4} \left(\mathbf{r}_1 - \frac{m_2\mathbf{r}_2 + m_3\mathbf{r}_3}{m_2+m_3}\right) \tag{6.16}$$

$$\mathbf{x}_2 = \left[\frac{m_3 m_1 M}{m_2(m_3+m_1)^2}\right]^{1/4} (\mathbf{r}_1 - \mathbf{r}_3); \quad \mathbf{y}_2 = \left[\frac{m_2(m_3+m_1)^2}{m_3 m_1 M}\right]^{1/4} \left(\mathbf{r}_2 - \frac{m_3\mathbf{r}_3 + m_1\mathbf{r}_1}{m_3+m_1}\right) \tag{6.17}$$

$$\mathbf{x}_3 = \left[\frac{m_1 m_2 M}{m_3(m_1+m_2)^2}\right]^{1/4} (\mathbf{r}_2 - \mathbf{r}_1); \quad \mathbf{y_3} = \left[\frac{m_3(m_1+m_2)^2}{m_1 m_2 M}\right]^{1/4} \left(\mathbf{r}_3 - \frac{m_1\mathbf{r}_1 + m_2\mathbf{r}_2}{m_1+m_2}\right). \tag{6.18}$$

The three coordinate systems are depicted in Fig. 6.2. For the Helium atom we choose the nucleus as m_1 and the two electrons as m_2 and m_3. For the rest of the section, we set $m_1 \to \infty$ and

$m_2 = m_3 = m$ such that

$$\mathbf{x}_1 = \beta_1(\mathbf{r}_3 - \mathbf{r}_2); \quad \mathbf{y}_1 = \frac{1}{\beta_1}\left(\mathbf{r}_1 - \frac{\mathbf{r}_2 + \mathbf{r}_3}{2}\right) \tag{6.19}$$

$$\mathbf{x}_2 = \beta_2(\mathbf{r}_1 - \mathbf{r}_3); \quad \mathbf{y}_2 = \frac{1}{\beta_2}\left(\mathbf{r}_2 - \frac{\mathbf{r}_3 + \mathbf{r}_1}{2}\right) \tag{6.20}$$

$$\mathbf{x}_3 = \beta_3(\mathbf{r}_2 - \mathbf{r}_1); \quad \mathbf{y}_3 = \frac{1}{\beta_3}\left(\mathbf{r}_3 - \frac{\mathbf{r}_1 + \mathbf{r}_2}{2}\right), \tag{6.21}$$

where $\beta_1 = 1/\sqrt{2}$ and $\beta_2 = \beta_3 = 1$ within the infinite mass approximation. By applying a Raynal-Revai coefficient (RRC) it is possible to transition between the three different coordinate systems. The transformation conserves the angular momentum quantum numbers K, L, and M of the hyperspherical harmonics.

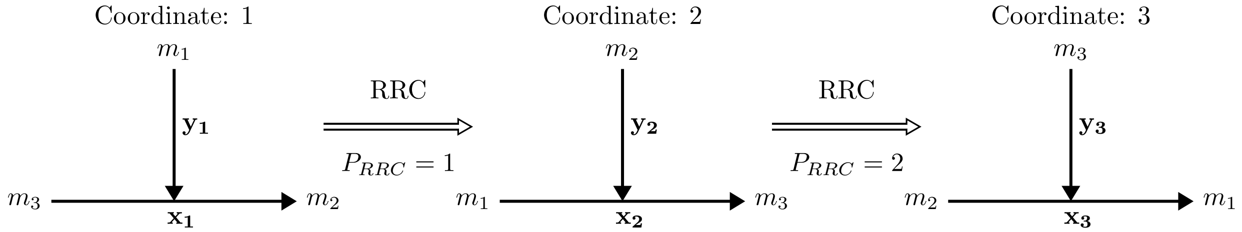

Figure 6.2: The Jacobi coordinates for three body interactions. Each coordinate can be obtained from the previous by utilizing a Raynal-Revai coefficient.

The RRCs for rotating between coordinate system i and j can be written explicitly as

$$\begin{aligned} < \ell_{x_j}, \ell_{y_j} | \ell_{x_i}, \ell_{y_i} >_{K,L} = & \frac{(-1)^{n_i+n_j}}{\sqrt{C^{n_j}_{\ell_{x_j}\ell_{y_j}} C^{n_i}_{\ell_{x_i}\ell_{y_i}}}} \sum_{\lambda_1,\lambda_2,\lambda_3,\lambda_4} i^{\lambda_2-\lambda_1+\ell_{y_i}-\ell_{y_j}} \left[\prod_{k=1}^{4}(2\lambda_k+1)\right] \\ & \times \left\langle \lambda_1 0 \lambda_3 0 \middle| \ell_{x_j} 0 \right\rangle \langle \lambda_2 0 \lambda_3 0 | \ell_{x_i} 0 \rangle \left\langle \lambda_2 0 \lambda_4 0 \middle| \ell_{y_j} 0 \right\rangle \langle \lambda_1 0 \lambda_4 0 | \ell_{y_i} 0 \rangle \\ & \times \operatorname{sgn}(a_{12})^{\lambda_1} \operatorname{sgn}(a_{21})^{\lambda_2} \operatorname{sgn}(a_{11})^{\lambda_3} \operatorname{sgn}(a_{22})^{\lambda_4} \begin{bmatrix} \lambda_3 & \lambda_1 & \ell_{x_j} \\ \lambda_2 & \lambda_4 & \ell_{y_j} \\ l_{x_i} & l_{y_i} & L \end{bmatrix} \\ & \times \sum_{\nu,\mu} (-1)^{\mu} |a_{12}|^{2\mu+\lambda_1+\lambda_2} |a_{12}|^{2\nu+\lambda_3+\lambda_4} C^{\mu}_{\lambda_1\lambda_2} C^{\nu}_{\lambda_3\lambda_4} \end{aligned} \tag{6.22}$$

where $\operatorname{sgn}(a_{ij})$ is the sign of a_{ij}, between spherical harmonics with quantum numbers $K = 2n_i + \ell_{x_i} + \ell_{y_i} = 2n_j + \ell_{x_j} + \ell_{y_j}$, the sums go over all possible combinations of $K = 2(\mu+\nu) + \lambda_1 + \lambda_2 + \lambda_3 + \lambda_4$ with

$(\lambda_i, \mu, \nu = 0, 1, 2, \cdots)$, $\langle \lambda_1 0 \lambda_3 0 | \ell_{x_j} 0 \rangle$ is a Clebsch Gordan coefficient, $\begin{bmatrix} \lambda_3 & \lambda_1 & \ell_{x_j} \\ \lambda_2 & \lambda_4 & \ell_{y_j} \\ l_{x_i} & l_{x_y} & L \end{bmatrix}$ is a Wigner 9j symbol, $C^{\mu}_{\alpha\beta} = \frac{(2\mu+\alpha+\beta+1)!}{(\mu)!(\mu+\alpha+\beta+1)!(2(\mu+\alpha)+1)!!(2(\mu+\beta)+1)!!}$, $a_{11} = \cos(\xi_{ki})$, $a_{22} = \cos(\xi_{ki})$, $a_{12} = \sin(\xi_{ki})$, and $a_{21} = -\sin(\xi_{ki})$ with $\xi_{ki} = \arctan\big((-1)^{P_{RRC}} \sqrt{M m_j/(m_i m_k)}\big)$ where m_i is the mass of the ith particle, M is the total mass and P is the number of permutations of $m_1 \to m_2 \to m_3 \to m_1$ as shown in Fig. 6.2. As the value of K increases, RRCs become extremely computationally expensive limiting the usefulness of this approach.

Utilizing the Jacobi coordinates, denoted by '1' in Fig. 6.2, the Helium potential becomes

$$V(\mathbf{R}) = \frac{1}{r_{23}} - \frac{Z}{r_{12}} - \frac{Z}{r_{13}} \tag{6.23}$$

which can be rewritten as

$$W(\Omega_5) = RV(\mathbf{R}) = \frac{1}{x_1\sqrt{2}} - \frac{Z\sqrt{2}}{|\hat{y}_1 + \hat{x}_1|} - \frac{Z\sqrt{2}}{|\hat{y}_1 - \hat{x}_1|}. \tag{6.24}$$

By using the hyperspherical harmonics defined in Eq. 6.14, with $\mathbf{r}_1 = \mathbf{x}_1$ and $\mathbf{r}_2 = \mathbf{y}_1$, the first term is easy to calculate through a 1D integral over α written explicitly below. However, the next two terms would require a 5D integral which is expensive and numerically unstable if computed directly. Instead, we will exchange particles in the coordinate system to allow the Jacobi coordinate $\mathbf{x}_i$ to correspond to the distance between the two interacting particles. The result is a 1D integral over α that is similar to the electron-electron repulsion term. To achieve this, we utilize RRC (Eq. 6.22) which allow us to write

$$Y^{\ell_{x_i},\ell_{y_i}}_{K,L,M} = \sum_{\ell_{x_j}\ell_{y_j}} < \ell_{x_j}, \ell_{y_j} | \ell_{x_i}, \ell_{y_i} >_{K,L} Y^{\ell_{x_j},\ell_{y_j}}_{K,L,M}(\Omega_{5_j}), \tag{6.25}$$

where Ω_{5_i} and Ω_{5_j} are the solid angles in the Jacobi coordinates labeled by i, j. We note that K, L and M are conserved in this rotation allowing us to remove any subscripts.

For practical reasons, we need to calculate the matrix elements $\langle \mathbf{K}' | V(R = 1, \Omega_{5_i}) | \mathbf{K} \rangle = \langle \mathbf{K}' | W(\Omega_{5_i}) | \mathbf{K} \rangle$ as the term $1/R$ can be factored out of $V(R, \Omega_{5_i})$ removing its dependence on R. We can then store the results of $\langle \mathbf{K}' | W(\Omega_{5_i}) | \mathbf{K} \rangle$ in a hash table to be looked up when building the matrix [126].

The electron-electron repulsion term of $W(\Omega_5)$ becomes

$$\left\langle K'\ell'_{x_1}\ell'_{y_1}L'M'\right| \frac{1}{\sqrt{2}\cos\alpha_1} \left|K\ell_{x_1}\ell_{y_1}LM\right\rangle = \frac{1}{\sqrt{2}}\delta_{\ell'_{x_1},\ell_{x_1}}\delta_{\ell'_{y_1},\ell_{y_1}}\delta_{L',L}\delta_{M',M} \tag{6.26}$$

$$\times \int_0^{\pi/2} \tilde{P}_{n'}^{\ell'_{x_1},\ell'_{y_1}}(\alpha_1)\tilde{P}_{n}^{\ell_{x_1},\ell_{y_1}}(\alpha_1)\sin^2(\alpha_1)\cos(\alpha_1)d\alpha_1\,, \tag{6.27}$$

where the delta functions arise from the integral over $d\omega$.

The Coulomb potential for the electron with mass m_3 in $W(\Omega_5)$ becomes

$$\left\langle K'\ell'_{x_1}\ell'_{y_1}L'M'\right| -Z\frac{R}{r_{13}} \left|K\ell_{x_1}\ell_{y_1}LM\right\rangle = \sum_{\ell_{x_2},\ell_{y_2}} <\ell_{x_2},\ell_{y_2}|\ell'_{x_1},\ell'_{x_1}>_{K',L'}<\ell_{x_2},\ell_{y_2}|\ell_{x_1},\ell_{x_1}>_{K,L} \tag{6.28}$$

$$\times \left\langle K'\ell'_{x_2}\ell'_{y_2}L'M'\right| \frac{-Z}{\cos\alpha_2} \left|K\ell_{x_2}\ell_{y_2}LM\right\rangle \tag{6.29}$$

with $P_{RRC} = 1$ and

$$\left\langle K'\ell'_{x_2}\ell'_{y_2}L'M'\right| \frac{1}{\sqrt{2}\cos\alpha_2} \left|K\ell_{x_2}\ell_{y_2}LM\right\rangle = \frac{1}{\sqrt{2}}\delta_{\ell'_{x_2},\ell_{x_2}}\delta_{\ell'_{y_2},\ell_{y_2}}\delta_{L',L}\delta_{M',M} \tag{6.30}$$

$$\times \int_0^{\pi/2} \tilde{P}_{n'}^{\ell'_{x_2},\ell'_{y_2}}(\alpha_2)\tilde{P}_{n}^{\ell_{x_2},\ell_{y_2}}(\alpha_2)\sin^2(\alpha_2)\cos(\alpha_2)d\alpha_2 \tag{6.31}$$

and the Coulomb potential for the other electron (with m_2) of $W(\Omega_5)$ becomes

$$\left\langle K'\ell'_{x_1}\ell'_{y_1}L'M'\right| -Z\frac{R}{r_{12}} \left|K\ell_{x_1}\ell_{y_1}LM\right\rangle = \sum_{\ell_{x_3},\ell_{y_3}} <\ell_{x_3},\ell_{y_3}|\ell'_{x_1},\ell'_{x_1}>_{K',L'}<\ell_{x_3},\ell_{y_3}|\ell_{x_1},\ell_{x_1}>_{K,L} \tag{6.32}$$

$$\times \left\langle K'\ell'_{x_3}\ell'_{y_3}L'M'\right| \frac{-Z}{\cos\alpha_3} \left|K\ell_{x_3}\ell_{y_3}LM\right\rangle \tag{6.33}$$

with $P_{RRC} = 2$ and

$$\left\langle K'\ell'_{x_3}\ell'_{y_3}L'M'\right| \frac{1}{\sqrt{2}\cos\alpha_3} \left|K\ell_{x_3}\ell_{y_3}LM\right\rangle = \frac{1}{\sqrt{2}}\delta_{\ell'_{x_3},\ell_{x_3}}\delta_{\ell'_{y_3},\ell_{y_3}}\delta_{L',L}\delta_{M',M} \tag{6.34}$$

$$\times \int_0^{\pi/2} \tilde{P}_{n'}^{\ell'_{x_3},\ell'_{y_3}}(\alpha_3)\tilde{P}_{n}^{\ell_{x_3},\ell_{y_3}}(\alpha_3)\sin^2(\alpha_3)\cos(\alpha_3)d\alpha_3. \tag{6.35}$$

Next, the laser potential for a linearly polarized laser aligned along the z-axis needs to be calculated. The potential term is given by

$$V_{las}(\mathbf{R}) = -E_z z_2 - E_z z_3 = -2E_z \frac{z_2 + z_3}{2}\,, \tag{6.36}$$

where z_2 and z_3 are the z-components of the two electrons and E_z is the magnitude of the z-component of the electric field. Therefore, the laser couples to the z-component of the center of mass of the two electrons namely

$$\mathbf{r}_{2e_{cm}} = \frac{\mathbf{r}_2 + \mathbf{r}_3}{2}. \tag{6.37}$$

Noticing that y_1 from Eq. 6.16 contains $\mathbf{r}_{2e_{cm}}$, the laser term only appears in the $\hat{y}_1$ spherical harmonics. Next, we need to calculate the $V_{las}(\mathbf{R})$ matrix element as

$$\left\langle K'\ell'_{x_1}\ell'_{y_1}L'M'\right| -2E_z z_{2e_{cm}} \left|K\ell_{x_1}\ell_{y_1}LM\right\rangle. \tag{6.38}$$

In the infinite mass approximation, $\mathbf{R}_{cm} = \mathbf{y}_1$ and therefore

$$\begin{aligned} z_{2e_{cm}} &= \beta_1 \mathbf{y}_1 \cdot \hat{z}_{cm} && (6.39)\\ &= \frac{y_1 \cos(\theta_{y_1})}{\sqrt{2}} && (6.40)\\ &= 2\sqrt{\frac{\pi}{6}} y_1 Y_{1,0}(\hat{y}_1) && (6.41)\\ &= 2\sqrt{\frac{\pi}{6}} Rsin(\alpha_1) Y_{1,0}(\hat{y}_1) && (6.42) \end{aligned}$$

Using this in Eq. 6.38 we obtain

$$\begin{aligned} &\left\langle K'\ell'_{x_1}\ell'_{y_1}L'M'\right| -2E_z z_{2e_{cm}} \left|K\ell_{x_1}\ell_{y_1}LM\right\rangle && (6.43)\\ &\quad = -2E_z \left\langle K'\ell'_{x_1}\ell'_{y_1}L'M'\right| 2\sqrt{\frac{\pi}{6}} Rsin(\alpha_1) Y_{1,0}(\hat{y}_1) \left|K\ell_{x_1}\ell_{y_1}LM\right\rangle \end{aligned}$$

which becomes

$$\begin{aligned}
&\left\langle K'\ell'_{x_1}\ell'_{y_1}L'M'\right| -2E_z z_{2e_{cm}} \left|K\ell_{x_1}\ell_{y_1}LM\right\rangle \\
&\qquad= -2E_z\delta_{\ell'_{x_1}\ell_{x_1}}\delta_{M'M}R\sqrt{\frac{(2\ell'_{y_1}+1)}{2(2\ell_{y_1}+1)}} \\
&\qquad\times\left[\int_0^{\pi/2}\tilde{P}_{n'}^{\ell'_{x_1},\ell'_{y_1}}(\alpha_1)\tilde{P}_{n}^{\ell_{x_1},\ell_{y_1}}(\alpha_1)\sin^3(\alpha_1)\cos^2(\alpha_1)d\alpha_1\right] \\
&\qquad\times\sum_{m'_x,m'_y,m_x,m_y}\Big[\left\langle\ell'_{y_1},0,1,0\middle|\ell_{y_1},0\right\rangle\left\langle\ell'_{y_1},m'_y,1,0\middle|\ell_{y_1},m_y\right\rangle \\
&\qquad\times\left\langle\ell'_{x_1},m'_x,\ell'_{y_1},m'_y\middle|L',M'\right\rangle\left\langle\ell_{x_1},m_x,\ell_{y_1},m_y\middle|L,M\right\rangle\Big]
\end{aligned} \tag{6.44}$$

Since the M quantum number does not change and $M = 0$ for the ground state of helium atom, the sum over m'_x, m'_y, m_x, m_y simplifies to a single sum over $-\min(L', L) \leq m \leq \min(L', L)$ with $m'_x = m_x = -m$ and $m'_y = m_y = m$ as we get $\delta_{m'_y,m_y}$ from the second CGC, $\delta_{m'_x,-m'_y}$ (when $M' = 0$) from the third CGC, and $\delta_{m_x,-m_y}$ (when $M = 0$) from the forth CGC. If $M \neq 0$ is needed, a different simplification is required.

6.1.3 Electronic coordinates

To remove the need for RRCs due to their numerical complexity for high K values, we will use the nucleus as the origin and label the coordinates from the proton to the i-th electron as $\mathbf{r}_i$ where $i = 1, 2$. Therefore, we have

$$r_1 = R\cos(\alpha) \tag{6.45}$$

$$r_2 = R\sin(\alpha) \tag{6.46}$$

and a solid angle

$$d\Omega_5 = \cos^2(\alpha)\sin^2(\alpha)d\alpha d\omega_{r_1}d\omega_{r_2}. \tag{6.47}$$

We will use spherical harmonics with labels $Y^{\ell_{r_1},\ell_{r_2}}_{K,L,M}(\Omega_5)$ where ℓ_{r_i} is the spherical harmonic for the 3D space coordinate $\mathbf{r}_i$. The electron-nucleus terms take the form $-Z/r_i$ and the matrix elements become

$$-\left\langle\Psi'\right|\frac{Z}{r_1}\left|\Psi\right\rangle = -\frac{Z}{R}\delta_{L',L}\delta_{M',M}\delta_{\ell'_{r_1},\ell_{r_1}}\delta_{\ell'_{r_2},\ell_{r_2}}\int\limits_0^{\pi/2}\tilde{P}_{n'}^{\ell'_{r_1},\ell'_{r_2}}(\alpha)\tilde{P}_{n}^{\ell_{r_1},\ell_{r_2}}(\alpha)\sin^2(\alpha)\cos(\alpha)d\alpha \tag{6.48}$$

and

$$-\left\langle\Psi'\right|\frac{Z}{r_2}\left|\Psi\right\rangle = -\frac{Z}{R}\delta_{L',L}\delta_{M',M}\delta_{\ell'_{r_1},\ell_{r_1}}\delta_{\ell'_{r_2},\ell_{r_2}}\int\limits_0^{\pi/2}\tilde{P}_{n'}^{\ell'_{r_1},\ell'_{r_2}}(\alpha)\tilde{P}_{n}^{\ell_{r_1},\ell_{r_2}}(\alpha)\sin(\alpha)\cos^2(\alpha)d\alpha. \tag{6.49}$$

Note that the term $1/R$ can be factored out allowing the integral over α to be performed once and stored in a lookup table to improve computational performance.

The electron-electron term is less straight forward. We start by using

$$\frac{1}{|\mathbf{r}_1-\mathbf{r}_2|} = \sum_{\ell=0}^{\infty}\sum_{m=-\ell}^{\ell}\frac{4\pi}{2\ell+1}\frac{r_<^{\ell}}{r_>^{\ell+1}}Y^*_{\ell,m}(\hat{\mathbf{r}}_2)Y_{\ell,m}(\hat{\mathbf{r}}_1) \tag{6.50}$$

and then after some extensive algebraic work we obtain

$$\left\langle\Psi'\right|\frac{1}{|\mathbf{r}_1-\mathbf{r}_2|}\left|\Psi\right\rangle = \frac{\delta_{L',L}\delta_{M',M}}{R}\sqrt{\frac{(2\ell'_{r_1}+1)(2\ell'_{r_2}+1)}{(2\ell_{r_1}+1)(2\ell_{r_2}+1)}} \tag{6.51}$$

$$\times\sum_{\ell=max(|\ell_{r_1}-\ell_{r_2}|,|\ell'_{r_1}-\ell'_{r_2}|)}^{min(|\ell_{r_1}+\ell_{r_2}|,|\ell'_{r_1}+\ell'_{r_2}|)}\left\langle\ell'_{r_1},0,\ell,0\middle|\ell_{r_1},0\right\rangle\left\langle\ell'_{r_2},0,\ell,0\middle|\ell_{r_2},0\right\rangle \tag{6.52}$$

$$\times\left[\int\limits_0^{\pi/4}\tilde{P}_{n'}^{\ell'_{r_1},\ell'_{r_2}}(\alpha)\tilde{P}_{n}^{\ell_{r_1},\ell_{r_2}}(\alpha)\frac{\sin^{\ell+2}(\alpha)}{\cos^{\ell-1}(\alpha)}d\alpha+\int\limits_{\pi/4}^{\pi/2}\tilde{P}_{n'}^{\ell'_{r_1},\ell'_{r_2}}(\alpha)\tilde{P}_{n}^{\ell_{r_1},\ell_{r_2}}(\alpha)\frac{\cos^{\ell+2}(\alpha)}{\sin^{\ell-1}(\alpha)}d\alpha\right] \tag{6.53}$$

$$\times\sum_{m'_{r_1}=-\ell'_{r_1},m'_{r_2}=M'-m'_{r_1}}^{\ell'_{r_1}}\left\langle L',M'\middle|\ell'_{r_1},m'_{r_1},\ell'_{r_2},m'_{r_2}\right\rangle \tag{6.54}$$

$$\times\sum_{m_{r_1}=-\ell_{r_1},m_{r_2}=M-m_{r_1},m=m_{r_1}-m'_{r_1}}^{\ell_{r_1}}(-1)^m\left\langle L,M|\ell_{r_1},m_{r_1},\ell_{r_2},m_{r_2}\right\rangle \tag{6.55}$$

$$\times\left\langle\ell'_{r_1},m'_{r_1},\ell,m\middle|\ell_{r_1},m_{r_1}\right\rangle\left\langle\ell'_{r_2},m'_{r_2},\ell,m\middle|\ell_{r_2},m_{r_2}\right\rangle\,. \tag{6.56}$$

Note the requirement for the last row gives $m = m_{r_1} - m'_{r_1}$ and $m = m'_{r_2} - m_{r_2}$ which gives the delta function $\delta_{M',M}$ as well.

Finally, we need the laser operator

$$V_{las}(\mathbf{R}) = -E_z z_{r_1} - E_z z_{r_2}. \tag{6.57}$$

Since each electron has its own 3D space, it is easier to calculate the laser operator for each electron independently. It is then convenient to define

$$V_{las}(\mathbf{r}_1) = -E_z z_{r_1} = -2E_z z_{r_2}\sqrt{\frac{\pi}{3}}R\sin(\alpha_1)Y_{1,0}(\hat{r}_1), \tag{6.58}$$

$$V_{las}(\mathbf{r}_2) = -E_z z_{r_2} = -2E_z z_{r_2}\sqrt{\frac{\pi}{3}}R\sin(\alpha_1)Y_{1,0}(\hat{r}_2), \tag{6.59}$$

$$V_{las}(\mathbf{R}) = V_{las}(\mathbf{r}_1) + V_{las}(\mathbf{r}_2). \tag{6.60}$$

The resulting matrix elements are

$$\left\langle\Psi'\right| V_{las}(\mathbf{r}_1)\left|\Psi\right\rangle = -E_z R\sqrt{\frac{(2\ell'_{r_1}+1)}{(2\ell_{r_1}+1)}}\delta_{L',L\pm1}\delta_{M',M}\delta_{\ell'_{r_1},\ell_{r_1}\pm1}\delta_{\ell'_{r_2},\ell_{r_2}}\left\langle\ell'_{r_1},0,1,0\middle|\ell_{r_1},0\right\rangle \tag{6.61}$$

$$\times\int\limits_0^{\pi/2}\tilde{P}_{n'}^{\ell'_{r_1},\ell'_{r_2}}(\alpha)\tilde{P}_n^{\ell_{r_1},\ell_{r_2}}(\alpha)\sin^3(\alpha)\cos^2(\alpha)d\alpha \tag{6.62}$$

$$\times\sum_{m_r=-\min\left[l'_{r_1},l_{r_1},l'_{r_2},l_{r_2}\right]}^{\min\left[l'_{r_1},l_{r_1},l'_{r_2},l_{r_2}\right]}\left\langle\ell'_{r_1},m_r,1,0\middle|\ell_{r_1},m_r\right\rangle \tag{6.63}$$

$$\times\left\langle L',M\middle|\ell'_{r_1},m_r,\ell_{r_2},-m_r\right\rangle\left\langle L,M|\ell_{r_1},m_r,\ell_{r_2},-m_r\right\rangle \tag{6.64}$$

and

$$\left\langle\Psi'\right| V_{las}(\mathbf{r}_2)\left|\Psi\right\rangle = -E_z R\sqrt{\frac{(2\ell'_{r_2}+1)}{(2\ell_{r_2}+1)}}\delta_{L',L\pm1}\delta_{M',M}\delta_{\ell'_{r_1},\ell_{r_1}}\delta_{\ell'_{r_2},\ell_{r_2}\pm1}\left\langle\ell'_{r_2},0,1,0\middle|\ell_{r_2},0\right\rangle \tag{6.65}$$

$$\times\int\limits_0^{\pi/2}\tilde{P}_{n'}^{\ell'_{r_1},\ell'_{r_2}}(\alpha)\tilde{P}_n^{\ell_{r_1},\ell_{r_2}}(\alpha)\sin^3(\alpha)\cos^2(\alpha)d\alpha \tag{6.66}$$

$$\times\sum_{m_r=-\min\left[l'_{r_1},l_{r_1},l'_{r_2},l_{r_2}\right]}^{\min\left[l'_{r_1},l_{r_1},l'_{r_2},l_{r_2}\right]}\left\langle\ell'_{r_2},m_r,1,0\middle|\ell_{r_2},m_r\right\rangle \tag{6.67}$$

$$\times\left\langle L',M\middle|\ell_{r_1},m_r,\ell'_{r_2},-m_r\right\rangle\left\langle L,M|\ell_{r_1},m_r,\ell_{r_2},-m_r\right\rangle. \tag{6.68}$$

In this derivation, we used $M = 0$ therefore $m_{r_1} = -m_{r_2}$. For $M \neq 0$ adjustments to the sum are needed.

6.2 Implementation and first tests

The RRC and non-RRC methods were both implemented in the same code, based on the SAE-TDSE method. This allows for two electron calculations to be performed by simply changing a few parameters in an input file.

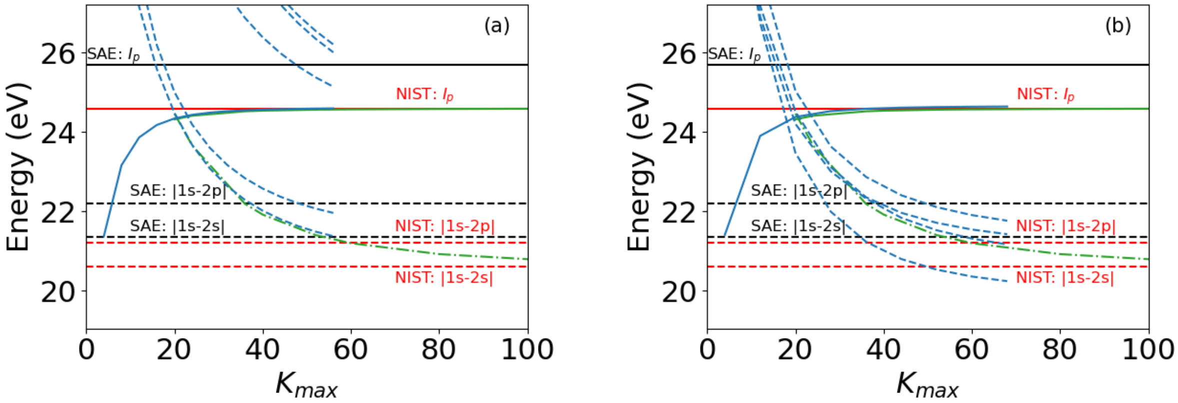

Figure 6.3: Convergence of He atom first ionization potential (blue solid line) and excited states (blue dashed line) with RRC (left) and non-RRC (right) methods. Reference lines for He-SAE (black), NIST energies (red), and literature convergence (green, [126]) are shown.

To ensure the code is working properly, we have ran test on the convergences of the ionization potential and low lying bound states shown in Fig. 6.3. Panel (a) shows the convergence of the RRC method in blue as a function of the grand angular momentum using second order finite difference with a grid spacing of 0.05 au. The convergence is in good agreement with the green lines from a similar code [126]. Additionally, the NIST (red) and SAE potential (black) energy levels are shown. Panel (b) shows the same data for the non-RRC method shown in blue. The non-RRC method has more low lying bound states that are due to not separating out the eigenstates with two spin up electrons. Taking account of it will reduce the runtime of the non-RRC method. As one can see, both methods produce highly accurate bound states quite quickly. The excited states, however, are slow to converge only outperforming the DFT based SAE potential energy levels with $K_{max} > 48$. As K_{max} increases the matrix elements become increasingly difficult to calculate and the size of the wavefunction grows rapidly. This greatly limits the usefulness of this method for two electron calculations without the use of supercomputing resources.

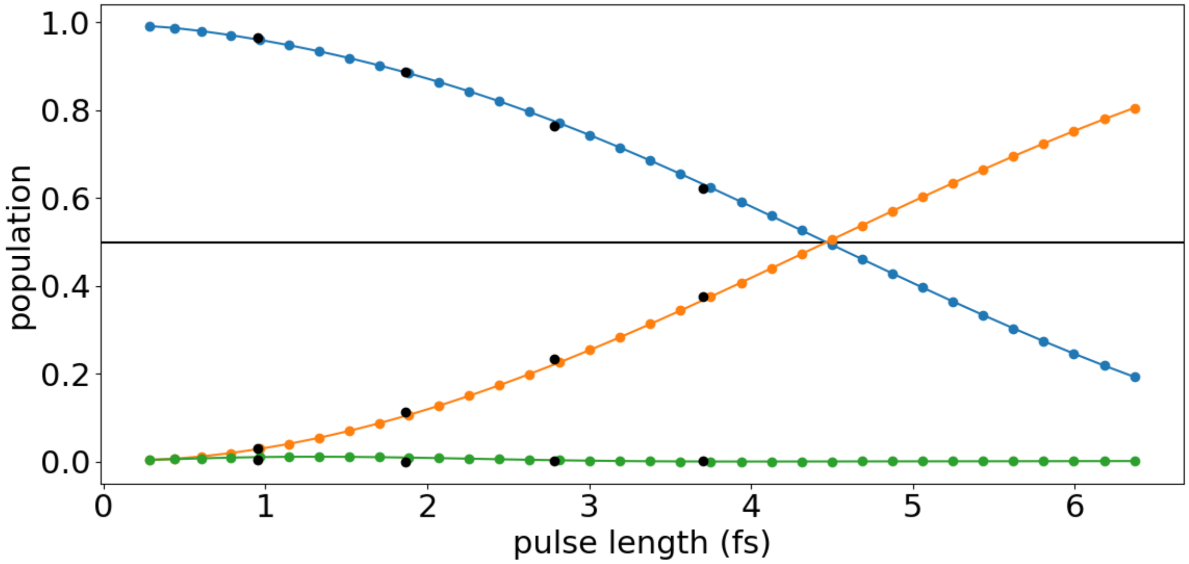

Figure 6.4: Rabi flopping between the $1s$ and $2p$ states in helium atom. The populations in the $1s$ (blue), $2p$ (orange), and all other states (green) for the SAE code are plotted. The black dots show the two electrons simulations using the RRC method with $K_{max} = 48$ agree well with the SAE results.

To test the stability and accuracy of the time propagation linearly polarized laser field, the RRC code was used to preform a $1s-2p$ Rabi flopping with $K_{max} = 48$ to closely match the $1s-2p$ energy gap to the SAE potential. The laser pulse had a sine squared envelope, peak intensity of 10^{14} W/cm^2, resonant central frequency of 0.812 au (0.822 au) for the SAE (RRC) code with varying pulse lengths ranging from 1 to 34 cycles. Fig. 6.4 shows the SAE populations in the $1s$ (blue), $2p$ (orange), and all other bound/continuum states (green) for reference. The two electron populations are shown in black. The agreement is quite good, and the small discrepancy are due to slightly different energy gaps.

6.3 Outlook

The present methods still require improvement in order to perform converged two active electron simulations on desktop systems. Switching from the RRC to the non-RRC method lead to orders of magnitude reduction in runtime for matrix generation. However, the need to perform numerical integrals of Jacobi polynomials largely slows down the computation. Additionally, the slow convergence of excited states with respect to the grand angular momentum leads to large wavefuctions. If the hyperangle α is discretized using finite difference, the integrals become integrals over delta functions and the slow convergence with respect to the grand angular momentum (K) may be avoided.

Chapter 7

Summary

This thesis covers theoretical approaches to understand ultrafast processes in photoionization, Rydberg state excitation, and electron correlation. In the first two chapters, an introduction to ultrafast and strong-field physics was given with a review of relevant experimental and theoretical studies. The numerical and analytical methods that are used in this thesis were covered in Chap. 3, including original studies using RBFs to solve the time independent Schrödinger equation (Sec. 3.3.3) and a frequency correction to ultrashort laser pulses (Sec. 3.6).

The focus was then turned to developing a method of imaging ultrafast electron wavepacket dynamics using few photon ionization in Chap. 4. The extreme bandwidth of ultrafast pulses allows for processes involving different numbers of photons from the same pulse to interfere. The impacts on ionization of a helium atom were studied in Sec. 4.1 including the effects of pulse variations present in experiment. Sec. 4.2 extends the typical forward backward ionization asymmetry from ground states to the ionization of wavepackets in superposition with different m quantum numbers. To this end, we presented a novel set of generalized asymmetry parameters (GAP) to study the interference of the ground and excited state ionization signals. Finally, a method for reconstructing wavepackets undergoing attosecond electron motion using perturbation theory was presented in Sec. 4.3. The impact of shot to shot variations and the laser parameter regime required for a quality reconstruction have been analyzed.

Next, Chap. 5 covers the excitation of Rydberg states by intense IR laser pulses. Linear polarization results, in Sec. 5.1, show that the ℓ quantum number of the populated states has the same parity as the sum of the number of photons involved in the process and the ground states ℓ quantum number. The FID signals present in the HHG spectrum allows for experimental verification of this effect. Sec. 5.2 extended this study to bi-circular driving laser pulses, including an analysis of the pathways to available resonances and the occurence of high order Raman transitions which have been further studied in a project led by another graduate student [77].

Finally, we turned to the development and first tests of a fully correlated two electron code in Chap. 6. We used hyperspherical harmonics to reduce the number of radii that must be discretized from two to one. The code produces ground and excited state energies consistent with experimental results and has produced a Rabi flop between the $1s$ and the $2p$ state in He that matches our SAE codes. Future development may allow for fully correlated two electron calculations to be performed efficiently on desktop computers opening the door for more in depth studies of time dependent multi-electron effects in ultrafast physics.

Bibliography

[1] Mahmoud Abu-samha and Lars Bojer Madsen. Probing atomic and molecular targets by intense bicircular counter-rotating laser fields. Journal of Physics B: Atomic, Molecular and Optical Physics, 51(13):135401, 2018.

[2] Mahmoud Abu-samha and Lars Bojer Madsen. Pulse-length effects in strong-field ionization of atoms by co-rotating and counter-rotating bicircular laser pulses. Phys. Rev. A, 100:043415, 2019.

[3] P. Agostini, P. Breger, A. L'Huillier, H. G. Muller, G. Petite, A. Antonetti, and A. Migus. Giant stark shifts in multiphoton ionization. Phys. Rev. Lett., 63:2208–2211, 1989.

[4] P. Agostini, F. Fabre, G. Mainfray, G. Petite, and N. K. Rahman. Free-free transitions following six-photon ionization of xenon atoms. Phys. Rev. Lett., 42:1127–1130, 1979.

[5] D. Akoury, K. Kreidi, T. Jahnke, Th. Weber, A. Staudte, M. Schöffler, N. Neumann, J. Titze, L. Ph. H. Schmidt, A. Czasch, O. Jagutzki, R. A. Costa Fraga, R. E. Grisenti, R. Díez Muiño, N. A. Cherepkov, S. K. Semenov, P. Ranitovic, C. L. Cocke, T. Osipov, H. Adaniya, J. C. Thompson, M. H. Prior, A. Belkacem, A. L. Landers, H. Schmidt-Böcking, and R. Dörner. The simplest double slit: Interference and entanglement in double photoionization of h2. Science, 318(5852):949–952, 2007.

[6] Diego G. Arbó, Konstantinos I. Dimitriou, Emil Persson, and Joachim Burgdörfer. Sub-poissonian angular momentum distribution near threshold in atomic ionization by short laser pulses. Phys. Rev. A, 78:013406, 2008.

[7] David Ayuso, Piero Decleva, Serguei Patchkovskii, and Olga Smirnova. Chiral dichroism in bi-elliptical high-order harmonic generation. Journal of Physics B: Atomic, Molecular and Optical Physics, 51(6):06LT01, 2018.

[8] Satish Balay, Shrirang Abhyankar, Mark F. Adams, Jed Brown, Peter Brune, Kris Buschelman, Lisandro Dalcin, Victor Eijkhout, William D. Gropp, Dinesh Kaushik, Matthew G. Knepley, Lois Curfman McInnes, Karl Rupp, Barry F. Smith, Stefano Zampini, Hong Zhang, and Hong Zhang. PETSc users manual. Technical Report ANL-95/11 - Revision 3.7, Argonne National Laboratory, 2016.

[9] Satish Balay, William D. Gropp, Lois Curfman McInnes, and Barry F. Smith. Efficient management of parallelism in object oriented numerical software libraries. In E. Arge, A. M. Bruaset, and H. P. Langtangen, editors, Modern Software Tools in Scientific Computing, pages 163–202. Birkhäuser Press, 1997.

[10] André D Bandrauk, François Mauger, and Kai-Jun Yuan. Circularly polarized harmonic generation by intense bicircular laser pulses: electron recollision dynamics and frequency dependent helicity. Journal of Physics B: Atomic, Molecular and Optical Physics, 49(23):23LT01, 2016.

[11] Lou Barreau, C. Leon M. Petersson, Markus Klinker, Antoine Camper, Carlos Marante, Timothy Gorman, Dietrich Kiesewetter, Luca Argenti, Pierre Agostini, Jesús González-Vázquez, Pascal Salières, Louis F. DiMauro, and Fernando Martín. Disentangling spectral phases of interfering autoionizing states from attosecond interferometric measurements. Phys. Rev. Lett., 122:253203, 2019.

[12] Lou Barreau, Kévin Veyrinas, Vincent Gruson, Sébastien J. Weber, Thierry Auguste, Jean-François Hergott, Fabien Lepetit, Bertrand Carré, Jean-Christophe Houver, Danielle Dowek, and Pascal Salières. Evidence of depolarization and ellipticity of high harmonics driven by ultrashort bichromatic circularly polarized fields. Nature Communications, 9(1):4727, 2018.

[13] Ingo Barth and Manfred Lein. Numerical verification of the theory of nonadiabatic tunnel ionization in strong circularly polarized laser fields. Journal of Physics B: Atomic, Molecular and Optical Physics, 47(20):204016, 2014.

[14] Ingo Barth and Olga Smirnova. Nonadiabatic tunneling in circularly polarized laser fields: Physical picture and calculations. Phys. Rev. A, 84:063415, 2011.

[15] Ingo Barth and Olga Smirnova. Nonadiabatic tunneling in circularly polarized laser fields. ii. derivation of formulas. Phys. Rev. A, 87:013433, 2013.

[16] Jarosław H. Bauer, Francisca Mota-Furtado, Patrick F. O'Mahony, Bernard Piraux, and Krzysztof Warda. Ionization and excitation of the excited hydrogen atom in strong circularly polarized laser fields. Phys. Rev. A, 90:063402, 2014.

[17] Denitsa Baykusheva, Md Sabbir Ahsan, Nan Lin, and Hans Jakob Wörner. Bicircular high-harmonic spectroscopy reveals dynamical symmetries of atoms and molecules. Phys. Rev. Lett., 116:123001, 2016.

[18] Denitsa Baykusheva, Simon Brennecke, Manfred Lein, and Hans Jakob Wörner. Signatures of electronic structure in bicircular high-harmonic spectroscopy. Phys. Rev. Lett., 119:203201, 2017.

[19] S. Beaulieu, S. Camp, D. Descamps, A. Comby, V. Wanie, S. Petit, F. Légaré, K. J. Schafer, M. B. Gaarde, F. Catoire, and Y. Mairesse. Role of excited states in high-order harmonic generation. Phys. Rev. Lett., 117:203001, 2016.

[20] Annelise R. Beck, Birgitta Bernhardt, Erika R. Warrick, Mengxi Wu, Shaohao Chen, Mette B. Gaarde, Kenneth J. Schafer, Daniel M. Neumark, and Stephen R. Leone. Attosecond transient absorption probing of electronic superpositions of bound states in neon: detection of quantum beats. New Journal of Physics, 16(11):113016, 2014.

[21] Shuai Ben, Pei-Ying Guo, Xue-Fei Pan, Tong-Tong Xu, Kai-Li Song, and Xue-Shen Liu. Recollision induced excitation-ionization with counter-rotating two-color circularly polarized laser field. Chemical Physics Letters, 679:38 – 44, 2017.

[22] S. Bengtsson, E. W. Larsen, D. Kroon, S. Camp, M. Miranda, C. L. Arnold, A. L'Huillier, K. J. Schafer, M. B. Gaarde, L. Rippe, and J. Mauritsson. Space–time control of free induction decay in the extreme ultraviolet. Nature Photonics, 11(4):252–258, 2017.

[23] Xue-Bin Bian and André D. Bandrauk. Multichannel molecular high-order harmonic generation from asymmetric diatomic molecules. Phys. Rev. Lett., 105:093903, 2010.

[24] Christer Z. Bisgaard and Lars Bojer Madsen. Tunneling ionization of atoms. American Journal of Physics, 72(2):249–254, 2004.

[25] Diego I. R. Boll, Omar A. Fojón, C. W. McCurdy, and Alicia Palacios. Angularly resolved two-photon above-threshold ionization of helium. Physical Review A, 99(2):023416, 2019.

[26] N. Böwering, T. Lischke, B. Schmidtke, N. Müller, T. Khalil, and U. Heinzmann. Asymmetry in Photoelectron Emission from Chiral Molecules Induced by Circularly Polarized Light. Physical Review Letters, 86(7):1187–1190, 2001.

[27] Timm Bredtmann, Szczepan Chelkowski, André D. Bandrauk, and Misha Ivanov. Xuv lasing during strong-field-assisted transient absorption in molecules. Phys. Rev. A, 93:021402, 2016.

[28] Gabriela Buica. Circular dichroism in angular distribution of electron-hydrogen scattering in a two-color bicircular laser field. Phys. Rev. A, 98:053427, 2018.

[29] M. Busuladžić, A. Gazibegović-Busuladžić, and D. B. Milošević. Strong-field ionization of homonuclear diatomic molecules by a bicircular laser field: Rotational and reflection symmetries. Phys. Rev. A, 95:033411, 2017.

[30] M. Busuladžić, A. Čerkić, A. Gazibegović-Busuladžić, E. Hasović, and D. B. Milošević. Molecular-orientation-dependent interference and plateau structures in strong-field ionization of a diatomic molecule by a corotating bichromatic elliptically polarized laser field. Phys. Rev. A, 98:013413, 2018.

[31] Francesca Calegari, Giuseppe Sansone, Salvatore Stagira, Caterina Vozzi, and Mauro Nisoli. Advances in attosecond science. Journal of Physics B: Atomic, Molecular and Optical Physics, 49(6):062001, 2016.

[32] Seth Camp, Kenneth J. Schafer, and Mette B. Gaarde. Interplay between resonant enhancement and quantum path dynamics in harmonic generation in helium. Phys. Rev. A, 92:013404, 2015.

[33] Thomas A. Carlson and Manfred O. Krause. Electron shake-off resulting from k-shell ionization in neon measured as a function of photoelectron velocity. Phys. Rev., 140:A1057–A1064, 1965.

[34] A. L. Cavalieri, N. Müller, Th Uphues, V. S. Yakovlev, A. Baltuška, B. Horvath, B. Schmidt, L. Blümel, R. Holzwarth, S. Hendel, M. Drescher, U. Kleineberg, P. M. Echenique, R. Kienberger, F. Krausz, and U. Heinzmann. Attosecond spectroscopy in condensed matter. Nature, 449(7165):1029–1032, 2007.

[35] Szczepan Chelkowski and André D. Bandrauk. Sensitivity of spatial photoelectron distributions to the absolute phase of an ultrashort intense laser pulse. Physical Review A, 65(6):061802, 2002.

[36] Cong Chen, Zhensheng Tao, Carlos Hernández-García, Piotr Matyba, Adra Carr, Ronny Knut, Ofer Kfir, Dimitry Zusin, Christian Gentry, Patrik Grychtol, Oren Cohen, Luis Plaja, Andreas Becker, Agnieszka Jaron-Becker, Henry Kapteyn, and Margaret Murnane. Tomographic reconstruction of circularly polarized high-harmonic fields: 3d attosecond metrology. Science Advances, 2(2), 2016.

[37] Ming-Chang Chen, Christopher Mancuso, Carlos Hernández-García, Franklin Dollar, Ben Galloway, Dimitar Popmintchev, Pei-Chi Huang, Barry Walker, Luis Plaja, Agnieszka A. Jaroń-Becker, Andreas Becker, Margaret M. Murnane, Henry C. Kapteyn, and Tenio Popmintchev. Generation of bright isolated attosecond soft X-ray pulses driven by multicycle midinfrared lasers. Proceedings of the National Academy of Sciences, 111(23):E2361–E2367, 2014.

[38] Michael Chini, Kun Zhao, and Zenghu Chang. The generation, characterization and applications of broadband isolated attosecond pulses. Nature Photonics, 8(3):178–186, 2014.

[39] Claudio Cirelli, Carlos Marante, Sebastian Heuser, C. L. M. Petersson, Álvaro Jiménez Galán, Luca Argenti, Shiyang Zhong, David Busto, Marcus Isinger, Saikat Nandi, Sylvain Maclot, Linnea Rading, Per Johnsson, Mathieu Gisselbrecht, Matteo Lucchini, Lukas Gallmann, J. Marcus Dahlström, Eva Lindroth, Anne L'Huillier, Fernando Martín, and Ursula Keller. Anisotropic photoemission time delays close to a Fano resonance. Nature Communications, 9(1):1–9, 2018.

[40] P. B. Corkum. Plasma perspective on strong field multiphoton ionization. Phys. Rev. Lett., 71:1994–1997, 1993.

[41] E Cormier and P Lambropoulos. Optimal gauge and gauge invariance in non-perturbative time-dependent calculation of above-threshold ionization. Journal of Physics B: Atomic, Molecular and Optical Physics, 29(9):1667–1680, 1996.

[42] M. P. de Boer and H. G. Muller. Observation of large populations in excited states after short-pulse multiphoton ionization. Phys. Rev. Lett., 68:2747–2750, 1992.

[43] Gopal Dixit, Álvaro Jiménez-Galán, Lukas Medišauskas, and Misha Ivanov. Control of the helicity of high-order harmonic radiation using bichromatic circularly polarized laser fields. Phys. Rev. A, 98:053402, 2018.

[44] J. M. Ngoko Djiokap, A. V. Meremianin, N. L. Manakov, S. X. Hu, L. B. Madsen, and Anthony F. Starace. Kinematical vortices in double photoionization of helium by attosecond pulses. Phys. Rev. A, 96:013405, 2017.

[45] V. K. Dolmatov, A. S. Kheifets, P. C. Deshmukh, and S. T. Manson. Attosecond time delay in the photoionization of mn in the region of the $3p \to 3d$ giant resonance. Phys. Rev. A, 91:053415, 2015.

[46] Kevin M. Dorney, Jennifer L. Ellis, Carlos Hernández-García, Daniel D. Hickstein, Christopher A. Mancuso, Nathan Brooks, Tingting Fan, Guangyu Fan, Dmitriy Zusin, Christian Gentry, Patrik Grychtol, Henry C. Kapteyn, and Margaret M. Murnane. Helicity-selective enhancement and polarization control of attosecond high harmonic waveforms driven by bichromatic circularly polarized laser fields. Phys. Rev. Lett., 119:063201, 2017.

[47] Nicolas Douguet, Alexei N. Grum-Grzhimailo, Elena V. Gryzlova, Ekaterina I. Staroselskaya, Joel Venzke, and Klaus Bartschat. Photoelectron angular distributions in bichromatic atomic ionization induced by circularly polarized VUV femtosecond pulses. Physical Review A, 93(3):033402, 2016.

[48] Charles G. Durfee, Sterling Backus, Henry C. Kapteyn, and Margaret M. Murnane. Intense 8-fs pulse generation in the deep ultraviolet. Opt. Lett., 24(10):697–699, 1999.

[49] S. Eckart, K. Fehre, N. Eicke, A. Hartung, J. Rist, D. Trabert, N. Strenger, A. Pier, L. Ph. H. Schmidt, T. Jahnke, M. S. Schöffler, M. Lein, M. Kunitski, and R. Dörner. Direct experimental access to the nonadiabatic initial momentum offset upon tunnel ionization. Phys. Rev. Lett., 121:163202, 2018.

[50] S. Eckart, M. Kunitski, I. Ivanov, M. Richter, K. Fehre, A. Hartung, J. Rist, K. Henrichs, D. Trabert, N. Schlott, L. Ph. H. Schmidt, T. Jahnke, M. S. Schöffler, A. Kheifets, and R. Dörner. Subcycle interference upon tunnel ionization by counter-rotating two-color fields. Phys. Rev. A, 97:041402, 2018.

[51] S. Eckart, M. Richter, M. Kunitski, A. Hartung, J. Rist, K. Henrichs, N. Schlott, H. Kang, T. Bauer, H. Sann, L. Ph. H. Schmidt, M. Schöffler, T. Jahnke, and R. Dörner. Nonsequential double ionization by counterrotating circularly polarized two-color laser fields. Phys. Rev. Lett., 117:133202, 2016.

[52] Sebastian Eckart, Maksim Kunitski, Martin Richter, Alexander Hartung, Jonas Rist, Florian Trinter, Kilian Fehre, Nikolai Schlott, Kevin Henrichs, Lothar Ph. H. Schmidt, Till Jahnke, Markus Schöffler, Kunlong Liu, Ingo Barth, Jivesh Kaushal, Felipe Morales, Misha Ivanov, Olga Smirnova, and Reinhard Dörner. Ultrafast preparation and detection of ring currents in single atoms. Nature Physics, 14(7):701–704, 2018.

[53] H. Eichmann, A. Egbert, S. Nolte, C. Momma, B. Wellegehausen, W. Becker, S. Long, and J. K. McIver. Polarization-dependent high-order two-color mixing. Phys. Rev. A, 51:R3414–R3417, 1995.

[54] U. Eichmann, A. Saenz, S. Eilzer, T. Nubbemeyer, and W. Sandner. Observing Rydberg atoms to survive intense laser fields. Phys. Rev. Lett., 110:203002, 2013.

[55] Nicolas Eicke and Manfred Lein. Attoclock with counter-rotating bicircular laser fields. Phys. Rev. A, 99:031402, 2019.

[56] A. Einstein. Über einen die Erzeugung und Verwandlung des Lichtes betreffenden heuristischen Gesichtspunkt. Annalen der Physik, 322(6):132–148, 1905.

[57] F H M Faisal. Multiple absorption of laser photons by atoms. Journal of Physics B: Atomic and Molecular Physics, 6(4):L89–L92, 1973.

[58] Tingting Fan, Patrik Grychtol, Ronny Knut, Carlos Hernández-García, Daniel D. Hickstein, Dmitriy Zusin, Christian Gentry, Franklin J. Dollar, Christopher A. Mancuso, Craig W. Hogle, Ofer Kfir, Dominik Legut, Karel Carva, Jennifer L. Ellis, Kevin M. Dorney, Cong Chen, Oleg G. Shpyrko, Eric E. Fullerton, Oren Cohen, Peter M. Oppeneer, Dejan B. Milošević, Andreas Becker, Agnieszka A. Jaroń-Becker, Tenio Popmintchev, Margaret M. Murnane, and Henry C. Kapteyn. Bright circularly polarized soft X-ray high harmonics for X-ray magnetic

circular dichroism. Proceedings of the National Academy of Sciences, 112(46):14206–14211, 2015.

[59] Lutz Fechner, Nicolas Camus, Andreas Krupp, Joachim Ullrich, Thomas Pfeifer, and Robert Moshammer. Creation and survival of autoionizing states in strong laser fields. Phys. Rev. A, 92:051403, 2015.

[60] M V Fedorov, M-M Tehranchi, and S M Fedorov. Interference stabilization of Rydberg atoms: numerical calculations and physical models. Journal of Physics B: Atomic, Molecular and Optical Physics, 29(13):2907–2924, 1996.

[61] J. Feist, S. Nagele, C. Ticknor, B. I. Schneider, L. A. Collins, and J. Burgdörfer. Attosecond two-photon interferometry for doubly excited states of helium. Phys. Rev. Lett., 107:093005, 2011.

[62] M Ferray, A L'Huillier, X F Li, L A Lompre, G Mainfray, and C Manus. Multiple-harmonic conversion of 1064 nm radiation in rare gases. Journal of Physics B: Atomic, Molecular and Optical Physics, 21(3):L31–L35, 1988.

[63] Avner Fleischer, Eliyahu Bordo, Ofer Kfir, Pavel Sidorenko, and Oren Cohen. Polarization-fan high-order harmonics. Journal of Physics B: Atomic, Molecular and Optical Physics, 50(3):034001, 2017.

[64] Avner Fleischer, Ofer Kfir, Tzvi Diskin, Pavel Sidorenko, and Oren Cohen. Spin angular momentum and tunable polarization in high-harmonic generation. Nature Photonics, 8(7):543–549, 2014.

[65] Viorica Florescu, Olimpia Budriga, and Henri Bachau. Two-photon above-threshold ionization of hydrogen over the photon energy range from 15 ev to 50 kev. Phys. Rev. A, 84:033425, 2011.

[66] Viorica Florescu, Olimpia Budriga, and Henri Bachau. Two-photon ionization of hydrogen and hydrogenlike ions: Retardation effects on differential and total generalized cross sections. Phys. Rev. A, 86:033413, 2012.

[67] R. L. Fork, C. H. Brito Cruz, P. C. Becker, and C. V. Shank. Compression of optical pulses to six femtoseconds by using cubic phase compensation. Opt. Lett., 12(7):483–485, 1987.

[68] Bengt Fornberg. Generation of finite difference formulas on arbitrarily spaced grids. Mathematics of Computation, 51(184):699–706, 1988.

[69] Bengt Fornberg and Natasha Flyer. A Primer on Radial Basis Functions with Applications to the Geosciences. Society for Industrial and Applied Mathematics, Philadelphia, PA, 2015.

[70] F. Frank, C. Arrell, T. Witting, W. A. Okell, J. McKenna, J. S. Robinson, C. A. Haworth, D. Austin, H. Teng, I. A. Walmsley, J. P. Marangos, and J. W. G. Tisch. Invited review article: Technology for attosecond science. Review of Scientific Instruments, 83(7):071101, 2012.

[71] P. A. Franken, A. E. Hill, C. W. Peters, and G. Weinreich. Generation of optical harmonics. Phys. Rev. Lett., 7:118–119, 1961.

[72] R. R. Freeman, P. H. Bucksbaum, H. Milchberg, S. Darack, D. Schumacher, and M. E. Geusic. Above-threshold ionization with subpicosecond laser pulses. Phys. Rev. Lett., 59:1092–1095, 1987.

[73] M. Fushitani, C. N. Liu, A. Matsuda, T. Endo, Y. Toida, M. Nagasono, T. Togashi, M. Yabashi, T. Ishikawa, Y. Hikosaka, T. Morishita, and A. Hishikawa. Femtosecond two-photon rabi oscillations in excited he driven by ultrashort intense laser fields. Nature Photonics, 10(2):102–105, 2016.

[74] Xiaohui Gao, Gauri Patwardhan, Samuel Schrauth, Daiwei Zhu, Tenio Popmintchev, Henry C. Kapteyn, Margaret M. Murnane, Dmitri A. Romanov, Robert J. Levis, and Alexander L. Gaeta. Picosecond ionization dynamics in femtosecond filaments at high pressures. Phys. Rev. A, 95:013412, 2017.

[75] Gustavo A. Garcia, Laurent Nahon, Steven Daly, and Ivan Powis. Vibrationally induced inversion of photoelectron forward-backward asymmetry in chiral molecule photoionization by circularly polarized light. Nature Communications, 4(1):2132, 2013.

[76] Peipei Ge, Meng Han, Yongkai Deng, Qihuang Gong, and Yunquan Liu. Universal description of the attoclock with two-color corotating circular fields. Phys. Rev. Lett., 122:013201, 2019.

[77] Y. Gebre, J. Venzke, A. Jaron-Becker, and A. Becker. Transitions between Rydberg states in two-color corotating circularly polarized laser pulses. Phys. Rev. A, 103:013101, 2021.

[78] Xiaochun Gong, Cheng Lin, Feng He, Qiying Song, Kang Lin, Qinying Ji, Wenbin Zhang, Junyang Ma, Peifen Lu, Yunquan Liu, Heping Zeng, Weifeng Yang, and Jian Wu. Energy-resolved ultrashort delays of photoelectron emission clocked by orthogonal two-color laser fields. Phys. Rev. Lett., 118:143203, 2017.

[79] E. Goulielmakis, M. Schultze, M. Hofstetter, V. S. Yakovlev, J. Gagnon, M. Uiberacker, A. L. Aquila, E. M. Gullikson, D. T. Attwood, R. Kienberger, F. Krausz, and U. Kleineberg. Single-cycle nonlinear optics. Science, 320(5883):1614–1617, 2008.

[80] Eleftherios Goulielmakis, Zhi-Heng Loh, Adrian Wirth, Robin Santra, Nina Rohringer, Vladislav S. Yakovlev, Sergey Zherebtsov, Thomas Pfeifer, Abdallah M. Azzeer, Matthias F. Kling, Stephen R. Leone, and Ferenc Krausz. Real-time observation of valence electron motion. Nature, 466(7307):739–743, 2010.

[81] H. R. Gray, R. M. Whitley, and C. R. Stroud. Coherent trapping of atomic populations. Opt. Lett., 3(6):218–220, 1978.

[82] Alexei N. Grum-Grzhimailo, Elena V. Gryzlova, Ekaterina I. Staroselskaya, Joel Venzke, and Klaus Bartschat. Interfering one-photon and two-photon ionization by femtosecond VUV pulses in the region of an intermediate resonance. Physical Review A, 91(6):063418, 2015.

[83] V. Gruson, L. Barreau, á Jiménez-Galan, F. Risoud, J. Caillat, A. Maquet, B. Carré, F. Lepetit, J.-F. Hergott, T. Ruchon, L. Argenti, R. Taïeb, F. Martín, and P. Salières. Attosecond dynamics through a Fano resonance: Monitoring the birth of a photoelectron. Science, 354(6313):734–738, 2016.

[84] Jing Guo, Kai-Jun Yuan, Huizhong Lu, and André D Bandrauk. Spatiotemporal evolution of ultrafast magnetic-field generation in molecules with intense bichromatic circularly polarized uv laser pulses. Phys. Rev. A, 99:053416, 2019.

[85] Maria Göppert-Mayer. Über Elementarakte mit zwei Quantensprüngen. Annalen der Physik, 401(3):273–294, 1931.

[86] Louis H. Haber, Benjamin Doughty, and Stephen R. Leone. Energy-dependent photoelectron angular distributions of two-color two-photon above threshold ionization of atomic helium. Phys. Rev. A, 84:013416, 2011.

[87] Meng Han, Peipei Ge, Yun Shao, Qihuang Gong, and Yunquan Liu. Attoclock photoelectron interferometry with two-color corotating circular fields to probe the phase and the amplitude of emitting wave packets. Phys. Rev. Lett., 120:073202, 2018.

[88] Yong-Chang Han and Lars Bojer Madsen. Comparison between length and velocity gauges in quantum simulations of high-order harmonic generation. Phys. Rev. A, 81:063430, 2010.

[89] N. A. Hart, J. Strohaber, A. A. Kolomenskii, G. G. Paulus, D. Bauer, and H. A. Schuessler. Selective strong-field enhancement and suppression of ionization with short laser pulses. Phys. Rev. A, 93:063426, 2016.

[90] Alexander Hartung, Felipe Morales, Maksim Kunitski, Kevin Henrichs, Alina Laucke, Martin Richter, Till Jahnke, Anton Kalinin, Markus Schöffler, Lothar Ph. H. Schmidt, Misha Ivanov, Olga Smirnova, and Reinhard Dörner. Electron spin polarization in strong-field ionization of xenon atoms. Nature Photonics, 10(8):526–528, 2016.

[91] M. Th Hassan, T. T. Luu, A. Moulet, O. Raskazovskaya, P. Zhokhov, M. Garg, N. Karpowicz, A. M. Zheltikov, V. Pervak, F. Krausz, and E. Goulielmakis. Optical attosecond pulses and tracking the nonlinear response of bound electrons. Nature, 530(7588):66–70, 2016.

[92] F. He, C. Ruiz, and A. Becker. Absorbing boundaries in numerical solutions of the time-dependent Schrödinger equation on a grid using exterior complex scaling. Phys. Rev. A, 75:053407, 2007.

[93] Feng He, Camilo Ruiz, Andreas Becker, and Uwe Thumm. Attosecond probing of instantaneous AC-stark shifts in helium atoms. Journal of Physics B: Atomic, Molecular and Optical Physics, 44(21):211001, 2011.

[94] Mingrui He, Yang Li, Yueming Zhou, Min Li, Wei Cao, and Peixiang Lu. Direct visualization of valence electron motion using strong-field photoelectron holography. Phys. Rev. Lett., 120:133204, 2018.

[95] M. Hentschel, R. Kienberger, Ch. Spielmann, G. A. Reider, N. Milosevic, T. Brabec, P. Corkum, U. Heinzmann, M. Drescher, and F. Krausz. Attosecond metrology. Nature, 414(6863):509–513, 2001.

[96] Thushani Herath, Lu Yan, Suk Kyoung Lee, and Wen Li. Strong-field ionization rate depends on the sign of the magnetic quantum number. Phys. Rev. Lett., 109:043004, 2012.

[97] Vicente Hernandez, Jose E. Roman, and Vicente Vidal. SLEPc: A scalable and flexible toolkit for the solution of eigenvalue problems. ACM Trans. Math. Software, 31(3):351–362, 2005.

[98] C. Hernández-García, C. G. Durfee, D. D. Hickstein, T. Popmintchev, A. Meier, M. M. Murnane, H. C. Kapteyn, I. J. Sola, A. Jaron-Becker, and A. Becker. Schemes for generation of isolated attosecond pulses of pure circular polarization. Phys. Rev. A, 93:043855, 2016.

[99] John Heslar, Dmitry A. Telnov, and Shih-I Chu. Controlling electron quantum paths for generation of circularly polarized high-order harmonics by H_2^+ subject to tailored (ω, 2ω) counter-rotating laser fields. Phys. Rev. A, 97:043419, 2018.

[100] Daniel D. Hickstein, Franklin J. Dollar, Patrik Grychtol, Jennifer L. Ellis, Ronny Knut, Carlos Hernández-García, Dmitriy Zusin, Christian Gentry, Justin M. Shaw, Tingting Fan, Kevin M. Dorney, Andreas Becker, Agnieszka Jaroń-Becker, Henry C. Kapteyn, Margaret M. Murnane, and Charles G. Durfee. Non-collinear generation of angularly isolated circularly polarized high harmonics. Nature Photonics, 9(11):743–750, 2015.

[101] Van-Hung Hoang, Van-Hoang Le, C. D. Lin, and Anh-Thu Le. Retrieval of target structure information from laser-induced photoelectrons by few-cycle bicircular laser fields. Phys. Rev. A, 95:031402, 2017.

[102] Paul Hockett, Christer Z. Bisgaard, Owen J. Clarkin, and Albert Stolow. Time-resolved imaging of purely valence-electron dynamics during a chemical reaction. Nature Physics, 7(8):612–615, 2011.

[103] J. Hofbrucker, A. V. Volotka, and S. Fritzsche. Photoelectron distribution of nonresonant two-photon ionization of neutral atoms. Phys. Rev. A, 96:013409, 2017.

[104] J. Hofbrucker, A. V. Volotka, and S. Fritzsche. Maximum elliptical dichroism in atomic two-photon ionization. Phys. Rev. Lett., 121:053401, 2018.

[105] M. Holler, F. Schapper, L. Gallmann, and U. Keller. Attosecond electron wave-packet interference observed by transient absorption. Phys. Rev. Lett., 106:123601, 2011.

[106] S. X. Hu and L. A. Collins. Attosecond pump probe: Exploring ultrafast electron motion inside an atom. Phys. Rev. Lett., 96:073004, 2006.

[107] Cheng Huang, Mingmin Zhong, and Zhengmao Wu. Intensity-dependent two-electron emission dynamics in nonsequential double ionization by counter-rotating two-color circularly polarized laser fields. Opt. Express, 26(20):26045–26056, 2018.

[108] Pei-Chi Huang, Carlos Hernández-García, Jen-Ting Huang, Po-Yao Huang, Chih-Hsuan Lu, Laura Rego, Daniel D. Hickstein, Jennifer L. Ellis, Agnieszka Jaron-Becker, Andreas Becker, Shang-Da Yang, Charles G. Durfee, Luis Plaja, Henry C. Kapteyn, Margaret M. Murnane, A. H. Kung, and Ming-Chang Chen. Polarization control of isolated high-harmonic pulses. Nature Photonics, 12(6):349–354, 2018.

[109] M. Ilchen, N. Douguet, T. Mazza, A. J. Rafipoor, C. Callegari, P. Finetti, O. Plekan, K. C. Prince, A. Demidovich, C. Grazioli, L. Avaldi, P. Bolognesi, M. Coreno, M. Di Fraia, M. Devetta, Y. Ovcharenko, S. Düsterer, K. Ueda, K. Bartschat, A. N. Grum-Grzhimailo, A. V. Bozhevolnov, A. K. Kazansky, N. M. Kabachnik, and M. Meyer. Circular dichroism in multiphoton ionization of resonantly excited He^+ ions. Phys. Rev. Lett., 118:013002, 2017.

[110] M. Ilchen, G. Hartmann, E. V. Gryzlova, A. Achner, E. Allaria, A. Beckmann, M. Braune, J. Buck, C. Callegari, R. N. Coffee, R. Cucini, M. Danailov, A. De Fanis, A. Demidovich, E. Ferrari, P. Finetti, L. Glaser, A. Knie, A. O. Lindahl, O. Plekan, N. Mahne, T. Mazza, L. Raimondi, E. Roussel, F. Scholz, J. Seltmann, I. Shevchuk, C. Svetina, P. Walter, M. Zangrando, J. Viefhaus, A. N. Grum-Grzhimailo, and M. Meyer. Symmetry breakdown of electron emission in extreme ultraviolet photoionization of argon. Nature Communications, 9(1):4659, 2018.

[111] Nobuhisa Ishii, Keisuke Kaneshima, Kenta Kitano, Teruto Kanai, Shuntaro Watanabe, and Jiro Itatani. Carrier-envelope phase-dependent high harmonic generation in the water window using few-cycle infrared pulses. Nature Communications, 5(1):3331, 2014.

[112] Kenichi L. Ishikawa and Kiyoshi Ueda. Competition of resonant and nonresonant paths in resonance-enhanced two-photon single ionization of he by an ultrashort extreme-ultraviolet pulse. Phys. Rev. Lett., 108:033003, 2012.

[113] Kenichi L. Ishikawa and Kiyoshi Ueda. Photoelectron angular distribution and phase in two-photon single ionization of h and he by a femtosecond and attosecond extreme-ultraviolet pulse. Applied Sciences, 3(1):189–213, 2013.

[114] M. Isinger, R. J. Squibb, D. Busto, S. Zhong, A. Harth, D. Kroon, S. Nandi, C. L. Arnold, M. Miranda, J. M. Dahlström, E. Lindroth, R. Feifel, M. Gisselbrecht, and A. L'Huillier. Photoionization in the time and frequency domain. Science, 358(6365):893–896, 2017.

[115] I. A. Ivanov, Chang Hee Nam, and Kyung Taec Kim. Photoionization in the presence of circularly polarized fundamental and odd-order harmonic fields. Phys. Rev. A, 95:053401, 2017.

[116] Wei-Chao Jiang, Xiao-Min Tong, Renate Pazourek, Stefan Nagele, and Joachim Burgdörfer. Theory of bound-state coherences generated and probed by optical attosecond pulses. Phys. Rev. A, 101:053435, 2020.

[117] Á. Jiménez-Galán, N. Zhavoronkov, D. Ayuso, F. Morales, S. Patchkovskii, M. Schloz, E. Pisanty, O. Smirnova, and M. Ivanov. Control of attosecond light polarization in two-color bicircular fields. Phys. Rev. A, 97:023409, 2018.

[118] Álvaro Jiménez-Galán, Luca Argenti, and Fernando Martín. Modulation of attosecond beating in resonant two-photon ionization. Phys. Rev. Lett., 113:263001, 2014.

[119] R. R. Jones, D. W. Schumacher, and P. H. Bucksbaum. Population trapping in kr and xe in intense laser fields. Phys. Rev. A, 47:R49–R52, 1993.

[120] W. Kaiser and C. G. B. Garrett. Two-photon excitation in CaF_2: Eu^{2+}. Phys. Rev. Lett., 7:229–231, 1961.

[121] A. Kaldun, A. Blättermann, V. StooB, S. Donsa, H. Wei, R. Pazourek, S. Nagele, C. Ott, C. D. Lin, J. Burgdörfer, and T. Pfeifer. Observing the ultrafast buildup of a Fano resonance in the time domain. Science, 354(6313):738–741, 2016.

[122] A. K. Kazansky, A. V. Grigorieva, and N. M. Kabachnik. Dichroism in short-pulse two-color xuv plus ir multiphoton ionization of atoms. Phys. Rev. A, 85:053409, 2012.

[123] L. V. Keldysh. Ionization in the field of a strong electromagnetic wave. JETP, 20(5):1965, 1965.

[124] S. Kerbstadt, K. Eickhoff, T. Bayer, and M. Wollenhaupt. Odd electron wave packets from cycloidal ultrashort laser fields. Nature Communications, 10(1):658, 2019.

[125] Ofer Kfir, Patrik Grychtol, Emrah Turgut, Ronny Knut, Dmitriy Zusin, Dimitar Popmintchev, Tenio Popmintchev, Hans Nembach, Justin M. Shaw, Avner Fleischer, Henry Kapteyn, Margaret Murnane, and Oren Cohen. Generation of bright phase-matched circularly-polarized extreme ultraviolet high harmonics. Nature Photonics, 9(2):99–105, 2015.

[126] Md. Abdul Khan. Hyperspherical three-body model calculation for the bound 3,1s-states of coulombic systems. International Journal of Modern Physics E, 24(12):1550094, 2015.

[127] Kyung Taec Kim, Dong Hyuk Ko, Juyun Park, Nark Nyul Choi, Chul Min Kim, Kenichi L. Ishikawa, Jongmin Lee, and Chang Hee Nam. Amplitude and phase reconstruction of electron wave packets for probing ultrafast photoionization dynamics. Phys. Rev. Lett., 108:093001, 2012.

[128] Kyung Taec Kim, Chunmei Zhang, Thierry Ruchon, Jean-François Hergott, Thierry Auguste, D. M. Villeneuve, P. B. Corkum, and F. Quéré. Photonic streaking of attosecond pulse trains. Nature Photonics, 7(8):651–656, 2013.

[129] K. Klünder, J. M. Dahlström, M. Gisselbrecht, T. Fordell, M. Swoboda, D. Guénot, P. Johnsson, J. Caillat, J. Mauritsson, A. Maquet, R. Taïeb, and A. L'Huillier. Probing single-photon ionization on the attosecond time scale. Phys. Rev. Lett., 106:143002, 2011.

[130] K. Klünder, P. Johnsson, M. Swoboda, A. L'Huillier, G. Sansone, M. Nisoli, M. J. J. Vrakking, K. J. Schafer, and J. Mauritsson. Reconstruction of attosecond electron wave packets using quantum state holography. Phys. Rev. A, 88:033404, 2013.

[131] Oleg Kornilov, Chia C. Wang, Oliver Bünermann, Andrew T. Healy, Mathew Leonard, Chunte Peng, Stephen R. Leone, Daniel M. Neumark, and Oliver Gessner. Ultrafast dynamics in helium nanodroplets probed by femtosecond time-resolved euv photoelectron imaging. The Journal of Physical Chemistry A, 114(3):1437–1445, 2010. PMID: 20043659.

[132] M. Kotur, D. Guénot, Á Jiménez-Galán, D. Kroon, E. W. Larsen, M. Louisy, S. Bengtsson, M. Miranda, J. Mauritsson, C. L. Arnold, S. E. Canton, M. Gisselbrecht, T. Carette, J. M. Dahlström, E. Lindroth, A. Maquet, L. Argenti, F. Martín, and A. L'Huillier. Spectral phase measurement of a Fano resonance using tunable attosecond pulses. Nature Communications, 7(1):10566, 2016.

[133] V. P. Krainov. Ionization rates and energy and angular distributions at the barrier-suppression ionization of complex atoms and atomic ions. J. Opt. Soc. Am. B, 14(2):425–431, 1997.

[134] K. Krajewska, I. I. Fabrikant, and A. F. Starace. Threshold effects in strong-field ionization: Energy shifts and rydberg structures. Phys. Rev. A, 86:053410, 2012.

[135] Ferenc Krausz and Misha Ivanov. Attosecond physics. Rev. Mod. Phys., 81:163–234, 2009.

[136] G Laplanche, M Jaouen, and A Rachman. Angular distributions and polarisation phenomena in non-resonant multiphoton ionisation of alkali-metal atoms. i. formal theory. Journal of Physics B: Atomic and Molecular Physics, 19(1):79–100, 1986.

[137] Manuel Lara-Astiaso, Mara Galli, Andrea Trabattoni, Alicia Palacios, David Ayuso, Fabio Frassetto, Luca Poletto, Simone De Camillis, Jason Greenwood, Piero Decleva, Ivano Tavernelli, Francesca Calegari, Mauro Nisoli, and Fernando Martín. Attosecond pump–probe spectroscopy of charge dynamics in tryptophan. The Journal of Physical Chemistry Letters, 9(16):4570–4577, 2018.

[138] Seyedreza Larimian, Sonia Erattupuzha, Christoph Lemell, Shuhei Yoshida, Stefan Nagele, Raffael Maurer, Andrius Baltuška, Joachim Burgdörfer, Markus Kitzler, and Xinhua Xie. Coincidence spectroscopy of high-lying Rydberg states produced in strong laser fields. Phys. Rev. A, 94:033401, 2016.

[139] Gavriel Lerner, Tzvi Diskin, Ofer Neufeld, Ofer Kfir, and Oren Cohen. Selective suppression of high-order harmonics within phase-matched spectral regions. Opt. Lett., 42(7):1349–1352, 2017.

[140] M. Lewenstein, Ph. Balcou, M. Yu. Ivanov, Anne L'Huillier, and P. B. Corkum. Theory of high-harmonic generation by low-frequency laser fields. Phys. Rev. A, 49:2117–2132, 1994.

[141] Min Li, Wei-Chao Jiang, Hui Xie, Siqiang Luo, Yueming Zhou, and Peixiang Lu. Strong-field photoelectron holography of atoms by bicircular two-color laser pulses. Phys. Rev. A, 97:023415, 2018.

[142] Min Li, Peng Zhang, Siqiang Luo, Yueming Zhou, Qingbin Zhang, Pengfei Lan, and Peixiang Lu. Selective enhancement of resonant multiphoton ionization with strong laser fields. Phys. Rev. A, 92:063404, 2015.

[143] Mu-Zi Li, Yan Xu, Guang-Rui Jia, and Xue-Bin Bian. Controlling polarization of high-order harmonic generation by molecular alignment in a bicircular laser field. Phys. Rev. A, 100:033410, 2019.

[144] Qianguang Li, Xiao-Min Tong, Toru Morishita, Cheng Jin, Hui Wei, and C D Lin. Rydberg states in the strong field ionization of hydrogen by 800, 1200 and 1600 nm lasers. Journal of Physics B: Atomic, Molecular and Optical Physics, 47(20):204019, 2014.

[145] Qianguang Li, Xiao-Min Tong, Toru Morishita, Hui Wei, and C. D. Lin. Fine structures in the intensity dependence of excitation and ionization probabilities of hydrogen atoms in intense 800-nm laser pulses. Phys. Rev. A, 89:023421, 2014.

[146] Kang Lin, Xinyan Jia, Zuqing Yu, Feng He, Junyang Ma, Hui Li, Xiaochun Gong, Qiying Song, Qinying Ji, Wenbin Zhang, Hanxiao Li, Peifen Lu, Heping Zeng, Jing Chen, and Jian Wu. Comparison study of strong-field ionization of molecules and atoms by bicircular two-color femtosecond laser pulses. Phys. Rev. Lett., 119:203202, 2017.

[147] Kunlong Liu, Hongcheng Ni, Klaus Renziehausen, Jan-Michael Rost, and Ingo Barth. Deformation of atomic $p_{\pm}$ orbitals in strong elliptically polarized laser fields: Ionization time drifts and spatial photoelectron separation. Phys. Rev. Lett., 121:203201, 2018.

[148] Ming-Ming Liu, Yun Shao, Meng Han, Peipei Ge, Yongkai Deng, Chengyin Wu, Qihuang Gong, and Yunquan Liu. Energy- and momentum-resolved photoelectron spin polarization in multiphoton ionization of xe by circularly polarized fields. Phys. Rev. Lett., 120:043201, 2018.

[149] Xi Liu, Xiaosong Zhu, Liang Li, Yang Li, Qingbin Zhang, Pengfei Lan, and Peixiang Lu. Selection rules of high-order-harmonic generation: Symmetries of molecules and laser fields. Phys. Rev. A, 94:033410, 2016.

[150] S. Long, W. Becker, and J. K. McIver. Model calculations of polarization-dependent two-color high-harmonic generation. Phys. Rev. A, 52:2262–2278, 1995.

[151] A. Ludwig, J. Maurer, B. W. Mayer, C. R. Phillips, L. Gallmann, and U. Keller. Breakdown of the dipole approximation in strong-field ionization. Phys. Rev. Lett., 113:243001, 2014.

[152] Hang Lv, Wanlong Zuo, Lei Zhao, Haifeng Xu, Mingxing Jin, Dajun Ding, Shilin Hu, and Jing Chen. Comparative study on atomic and molecular rydberg-state excitation in strong infrared laser fields. Phys. Rev. A, 93:033415, 2016.

[153] R. Ma, K. Motomura, K. L. Ishikawa, S. Mondal, H. Fukuzawa, A. Yamada, K. Ueda, K. Nagaya, S. Yase, Y. Mizoguchi, M. Yao, A. Rouze, A. Hundermark, M. J. J. Vrakking, P. Johnsson, M. Nagasono, K. Tono, T. Togashi, Y. Senba, H. Ohashi, M. Yabashi, and T. Ishikawa. Photoelectron angular distributions for the two-photon ionization of helium by ultrashort extreme ultraviolet free-electron laser pulses. Journal of Physics B: Atomic, Molecular and Optical Physics, 46(16):164018, 2013.

[154] Xiaomeng Ma, Yueming Zhou, Yinbo Chen, Min Li, Yang Li, Qingbin Zhang, and Peixiang Lu. Timing the release of the correlated electrons in strong-field nonsequential double ionization by circularly polarized two-color laser fields. Opt. Express, 27(3):1825–1837, 2019.

[155] Christopher A. Mancuso, Kevin M. Dorney, Daniel D. Hickstein, Jan L. Chaloupka, Jennifer L. Ellis, Franklin J. Dollar, Ronny Knut, Patrik Grychtol, Dmitriy Zusin, Christian Gentry, Maithreyi Gopalakrishnan, Henry C. Kapteyn, and Margaret M. Murnane. Controlling nonsequential double ionization in two-color circularly polarized femtosecond laser fields. Phys. Rev. Lett., 117:133201, 2016.

[156] Christopher A. Mancuso, Kevin M. Dorney, Daniel D. Hickstein, Jan L. Chaloupka, Xiao-Min Tong, Jennifer L. Ellis, Henry C. Kapteyn, and Margaret M. Murnane. Observation of ionization enhancement in two-color circularly polarized laser fields. Phys. Rev. A, 96:023402, 2017.

[157] Christopher A. Mancuso, Daniel D. Hickstein, Kevin M. Dorney, Jennifer L. Ellis, Elvedin Hasović, Ronny Knut, Patrik Grychtol, Christian Gentry, Maithreyi Gopalakrishnan, Dmitriy Zusin, Franklin J. Dollar, Xiao-Min Tong, Dejan B. Milošević, Wilhelm Becker, Henry C. Kapteyn, and Margaret M. Murnane. Controlling electron-ion rescattering in two-color circularly polarized femtosecond laser fields. Phys. Rev. A, 93:053406, 2016.

[158] A. Marinelli, J. MacArthur, P. Emma, M. Guetg, C. Field, D. Kharakh, A. A. Lutman, Y. Ding, and Z. Huang. Experimental demonstration of a single-spike hard-x-ray free-electron laser starting from noise. Applied Physics Letters, 111(15):151101, 2017.

[159] F Mauger, A D Bandrauk, and T Uzer. Circularly polarized molecular high harmonic generation using a bicircular laser. Journal of Physics B: Atomic, Molecular and Optical Physics, 49(10):10LT01, 2016.

[160] F. Maulbetsch and J. S. Briggs. Asymmetry parameter for double photoionization. Physical Review Letters, 68(13):2004–2006, 1992.

[161] J. Mauritsson, T. Remetter, M. Swoboda, K. Klünder, A. L'Huillier, K. J. Schafer, O. Ghafur, F. Kelkensberg, W. Siu, P. Johnsson, M. J. J. Vrakking, I. Znakovskaya, T. Uphues, S. Zherebtsov, M. F. Kling, F. Lépine, E. Benedetti, F. Ferrari, G. Sansone, and M. Nisoli. Attosecond electron spectroscopy using a novel interferometric pump-probe technique. Phys. Rev. Lett., 105:053001, 2010.

[162] T. Mazza, M. Ilchen, A. J. Rafipoor, C. Callegari, P. Finetti, O. Plekan, K. C. Prince, R. Richter, M. B. Danailov, A. Demidovich, G. De Ninno, C. Grazioli, R. Ivanov, N. Mahne, L. Raimondi, C. Svetina, L. Avaldi, P. Bolognesi, M. Coreno, P. O'Keeffe, M. Di Fraia, M. Devetta, Y. Ovcharenko, Th Möller, V. Lyamayev, F. Stienkemeier, S. Düsterer, K. Ueda, J. T. Costello, A. K. Kazansky, N. M. Kabachnik, and M. Meyer. Determining the polarization state of an extreme ultraviolet free-electron laser beam using atomic circular dichroism. Nature Communications, 5(1):1–6, 2014.

[163] K. C. McCormick, Keller J., Burd S. C., Wineland D. J., Wilson A. C., and Leibfried D. Quantum-enhanced sensing of a single-ion mechanical oscillator. Nature, 572:86, 2019.

[164] A. McPherson, G. Gibson, H. Jara, U. Johann, T. S. Luk, I. A. McIntyre, K. Boyer, and C. K. Rhodes. Studies of multiphoton production of vacuum-ultraviolet radiation in the rare gases. J. Opt. Soc. Am. B, 4(4):595–601, 1987.

[165] Lukas Medišauskas, Jack Wragg, Hugo van der Hart, and Misha Yu. Ivanov. Generating isolated elliptically polarized attosecond pulses using bichromatic counterrotating circularly polarized laser fields. Phys. Rev. Lett., 115:153001, 2015.

[166] Lise Meitner. Über die Entstehung der β-Strahl-Spektren radioaktiver Substanzen. Zeitschrift für Physik, 9(1):131–144, 1922.

[167] D. B. Milošević. Possibility of introducing spin into attoscience with spin-polarized electrons produced by a bichromatic circularly polarized laser field. Phys. Rev. A, 93:051402, 2016.

[168] D. B. Milošević and W. Becker. Improved strong-field approximation and quantum-orbit theory: Application to ionization by a bicircular laser field. Phys. Rev. A, 93:063418, 2016.

[169] D B Milošević. High-order harmonic generation by a bichromatic elliptically polarized field: conservation of angular momentum. Journal of Physics B: Atomic, Molecular and Optical Physics, 48(17):171001, 2015.

[170] Dejan B. Milošević. Generation of elliptically polarized attosecond pulse trains. Opt. Lett., 40(10):2381–2384, 2015.

[171] R. Mitzner, B. Siemer, M. Neeb, T. Noll, F. Siewert, S. Roling, M. Rutkowski, A.A. Sorokin, M. Richter, P. Juranic, K. Tiedtke, J. Feldhaus, W. Eberhardt, and H. Zacharias. Spatio-temporal coherence of free electron laser pulses in the soft x-ray regime. Opt. Express, 16(24):19909–19919, 2008.

[172] Erik P. Månsson, Diego Guénot, Cord L. Arnold, David Kroon, Susan Kasper, J. Marcus Dahlström, Eva Lindroth, Anatoli S. Kheifets, Anne L'Huillier, Stacey L. Sorensen, and Mathieu Gisselbrecht. Double ionization probed on the attosecond timescale. Nature Physics, 10(3):207–211, 2014.

[173] H. G. Muller. Reconstruction of attosecond harmonic beating by interference of two-photon transitions. Applied Physics B, 74(1):s17–s21, 2002.

[174] Eadweard Muybridge. The horse in motion. Sacramento Daily Union, 1978.

[175] J. M. Ngoko Djiokap, S. X. Hu, L. B. Madsen, N. L. Manakov, A. V. Meremianin, and Anthony F. Starace. Electron vortices in photoionization by circularly polarized attosecond pulses. Phys. Rev. Lett., 115:113004, 2015.

[176] E. R. Nightingale. Phenomenological theory of ion solvation. effective radii of hydrated ions. The Journal of Physical Chemistry, 63(9):1381–1387, 1959.

[177] L A A Nikolopoulos and P Lambropoulos. Multichannel theory of two-photon single and double ionization of helium. Journal of Physics B: Atomic, Molecular and Optical Physics, 34(4):545–564, 2001.

[178] M. Nisoli, S. De Silvestri, and O. Svelto. Generation of high energy 10 fs pulses by a new pulse compression technique. Applied Physics Letters, 68(20):2793–2795, 1996.

[179] M. Nisoli, S. De Silvestri, O. Svelto, R. Szipöcs, K. Ferencz, Ch. Spielmann, S. Sartania, and F. Krausz. Compression of high-energy laser pulses below 5 fs. Opt. Lett., 22(8):522–524, 1997.

[180] T. Nubbemeyer, K. Gorling, A. Saenz, U. Eichmann, and W. Sandner. Strong-field tunneling without ionization. Phys. Rev. Lett., 101:233001, 2008.

[181] S. Odžak, E. Hasović, and D. B. Milošević. High-order harmonic generation in polyatomic molecules induced by a bicircular laser field. Phys. Rev. A, 94:033419, 2016.

[182] C. H. Raymond Ooi, WaiLoon Ho, and A. D. Bandrauk. Photoelectron angular distributions of excited atoms in intense laser fields. Phys. Rev. A, 90:013417, 2014.

[183] Christian Ott, Andreas Kaldun, Luca Argenti, Philipp Raith, Kristina Meyer, Martin Laux, Yizhu Zhang, Alexander Blättermann, Steffen Hagstotz, Thomas Ding, Robert Heck, Javier Madroñero, Fernando Martín, and Thomas Pfeifer. Reconstruction and control of a time-dependent two-electron wave packet. Nature, 516(7531):374–378, 2014.

[184] Willi Paufler, Birger Böning, and Stephan Fritzsche. Tailored orbital angular momentum in high-order harmonic generation with bicircular laguerre-gaussian beams. Phys. Rev. A, 98:011401, 2018.

[185] P. M. Paul, E. S. Toma, P. Breger, G. Mullot, F. Augé, Ph Balcou, H. G. Muller, and P. Agostini. Observation of a Train of Attosecond Pulses from High Harmonic Generation. Science, 292(5522):1689–1692, 2001.

[186] Renate Pazourek, Johannes Feist, Stefan Nagele, and Joachim Burgdörfer. Attosecond streaking of correlated two-electron transitions in helium. Phys. Rev. Lett., 108:163001, 2012.

[187] Renate Pazourek, Stefan Nagele, and Joachim Burgdörfer. Attosecond chronoscopy of photoemission. Rev. Mod. Phys., 87:765–802, 2015.

[188] Peng Peng, Claude Marceau, and David M. Villeneuve. Attosecond imaging of molecules using high harmonic spectroscopy. Nature Reviews Physics, 1(2):144–155, 2019.

[189] D. Pengel, S. Kerbstadt, D. Johannmeyer, L. Englert, T. Bayer, and M. Wollenhaupt. Electron vortices in femtosecond multiphoton ionization. Phys. Rev. Lett., 118:053003, 2017.

[190] M. D. Perry, A. Szoke, and K. C. Kulander. Resonantly enhanced above-threshold ionization of helium. Phys. Rev. Lett., 63:1058–1061, 1989.

[191] Thomas Pfeifer, Yuhai Jiang, Stefan Düsterer, Robert Moshammer, and Joachim Ullrich. Partial-coherence method to model experimental free-electron laser pulse statistics. Opt. Lett., 35(20):3441–3443, 2010.

[192] Adrian N. Pfeiffer, Claudio Cirelli, Mathias Smolarski, Reinhard Dörner, and Ursula Keller. Timing the release in sequential double ionization. Nature Physics, 7(5):428–433, 2011.

[193] Liang-Wen Pi and Anthony F. Starace. Potential barrier effects in two-photon ionization processes. Phys. Rev. A, 82:053414, 2010.

[194] B. Piraux, F. Mota-Furtado, P. F. O'Mahony, A. Galstyan, and Yu. V. Popov. Excitation of rydberg wave packets in the tunneling regime. Phys. Rev. A, 96:043403, 2017.

[195] Emilio Pisanty and Álvaro Jiménez-Galán. Strong-field approximation in a rotating frame: High-order harmonic emission from p states in bicircular fields. Phys. Rev. A, 96:063401, 2017.

[196] Emilio Pisanty, Suren Sukiasyan, and Misha Ivanov. Spin conservation in high-order-harmonic generation using bicircular fields. Phys. Rev. A, 90:043829, 2014.

[197] Tenio Popmintchev, Ming-Chang Chen, Paul Arpin, Margaret M. Murnane, and Henry C. Kapteyn. The attosecond nonlinear optics of bright coherent X-ray generation. Nature Photonics, 4:822, 2010.

[198] Katharina E. Priebe, Christopher Rathje, Sergey V. Yalunin, Thorsten Hohage, Armin Feist, Sascha Schäfer, and Claus Ropers. Attosecond electron pulse trains and quantum state reconstruction in ultrafast transmission electron microscopy. Nature Photonics, 11(12):793–797, 2017.

[199] K. C. Prince, E. Allaria, C. Callegari, R. Cucini, G. De Ninno, S. Di Mitri, B. Diviacco, E. Ferrari, P. Finetti, D. Gauthier, L. Giannessi, N. Mahne, G. Penco, O. Plekan, L. Raimondi, P. Rebernik, E. Roussel, C. Svetina, M. Trovò, M. Zangrando, M. Negro, P. Carpeggiani, M. Reduzzi, G. Sansone, A. N. Grum-Grzhimailo, E. V. Gryzlova, S. I. Strakhova, K. Bartschat, N. Douguet, J. Venzke, D. Iablonskyi, Y. Kumagai, T. Takanashi, K. Ueda, A. Fischer, M. Coreno, F. Stienkemeier, Y. Ovcharenko, T. Mazza, and M. Meyer. Coherent control with a short-wavelength free-electron laser. Nature Photonics, 10(3):176–179, 2016.

[200] I. Pupeza, D. Sánchez, J. Zhang, N. Lilienfein, M. Seidel, N. Karpowicz, T. Paasch-Colberg, I. Znakovskaya, M. Pescher, W. Schweinberger, V. Pervak, E. Fill, O. Pronin, Z. Wei, F. Krausz, A. Apolonski, and J. Biegert. High-power sub-two-cycle mid-infrared pulses at 100 mhz repetition rate. Nature Photonics, 9(11):721–724, 2015.

[201] Krupa Ramasesha, Stephen R. Leone, and Daniel M. Neumark. Real-Time Probing of Electron Dynamics Using Attosecond Time-Resolved Spectroscopy. Annual Review of Physical Chemistry, 67(1):41–63, 2016.

[202] Jens Rauschenberger, Hoerlein, and Christoph Hauri. High-harmonic radiation for seeding the swiss free electron laser. `https://andor.oxinst.com/learning/view/article/high-harmonic-radiation-for-seeding-the-swiss-free-electron-laser`.

[203] Daniel M. Reich and Lars Bojer Madsen. Illuminating molecular symmetries with bicircular high-order-harmonic generation. Phys. Rev. Lett., 117:133902, 2016.

[204] Ran Reiff, Tennesse Joyce, Agnieszka Jaron-Becker, and Andreas Becker. Single-active electron calculations of high-order harmonic generation from valence shells in atoms for quantitative comparison with TDDFT calculations. Journal of Physics Communications, 2020.

[205] Howard R. Reiss. Effect of an intense electromagnetic field on a weakly bound system. Phys. Rev. A, 22:1786–1813, 1980.

[206] T. Remetter, P. Johnsson, J. Mauritsson, K. Varjú, Y. Ni, F. Lépine, E. Gustafsson, M. Kling, J. Khan, R. López-Martens, K. J. Schafer, M. J. J. Vrakking, and A. L'Huillier. Attosecond electron wave packet interferometry. Nature Physics, 2(5):323–326, 2006.

[207] H F Rey and H W van der Hart. Angular distributions in two-colour two-photon ionization of he. Journal of Physics B: Atomic, Molecular and Optical Physics, 47(22):225601, 2014.

[208] J. E. Roman, C. Campos, E. Romero, and A. Tomas. SLEPc users manual. Technical Report DSIC-II/24/02 - Revision 3.7, D. Sistemes Informàtics i Computació, Universitat Politècnica de València, 2016.

[209] H. Rottke, B. Wolff-Rottke, D. Feldmann, K. H. Welge, Martin Dörr, R. M. Potvliege, and Robin Shakeshaft. Atomic hydrogen in a strong optical radiation field. Phys. Rev. A, 49:4837–4851, 1994.

[210] A. Rouzée, P. Johnsson, E. V. Gryzlova, H. Fukuzawa, A. Yamada, W. Siu, Y. Huismans, E. Louis, F. Bijkerk, D. M. P. Holland, A. N. Grum-Grzhimailo, N. M. Kabachnik, M. J. J. Vrakking, and K. Ueda. Angle-resolved photoelectron spectroscopy of sequential three-photon triple ionization of neon at 90.5 eV photon energy. Phys. Rev. A, 83:031401, 2011.

[211] Womersley RS and Sloan IH. Interpolation and cubature on the sphere. `http://web.maths.unsw.edu.au/~rsw/Sphere/`, 2007.

[212] M. Sabbar, S. Heuser, R. Boge, M. Lucchini, T. Carette, E. Lindroth, L. Gallmann, C. Cirelli, and U. Keller. Resonance effects in photoemission time delays. Phys. Rev. Lett., 115:133001, 2015.

[213] M Saffman. Quantum computing with atomic qubits and Rydberg interactions: progress and challenges. Journal of Physics B: Atomic, Molecular and Optical Physics, 49(20):202001, 2016.

[214] Takahiro Sato, Atsushi Iwasaki, Kazuki Ishibashi, Tomoya Okino, Kaoru Yamanouchi, Junichi Adachi, Akira Yagishita, Hiroki Yazawa, Fumihiko Kannari, Makoto Aoyma, Koichi

Yamakawa, Katsumi Midorikawa, Hidetoshi Nakano, Makina Yabashi, Mitsuru Nagasono, Atsushi Higashiya, and Tetsuya Ishikawa. Determination of the absolute two-photon ionization cross section of He by an XUV free electron laser. Journal of Physics B: Atomic, Molecular and Optical Physics, 44(16), 2011.

[215] Timothy Sauer. Numerical Analysis. Pearson Education, Inc., Boston, 2012.

[216] M. Schultze, M. Fieß, N. Karpowicz, J. Gagnon, M. Korbman, M. Hofstetter, S. Neppl, A. L. Cavalieri, Y. Komninos, Th Mercouris, C. A. Nicolaides, R. Pazourek, S. Nagele, J. Feist, J. Burgdörfer, A. M. Azzeer, R. Ernstorfer, R. Kienberger, U. Kleineberg, E. Goulielmakis, F. Krausz, and V. S. Yakovlev. Delay in Photoemission. Science, 328(5986):1658–1662, 2010.

[217] Armin Scrinzi. Infinite-range exterior complex scaling as a perfect absorber in time-dependent problems. Phys. Rev. A, 81:053845, 2010.

[218] E. A. Seddon, J. A. Clarke, D. J. Dunning, C. Masciovecchio, C. J. Milne, F. Parmigiani, D. Rugg, J. C. H. Spence, N. R. Thompson, K. Ueda, S. M. Vinko, J. S. Wark, and W. Wurth. Short-wavelength free-electron laser sources and science: a review. Reports on Progress in Physics, 80(11):115901, 2017.

[219] E. E. Serebryannikov and A. M. Zheltikov. Strong-field photoionization as excited-state tunneling. Phys. Rev. Lett., 116:123901, 2016.

[220] Robin Shakeshaft. Two-photon single and double ionization of helium. Phys. Rev. A, 76:063405, 2007.

[221] Yun Shao, Min Li, Ming-Ming Liu, Xufei Sun, Xiguo Xie, Peng Wang, Yongkai Deng, Chengyin Wu, Qihuang Gong, and Yunquan Liu. Isolating resonant excitation from above-threshold ionization. Phys. Rev. A, 92:013415, 2015.

[222] T Sørevik, L B Madsen, and J P Hansen. A spectral method for integration of the time-dependent schrödinger equation in hyperspherical coordinates. Journal of Physics A: Mathematical and General, 38(31):6977–6985, 2005.

[223] C. Spezzani, E. Allaria, M. Coreno, B. Diviacco, E. Ferrari, G. Geloni, E. Karantzoulis, B. Mahieu, M. Vento, and G. De Ninno. Coherent light with tunable polarization from single-pass free-electron lasers. Phys. Rev. Lett., 107:084801, 2011.

[224] Jing Su, Hongcheng Ni, Agnieszka Jaroń-Becker, and Andreas Becker. Time delays in two-photon ionization. Phys. Rev. Lett., 113:263002, 2014.

[225] Toshinori Suzuki. Ultrafast electronic dynamics in polyatomic molecules studied using femtosecond vacuum ultraviolet and x-ray pulses. Journal of Physics B: Atomic, Molecular and Optical Physics, 47(12):124001, 2014.

[226] Zhensheng Tao, Cong Chen, Tibor Szilvási, Mark Keller, Manos Mavrikakis, Henry Kapteyn, and Margaret Murnane. Direct time-domain observation of attosecond final-state lifetimes in photoemission from solids. Science, 353(6294):62–67, 2016.

[227] E S Toma, Ph Antoine, A de Bohan, and H G Muller. Resonance-enhanced high-harmonic generation. Journal of Physics B: Atomic, Molecular and Optical Physics, 32(24):5843–5852, 1999.

[228] D. Trabert, A. Hartung, S. Eckart, F. Trinter, A. Kalinin, M. Schöffler, L. Ph. H. Schmidt, T. Jahnke, M. Kunitski, and R. Dörner. Spin and angular momentum in strong-field ionization. Phys. Rev. Lett., 120:043202, 2018.

[229] J Ullrich, R Moshammer, A Dorn, R Dörner, L Ph H Schmidt, and H Schmidt-Böcking. Recoil-ion and electron momentum spectroscopy: reaction-microscopes. Reports on Progress in Physics, 66(9):1463–1545, 2003.

[230] Hugo W van der Hart and Peter Bingham. Two- and three-photon ionization of He between 1013 and 1014 w cm-2. Journal of Physics B: Atomic, Molecular and Optical Physics, 38(3):207–221, 2005.

[231] W. Vanroose, D. A. Horner, F. Martín, T. N. Rescigno, and C. W. McCurdy. Double photoionization of aligned molecular hydrogen. Phys. Rev. A, 74:052702, 2006.

[232] J. Venzke, A. Becker, and A. Jaron-Becker. Asymmetries in ionization of atomic superposition states by ultrashort laser pulses. Scientific Reports, 10(1):16164, 2020.

[233] J. Venzke, A. Becker, and A. Jaron-Becker. Imaging ring-current wave packets in the helium atom. Phys. Rev. A, 103:042808, 2021.

[234] J. Venzke, Y. Gebre, A. Becker, and A. Jaroń-Becker. Pathways to excitation of atoms with bicircular laser pulses. Phys. Rev. A, 101:053425, 2020.

[235] J. Venzke, A. Jaroń-Becker, and A. Becker. Ionization of helium by an ultrashort extreme-ultraviolet laser pulse. Journal of Physics B: Atomic, Molecular and Optical Physics, 53(8):085602, 2020.

[236] J. Venzke, T. Joyce, Z. Xue, A. Becker, and A. Jaron-Becker. Central frequency of few-cycle laser pulses in strong-field processes. Physical Review A, 98(6):063409, 2018.

[237] J. Venzke, R. Reiff, Z. Xue, A. Jaroń-Becker, and A. Becker. Angular momentum distribution in rydberg states excited by a strong laser pulse. Phys. Rev. A, 98:043434, 2018.

[238] Marc J. J. Vrakking. Attosecond imaging. Physical Chemistry Chemical Physics, 16(7):2775–2789, 2014.

[239] B. Walker, B. Sheehy, L. F. DiMauro, P. Agostini, K. J. Schafer, and K. C. Kulander. Precision measurement of strong field double ionization of helium. Phys. Rev. Lett., 73:1227–1230, 1994.

[240] Samuel G. Walt, Niraghatam Bhargava Ram, Marcos Atala, Nikolay I. Shvetsov-Shilovski, Aaron von Conta, Denitsa Baykusheva, Manfred Lein, and Hans Jakob Wörner. Dynamics of valence-shell electrons and nuclei probed by strong-field holography and rescattering. Nature Communications, 8(1):1–8, 2017.

[241] Jun-Ping Wang and Feng He. Tunneling ionization of neon atoms carrying different orbital angular momenta in strong laser fields. Phys. Rev. A, 95:043420, 2017.

[242] Linjun Wang, Run Long, and Oleg V. Prezhdo. Time-domain ab initio modeling of photoinduced dynamics at nanoscale interfaces. Annual Review of Physical Chemistry, 66(1):549–579, 2015. PMID: 25622188.

[243] Mu-Xue Wang, Hao Liang, Xiang-Ru Xiao, Si-Ge Chen, and Liang-You Peng. Time-dependent perturbation theory beyond the dipole approximation for two-photon ionization of atoms. Physical Review A, 99(2):023407, 2019.

[244] J. Wätzel and J. Berakdar. Discerning on a sub-optical-wavelength the attosecond time delays in electron emission from magnetic sublevels by optical vortices. Phys. Rev. A, 94:033414, 2016.

[245] Zhao Xi, Yang Yu-Jun, Liu Xue-Shen, and Wang Bing-Bing. Carrier envelope phase effect of a long duration pulse in the low frequency region. Chinese Physics Letters, 31(04):043202, 2014.

[246] Xinhua Xie, Stefan Roither, Daniil Kartashov, Emil Persson, Diego G. Arbó, Li Zhang, Stefanie Gräfe, Markus S. Schöffler, Joachim Burgdörfer, Andrius Baltuška, and Markus Kitzler. Attosecond probe of valence-electron wave packets by subcycle sculpted laser fields. Phys. Rev. Lett., 108:193004, 2012.

[247] Wei-Hao Xiong, Jian-Zhao Jin, Liang-You Peng, and Qihuang Gong. Numerical observation of two sets of low-order harmonics near the ionization threshold. Phys. Rev. A, 96:023418, 2017.

[248] Wei-Hao Xiong, Xiang-Ru Xiao, Liang-You Peng, and Qihuang Gong. Correspondence of below-threshold high-order-harmonic generation and frustrated tunneling ionization. Phys. Rev. A, 94:013417, 2016.

[249] Junliang Xu, Cosmin I. Blaga, Pierre Agostini, and Louis F. DiMauro. Time-resolved molecular imaging. Journal of Physics B: Atomic, Molecular and Optical Physics, 49(11):112001, 2016.

[250] Yi-Yian Yin, Ce Chen, D. S. Elliott, and A. V. Smith. Asymmetric photoelectron angular distributions from interfering photoionization processes. Physical Review Letters, 69(16):2353–2356, 1992.

[251] Linda Young, Kiyoshi Ueda, Markus Gühr, Philip H. Bucksbaum, Marc Simon, Shaul Mukamel, Nina Rohringer, Kevin C. Prince, Claudio Masciovecchio, Michael Meyer, Artem Rudenko, Daniel Rolles, Christoph Bostedt, Matthias Fuchs, David A. Reis, Robin Santra, Henry Kapteyn, Margaret Murnane, Heide Ibrahim, François Légaré, Marc Vrakking, Marcus Isinger, David Kroon, Mathieu Gisselbrecht, Anne L'Huillier, Hans Jakob Wörner, and Stephen R. Leone. Roadmap of ultrafast x-ray atomic and molecular physics. Journal of Physics B: Atomic, Molecular and Optical Physics, 51(3):032003, 2018.

[252] Wei-Wei Yu, Shuai Ben, Lei Ji, Yu-Shuang Liu, Jing Guo, and Xue-Shen Liu. Enhancement of nonsequential double ionization in counter-rotating two-color circularly polarized laser fields. Chemical Physics Letters, 706:62 – 67, 2018.

[253] Kai-Jun Yuan and André D. Bandrauk. Attosecond-magnetic-field-pulse generation by electronic currents in bichromatic circularly polarized uv laser fields. Phys. Rev. A, 92:063401, 2015.

[254] Kai-Jun Yuan, Szczepan Chelkowski, and André D. Bandrauk. Photoelectron momentum distributions of molecules in bichromatic circularly polarized attosecond uv laser fields. Phys. Rev. A, 93:053425, 2016.

[255] Qingbin Zhang, Gihan Basnayake, Alexander Winney, Yun Fei Lin, Duke Debrah, Suk Kyoung Lee, and Wen Li. Orbital-resolved nonadiabatic tunneling ionization. Phys. Rev. A, 96:023422, 2017.

[256] Kun Zhao, Qi Zhang, Michael Chini, Yi Wu, Xiaowei Wang, and Zenghu Chang. Tailoring a 67 attosecond pulse through advantageous phase-mismatch. Opt. Lett., 37(18):3891–3893, 2012.

[257] Xi Zhao, Jing Chen, Panming Fu, Xueshen Liu, Zong-Chao Yan, and Bingbing Wang. Carrier-envelope-phase effect in a long laser pulse with tens of optical cycles. Phys. Rev. A, 87:043411, 2013.

[258] Nickolai Zhavoronkov and Mikhail Ivanov. Extended ellipticity control for attosecond pulses by high harmonic generation. Opt. Lett., 42(22):4720–4723, 2017.

[259] Jianping Zhou, Greg Taft, Chung-Po Huang, Margaret M. Murnane, Henry C. Kapteyn, and Ivan P. Christov. Pulse evolution in a broad-bandwidth ti:sapphire laser. Opt. Lett., 19(15):1149–1151, 1994.

[260] H. Zimmermann, J. Buller, S. Eilzer, and U. Eichmann. Strong-field excitation of helium: Bound state distribution and spin effects. Phys. Rev. Lett., 114:123003, 2015.

[261] H. Zimmermann, S. Patchkovskii, M. Ivanov, and U. Eichmann. Unified time and frequency picture of ultrafast atomic excitation in strong laser fields. Phys. Rev. Lett., 118:013003, 2017.